Radar Band Fusion for improved Range Resolution using Compressed Sensing

DISSERTATION zur Erlangung des Grades eines Doktors der Ingenieurwissenschaften

vorgelegt von
Sanhita Guha

eingereicht bei der Naturwissenschaftlich-Technischen Fakultät
der Universität Siegen
Siegen 2024

betreut von
Prof. Dr.-Ing. Joachim Ender
Dr.-Ing. habil. Miguel Heredia Conde

Tag der Mündlichen Prüfung: 08.04.2024

Zusammenfassung

Hochauflösende Radarbilder können in der Regel nur erstellt werden, wenn die Szene mit einem Breitbandradar erfasst wird. In den letzten Jahren wurden die Anwendungen der Fernerkundung stetig weiterentwickelt. Das führte dazu, dass der Bedarf an hochauflösenden Radarbildern wesentlich gestiegen ist. Damit wuchs auch der Wunsch nach mehr Frequenzbändern mit hoher Bandbreite. Auf der anderen Seite ist das Frequenzspektrum eine begrenzte Ressource, in der Bereiche für eine große Anzahl von Geräten und Anwendungen zur Verfügung gestellt werden müssen. Dies führte dazu, dass für bildgebendes Radar in vielen Fällen nur unzusammenhängende schmale Bänder genutzt werden können. Das dieser Arbeit zugrundeliegende Ziel besteht nun darin, die gewünschte hohe Auflösung durch gemeinsame Nutzung dieser verfügbaren Bänder zu erreichen.

Da es sich bei diesem Problem um einen Spezialfall der Bildgebung mit fehlenden oder begrenzten Messungen handelt, wurde die bisherige Forschung in diesem Bereich gesichtet. Es zeigte sich, dass verschiedene Methoden entwickelt worden sind, hochauflösende Bilder mit einer begrenzten Anzahl von Messungen zu prozessieren. Dabei kommt den auf Compressed Sensing (CS) basierenden Methoden eine besondere Bedeutung zu. CS-Verfahren machen sich die geringe Dichte einer Szene zunutze, um ein unterbestimmtes System linearer Gleichungen effizient zu lösen und damit eine hochauflösende Szenenschatzung zu liefern. Da Radarszenen wegen des Vorhandenseins dominanter Streuer häufig als dünn besetzt angenommen werden kann, ist der Einsatz von CS-Verfahren ein logischer Ansatz. Es hat sich jedoch gezeigt, dass in den meisten bestehenden Arbeiten die Situation zufällig fehlender Stichproben behandelt wird. Das in dieser Arbeit behandelte Problem ist es jedoch anders. Die unzusammenhängenden schmalen Bänder in der aktuellen Situation führen zu kontinuierlichen Blöcken fehlender Daten oder, mit anderen Worten, zu kontinuierlichen Lücken im Frequenzband.

Die Anwendung von CS auf ein solches "Gapped-Band" Problem ist nach Kenntnis der Autorin in der Literatur noch nicht untersucht worden. Die Arbeit zielt darauf ab, diese Forschungslücke zu schließen. Konkret werden zwei Themen behandelt:

- Kohärenz: Die Kohärenz ist eine Metrik zur Beurteilung der Qualität der Erfassungmatrix (sensing matrix). Ein niedriger Kohärenzwert entspricht einem besser konditionierten Ausgangspunkt für die Szenenschatzung. Für eine Steigerung der Entfernungsauflösung muss die Schätzung der Szene auf einem engmaschigen Entfernungsraster erfolgen, was zu einem Anstieg der Kohärenz führt. Das Vorhandensein einer kontinuierlichen Lücke verschärft dieses Problem noch.

- Hoher Rechenaufwand: Der hohe Rechenaufwand ist eine Herausforderung beim Einsatz von CS für praktische Radaranwendungen. Insbesondere bei Verfahren wie Synthetic Aperture Radar (SAR) ist die Menge der pro Szene erzeugten Rohdaten sehr groß. Die zusätzliche Anforderung einer höheren Auflösung macht die SAR-Bildrekonstruktion noch rechenintensiver.

In dieser Arbeit werden die oben genannten Probleme durch die folgenden Beiträge angegangen: Zunächst werden strukturierte Erfassungsmatrizen formuliert, die das "Gapped-Band" berücksichtigen. Dann werden zwei Algorithmen vorgeschlagen - der Subdivision Fusion (SF)-Algorithmus und der Approximated Observation

(AO)-Algorithmus. Der SF-Algorithmus löst beide Probleme durch ein Unterteilungsschema, das auf den vorgeschlagenen strukturierten Erfassungsmatrizen basiert. Der Unterteilungsschritt verbessert den Kohärenzwert, reduziert die Größe des CS-Problems und ermöglicht eine parallele Ausführung. Der AO-Algorithmus geht ebenfalls auf beide Probleme ein, indem er die die Multiplikation mit einer CS-Erfassungsmatrix bzw. deren hermitesch Konjugierten durch Prozessoren mit angepassten Filtern ersetzt. Die rechenintensiven Multiplikationen mit der Erfassungsmatrix werden durch FFTs innerhalb einer Schleife des CS-Algorithmus mit weicher Schwellenbildung (soft thresholding) ersetzt. Bei beiden Algorithmen werden neue Ideen und Modifikationen eingebracht, um bestehende CS-Methoden an das Gapped-Band-Problem anzupassen.

Darüberhinaus wird in dieser Arbeit eine Erweiterung des SF-Algorithmus vorgestellt, die sich mit der Mehrwegeabbildung für ein time-of-flight (ToF)-System befasst und damit zeigt, dass die vorgeschlagene Idee flexibel ist und für verschiedene Abbildungssysteme angepasst werden kann.

Die Algorithmen wurden sowohl an simulierten Szenen als auch an realen Daten getestet. Die erzielten Ergebnisse zeigen eine deutliche Verbesserung der Entfernungsauflösung trotz der Kohärenzbeschränkungen, die durch das lückenhafte Band entstehen. Die vorgeschlagenen Umstrukturierungen der CS-Erfassungsmatrix kann die Konditionierung des zuvor schlecht gestellten CS Problems verbessern und es ermöglichen, recht gute Szenenschatzungen zu liefern. Die Arbeit schließt mit einer Diskussion zukünftiger Richtungen für praktische Anwendung der vorgeschlagenen Ideen.

Abstract

High range resolution radar imaging is possible only when a scene is detected using a wide band radar. In the past few years, remote sensing applications have multiplied and evolved rapidly, which has led to an increased demand for such high resolution imaging. As a result, the need for wider frequency bands has also increased. However, there has been an exponential rise in spectrum congestion, leading to a direct conflict with this wide band requirement. A large number of devices and applications need access to the frequency spectrum, which is a limited resource. Consequently, in many cases, only disjoint narrow frequency bands are available for imaging. Therefore, the goal is to now obtain the desired high resolution by making use of the available narrow bands.

Since this problem appears to be a specialized case of imaging with missing or limited measurements, it makes sense to examine past research done in this area. It is found that several efforts have been made to obtain high resolution images using a limited number of measurements, out of which Compressed Sensing (CS) based methods are quite popular. CS techniques exploit the underlying sparsity of a scene to efficiently solve an under-determined system of linear equations and provide a high-resolution scene estimate. Since radar scenes are inherently sparse, this is a logical approach. However, it is found that in most existing works, the limitation in the number of measurement arises due to randomly missing samples. The problem addressed here is slightly different. The disjoint narrow bands in the current situation give rise to continuous blocks of missing data, or, in other words, continuous gaps in the frequency band.

CS applied to such a 'gapped-band' problem has, to the author's knowledge, not been explored in literature and this thesis aims to address this research gap. Specifically, two issues are addressed :

- Coherence: The coherence is a metric that determines the quality of the CS sensing matrix and a lower coherence value corresponds to a better scene estimate. For a higher range resolution, the scene estimation must be carried out on a finely spaced range grid, which leads to an increase in coherence. The presence of a continuous gap further aggravates this problem.

- Large computational load: High computational load is a popular challenge in using CS for practical radar applications. Specially for systems like Synthetic Aperture Radar (SAR), the volume of raw data generated per scene is large. The additional requirement of a higher resolution makes the SAR image reconstruction even more computationally expensive.

This thesis addresses the aforementioned problems via the following contributions. First, structured sensing matrices are formulated taking the 'gapped-band' into consideration. Then, two algorithms are proposed— the Subdivision Fusion (SF) algorithm, and the Approximated Observation (AO) algorithm. The SF algorithm addresses both the problems via a subdivision scheme based on the proposed structured sensing matrices. The subdivision step improves the coherence value, reduces the size of the CS problem and makes a parallel execution possible. The AO algorithm also addresses both issues by replacing the CS sensing matrix with matched filter based processors. Computationally heavy multiplications involving the sensing matrix are replaced by FFTs within a soft-thresholding CS algorithm loop. Both algorithms introduce new ideas and modifications to adapt existing CS methods to the gapped-band problem. In addition, the thesis presents an extension

of the SF algorithm that deals with multi-path imaging for a ToF system, thereby showing that the proposed idea is flexible and may be adapted for different imaging systems.

The algorithms are tested on synthetic scenes as well as real world data and the results achieved show significant improvement in range resolution despite the coherence limitations imposed by the gapped band. It is concluded that the proposed modifications to the CS sensing matrix improve the conditioning of the previously ill-posed CS problem and allow it to provide better scene estimates. Possible future directions involving practical applications of the proposed ideas are also discussed.

Acknowledgements

I would like to express my sincere gratitude to my supervisors Prof. Joachim Ender and Dr. -Ing. habil Miguel Heredia Conde for their continued support, motivation and valuable contributions during the PhD journey. Their vast knowledge and experience in the field of compressive sensing, along with their continued guidance made it possible for me to efficiently carry out the assigned tasks. Our numerous technical discussions have motivated me and given me new perspective on how to approach complex problems.

I would like to thank Prof. Otmar Loffeld, without whom this project would not have started. He was the initiator of this PhD program and his absence was profoundly felt while we continued on the path set out by him. I am grateful that I got the opportunity to meet him in person and will always remember him as a confident and charismatic mentor.

I would like to thank Dr. Andreas Bathelt for his guidance and important scientific contributions to the work. The timely execution of all the sub-tasks in this project would not have been possible without his supervision, specially during the challenging phases towards the beginning of the program. His advice on technical writing and mathematical formulations have helped me a lot in improving my skills as a researcher. I would also like to thank him for his administrative support throughout the project.

I would like to thank Prof. Mihai Datcu and Prof. Andrei Anghel, for supervising me during my secondment at Politechnica University of Bucharest (UPB). I am grateful that I got the opportunity to have interesting technical discussions with them. I thank them for being present at conferences and introducing me to other researchers working in similar fields. I would also like to express my sincere gratitude to Prof. Paula Lopez Martinez and Prof. Daniela Coltuc. Although I was not directly supervised by them, their questions, inputs and suggestions during our research presentations have added a lot of value to the work.

I would like to thank my fellow ESRs who have always been supportive and encouraging throughout this journey. My colleagues at UPB and Center for Sensor Systems (ZESS), University of Siegen, made me feel very welcome during my secondments. Their encouragement and motivation have largely contributed to the success of these sub-projects.

I would like to express my gratitude to my fellow ESR, Faisal Ahmed, for acquiring the multi-path Time-of-flight (ToF) measurements during my secondment at ZESS and making it possible to successfully carry out the study within a limited time frame.

I would like to thank Dr. Andre Froehly from the Dept. of Integrated Circuits and Sensor Systems, Fraunhofer Institute for High Frequency Physics and Radar Techniques (FHR), who made it possible to acquire real FMCW radar measurements that supported the work done in the journal paper.

I want to thank my colleagues and superiors at Fraunhofer FHR, specially Dr. Michael Caris, Gregor Biegel, Dr. Stephan Stanko, Stephan Sieger, Michael Weimer, Anna Bischof, and Frank Klöppel, who were always ready to help with the technical, logistical and administrative challenges. I want to thank Sandra Herde and Annett Pilz for handling the formalities associated with the business trips for conferences and secondments. Lastly, I want to thank Siying Wang for being very kind and for encouraging me during tough times.

Finally, I thank my family and friends for their encouragement and support throughout this journey.

Contents

Chapter 1

Introduction

1.1 Background and Motivation

The term 'remote sensing' refers to the collection of data or information from an object of interest at a distance. It encapsulates imaging modalities working in different parts of the wavelength spectrum that are used to collect data unobtrusively, from a distant object or a scene of interest. Over the years, there has been an increasing demand for high-resolution remote sensing systems across different parts of the wavelength spectrum. Radars are one such imaging modality that work in the GHz frequency range and are used in numerous applications such as tracking and surveillance, environmental monitoring, and disaster management [GBC+13], [GCW+15]. Time-of-Flight (ToF) cameras are another example of a macroscopic imaging modality that work in the MHz frequency range and have applications in the automotive industry, safe patient monitoring for healthcare, 3D scanning, and human-machine interactions [NKR+15], [KBC13], [IHJ16].

What does such a high resolution requirement imply in the framework of a general signal model? Consider, a signal model represented by the equation [1]

$$\mathbf{y} = \boldsymbol{A}\mathbf{x},$$

where $\mathbf{y}$ represents the measurement vector, $\boldsymbol{A}$ represents the sensing matrix and $\mathbf{x}$ denotes the scene being detected. Consider this signal model to be defined in the complex domain $\mathbb{C}$. The vector $\mathbf{y}$ contains a fixed number of samples as dictated by the sensing system. If $\boldsymbol{A}$ was a full-rank square matrix, or in other words, a one-to-one mapping between the measurements and the scene, $\mathbf{x}$ would have the same length as $\mathbf{y}$. In such a scenario, the resolution of the scene $\mathbf{x}$ is the baseline resolution provided by the imaging system, without any modifications. Now, the goal is to improve the resolution of $\mathbf{x}$. Such an improved resolution is possible only if $\mathbf{x}$ lies on a finer grid. For this to happen, $\boldsymbol{A}$ has to be a horizontal matrix, giving rise to an under-determined system of linear equations. Finer the grid, more under-determined is the system.

Therefore, obtaining a higher resolution is synonymous to finding a good solution for an under-determined system of linear equations. Once this is established, one can make use of the vast literature available on solving under-determined systems. Since this is such a fundamental problem appearing in numerous research areas, different approaches to tackle this issue have been proposed by different communities, and a detailed discussion is presented in Chapter 4. It is observed that in many of these approaches, exploiting the sparsity of the scene in a certain domain is a recurring theme, and this naturally warrants focusing on the well-established sparsity-driven signal processing technique known as Compressed Sensing (CS).

[1] The measurement noise in the signal model is ignored here for simplicity.

The theory of CS has been extensively studied in the past and it comes with a very strong mathematical framework. Several classes of CS algorithms exist in literature and are known to perform quite well in solving the under-determined system to give a good estimate of $\mathbf{x}$.

But now, the problem becomes more difficult. Consider again the signal model equation, with a focus on the range resolution of radar systems. Let $\mathbf{y}$ represent the measurement vector with samples in the frequency domain. The baseline range resolution provided by a system depends on the bandwidth B of the transmitted signal, and is given by $\delta r = \frac{c}{2B}$. Thus larger the bandwidth, higher is the range resolution. For a constant sampling rate, a larger bandwidth implies more number of samples for the vector $\mathbf{y}$, thereby allowing a finer baseline range grid for $\mathbf{x}$. Now, a range grid having range cells of width $\Delta r < \delta r$ can be defined in an attempt to improve the range resolution further, leading to an under-determined system. However, a finer range resolution may not be the only reason behind this under-determined structure — an under-determined system can also exist if the some samples in $\mathbf{y}$ are missing, even for the baseline range resolution. What if there exists a condition that forces $\mathbf{y}$ to have a low number of samples?

In the recent years, there has been an exponential increase in the number of applications that use the frequency spectrum, leading to spectrum congestion [LMP+20], [DCW+13], and as a result, leading to the unavailability of wide frequency bands needed for a high range resolution. In other words, spectrum congestion is a condition that forces 'compression at sensing'. Therefore, the sensing must take place using the limited narrow frequency bands, while at the same time catering to the resolution requirements posed by various applications. Such narrow, disjointed frequency bands may be viewed as a wide band with several blocks of missing data. The previously simple under-determined system now becomes an under-determined system with gaps or a 'gapped-band' system. The advantage of such a gapped-band point of view is as follows :

- The under-determined system has become even more under-determined, but the basic structure remains the same. So, CS methods are still a valid approach.
- Challenges faced by practical sensing schemes (eg: Joint Communication and Sensing (JCS)) due to spectrum congestion can be recast into the gapped band problem.

Expanding on the former point, CS based missing data estimation techniques are explored to solve the gapped band problem. It is found that most of the existing works assume randomly missing data samples. A continuous block of missing data in an under-determined system is not addressed, bringing forth an important research gap. In addition, most traditional CS algorithms work under the assumption that the 'Coherence' of the CS sensing matrix lies within a certain bound, detailed in Chapter 3. The continuous gap challenges this assumption, but the performance of traditional CS algorithms in the presence of such a gap has not been studied.

Existing compressed sensing algorithms pose high computational complexity and large memory requirements, and have not been adapted to deal with the gapped-band problem. At the same time, there continues to be an increase in spectrum congestion, while the need for high resolution images remains constant. This bottleneck is the motivation behind the work done in this thesis. In order provide high resolution images inspite of the growing spectrum unavailability, it is necessary to develop adaptive CS algorithms that can deal with such challenges.

1.2 Research Objectives

The objectives of this work are outlined as follows:

- Theory development and simulations on the application of adaptive compressed sensing methods to reconstruct high resolution range profiles from two disjoint band radar signals.
- Testing of the developed methods for various radar domains, including SAR and ISAR imaging.

1.3 Contributions

The main contributions of this thesis are as follows :

- A gapped CS model is derived for chirped radar systems. A more practical extension to multiple co-located narrow band FMCW radar systems is also derived, showing the relation between 'gapped-band' systems and 'disjoint narrow-band' systems.
- A Subdivision-Fusion algorithm is proposed which uses the subdivision of a structured sensing matrix to obtain multiple smaller CS sensing matrices with lower coherence values. This allows solving for a number of smaller CS problems in parallel, thereby reducing the computational time and memory load. A fusion of the results gives the final estimate of the scene. The algorithm is tested on real radar data. This concept is also extended to the multi-path resolution problem for ToF cameras, demonstrating the flexibility of the overall idea.
- An Approximated Observation algorithm is discussed, which aims to reduce the complexity of CS applied to SAR systems. Specifically, it proposes to replace the CS sensing matrix by popular matched filter based SAR processors, thereby removing the large matrix multiplications involved in a normal SAR-CS implementation. Results obtained by application of the algorithm on real SAR data are provided.

1.4 Outline

The remainder of the thesis is organized as follows:

- Chapter 2 gives an overview of the Radar fundamentals and the working principle of a general radar system. The most commonly used radar waveforms are discussed. The main ideas SAR and ISAR imaging are also presented.
- Chapter 3 reviews the fundamentals of CS. It gives the details of the key components that constitute a CS problem. It presents the metrics that determine the quality of a CS sensing matrix followed by an overview of the most popular CS algorithms.
- Chapter 4 discusses CS applied to radar systems. It combines the ideas discussed in Chapters 2 and 3. The CS framework is explored based on the radar waveforms introduced previously.

- Chapter 5 discusses the work done to tackle the problem of missing data estimation under 3 broad subtopics and underlines the challenges faced by the existing approaches.
- Chapter 6 presents the problem statement of the thesis and mathematically defines the gapped band problem based on the CS models described in Chapter 4.
- Chapter 7 presents 2 algorithms to tackle the gapped-band problem for radar systems. Simulation results and results on real radar data are discussed.
- Chapter 8 uses a modified version of the Subdivision-Fusion algorithm to solve the multi-path interference problem faced by ToF cameras. The algorithm is applied to multi-path ToF data and the resulting depth images are provided.

Chapter 2

Radar Working Principles

2.1 Working Principle of General Radar Systems

The principle function of a radar is to detect a target and determine its location by emitting a signal and receiving its echo, after it is back-scattered by the target. The differences between the emitted and the received signal provide information about the target location, structure, material, etc.

Based on Maxwell's equations [W14], the emitted and received signals have to be real-valued radio-frequency (RF) signals. The common form of such an RF signal typically used for radars is given by

$$\begin{aligned} s_{\mathrm{RF}}(t) &= \mathcal{R}\{s(t) \exp j2\pi f_0 t\} \\ &= \mathcal{R}\{s(t)\} \cos 2\pi f_0 t + \mathcal{I}\{s(t)\} \sin 2\pi f_0 t \ , \end{aligned} \tag{2.1}$$

where $s(t)$ is the complex envelope, i.e., the complex waveform of the transmitted signal in baseband. $\mathcal{R}\{.\}$ and $\mathcal{I}\{.\}$ represent the real and imaginary component of the signal respectively. f_0 is the carrier frequency of the radar signal, also called the 'reference frequency' or the 'local frequency (LO)' and is usually in the range of GHz. $\cos 2\pi f_0 t$ and $\sin 2\pi f_0 t$ are known as the LO signals.

Direct signal processing in the RF domain is infeasible and impractical since it presents a large computational load and does not yield any additional information. Since all the information lies in the modulation, it makes sense to carry out the signal processing in the baseband. The complex valued baseband signal $s(t)$ can be generated by an arbitrary waveform generator (AWG) or direct digital synthesizer (DDS). Then, the so called 'quadrature modulator' (QM) in the emitter transforms $s(t)$ to $s_{\mathrm{RF}}(t)$. The emitted RF signal is back-scattered from the target, and fed via the receiver antenna into the radar receiver. Finally, the 'quadrature demodulator' (QDM) in the receiver re-extracts the complex waveform. Figs. 2.1 and 2.2 show the basic structure of a QM and QDM respectively.

Consider the relation between $s_{\mathrm{RF}}(t)$ and $s(t)$ in the frequency domain. Based on (2.1), the Fourier-transform of the RF signal will be

$$s_{\mathrm{RF}}(f) = \frac{1}{2}\left(s(f+f_0) + s(f-f_0)\right) \ . \tag{2.2}$$

Let, $s(t)$ be bandlimited to the frequency interval $[\frac{-b}{2}, \frac{b}{2}]$. Substituting these bandlimits in (2.2), $s_{\mathrm{RF}}(f)$ exists in 2 disjoint frequency intervals, $[f_0 - \frac{b}{2}, f_0 + \frac{b}{2}]$ and $[-f_0 - \frac{b}{2}, -f_0 + \frac{b}{2}]$.

Mathematically, $s(t)$ can be recovered from $s_{\mathrm{RF}}(f)$ by first removing the negative frequencies and creating a single-sided spectrum containing only the positive part of the frequency band. Then, this positive spectrum is shifted to the left by f_0, thereby

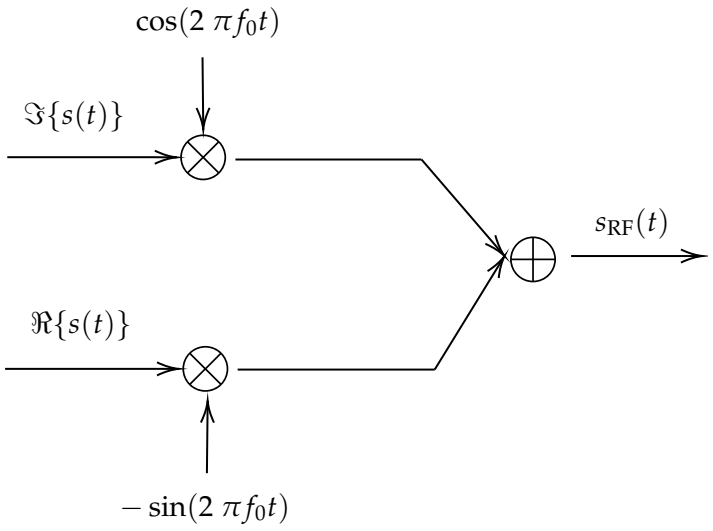

FIGURE 2.1: Quadrature Modulator (QM).

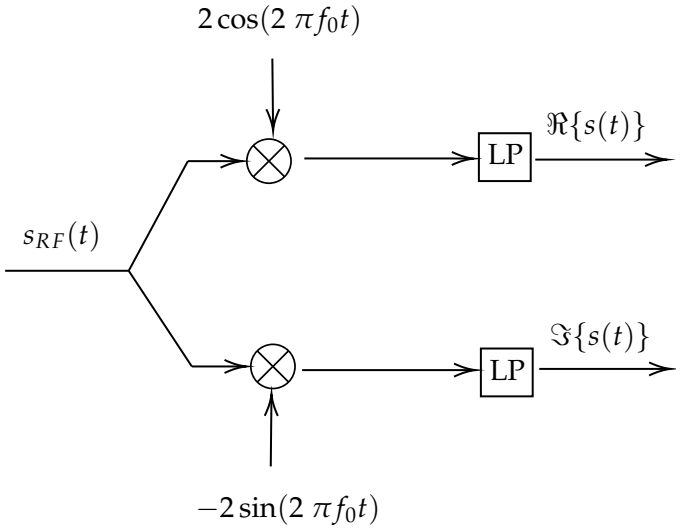

FIGURE 2.2: Quadrature Demodulator (QDM).

centering it around $f = 0$. Multiplying it by a factor 2 and applying the inverse Fourier Transform gives back $s(t)$.

In practice, the recovery of $s(t)$ is done by the QDM. The $s_{\mathrm{RF}}(t)$ signal is passed to 2 mixers and down-mixed with the LO signals, $2\cos 2\pi f_0 t$ and $-2\sin 2\pi f_0 t$, which are produced by a stable frequency source. To understand how the QDM outputs are used to recover the transmitted signal, the following trigonometric equations are required:

- $\cos^2(2\pi f_0 t) = \frac{1}{2}(1 + \cos(4\pi f_0 t))$.
- $\sin^2(2\pi f_0 t) = \frac{1}{2}(1 - \cos(4\pi f_0 t))$.
- $\sin(2\pi f_0 t)\cos(2\pi f_0 t) = \frac{1}{2}\sin(4\pi f_0 t)$.

Now, the 2 outputs from the QDM give the real and imaginary components of $s(t)$ along with some additional terms, i.e.,

$$\begin{aligned} s(t)\,2\cos(2\pi f_0 t) &= 2\mathcal{R}\{s(t)\}\cos^2(2\pi f_0 t) - 2\mathcal{I}\{s(t)\}\sin(2\pi f_0 t)\cos(2\pi f_0 t) \\ &= \mathcal{R}\{s(t)\}(1 + \cos(4\pi f_0 t)) - \mathcal{I}\{s(t)\}\sin(4\pi f_0 t) \\ &= \mathcal{R}\{s(t)\} + \mathcal{R}\{s(t)\}\cos(4\pi f_0 t) - \mathcal{I}\{s(t)\}\sin(4\pi f_0 t) \end{aligned} \tag{2.3}$$

$$\begin{aligned} s(t)\,(-2\sin(2\pi f_0 t)) &= -2\mathcal{R}\{s(t)\}\cos(2\pi f_0 t)\sin(2\pi f_0 t) + 2\mathcal{I}\{s(t)\}\sin^2(2\pi f_0 t) \\ &= -\mathcal{R}\{s(t)\}\sin(4\pi f_0 t) + \mathcal{I}\{s(t)\}(1 - \cos(4\pi f_0 t)) \\ &= \mathcal{I}\{s(t)\} - \mathcal{I}\{s(t)\}\cos(4\pi f_0 t) - \mathcal{R}\{s(t)\}\sin(4\pi f_0 t)\ . \end{aligned} \tag{2.4}$$

The unwanted terms at $\pm 2f_0$ are removed using low-pass filters. If the output of the QM is directly passed to the input of the QDM , the output from the QDM is identical to the input signal of QM. This structure may now be expanded to describe a complete radar system.

Fig. 2.3 shows the structure of a radar system. The output from the QM is amplified and passed through a transmit/receive switch to the antenna and emitted into free space. It is reflected by a target at a distance r and received by the antenna with a time delay τ. Considering the round trip of the signal, the delay is given by $\tau = \frac{R}{c}$, where $R = 2r$, and c is the speed of light in free space. This signal is amplified and sent into the QDM to obtain the baseband received signal, i.e., the time-delayed version of the emitted signal containing the range information.

2.2 Radar Waveforms

In the previous section, the basic working principal of a radar system was described using an arbitrary signal $s(t)$. This section focuses on 2 types of radar waveforms: 1) the pulse waveform and 2) the Linear Frequency Modulated (LFM) waveform, also commonly known as the chirp.

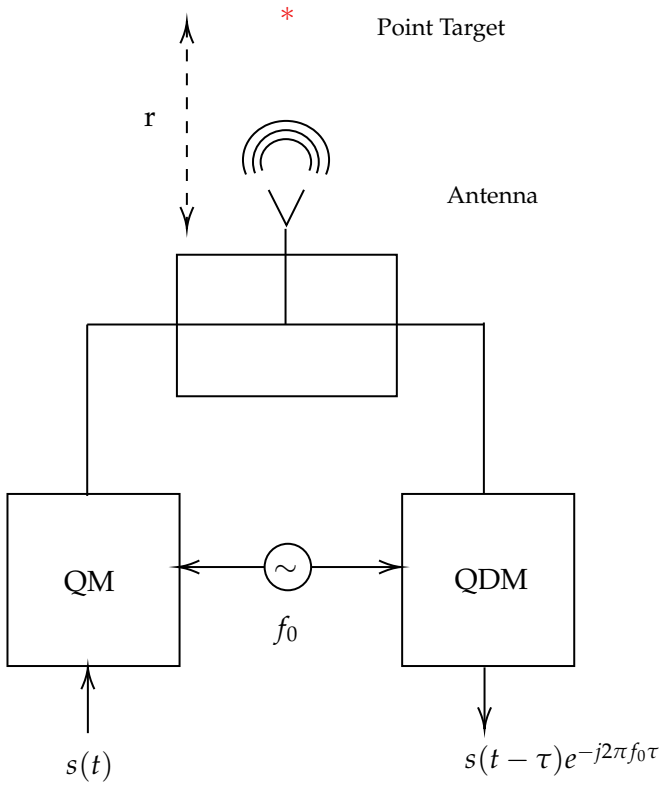

FIGURE 2.3: Structure of a radar system combining QM and QDM.

2.2.1 The Pulse Waveform

Waveform Characteristics

The most basic radar waveform is the rectangular pulsed waveform, or the 'pulse burst' waveform which consists of a series of rectangular pulses. A single rectangular pulse defined by an amplitude A and a time period T_p, and is given by

$$s(t) = A \text{ rect}\left(\frac{t}{T_p}\right) . \tag{2.5}$$

A more generalized extension of the rectangular pulse is the coded rectangular pulse, given by

$$s(t) = A \text{ rect}\left(\frac{t}{T_p}\right) e^{\phi} , \tag{2.6}$$

where ϕ is an arbitrary phase term that depends upon the 'code' under consideration. In coded pulses, the frequency and/or phase changes across the pulse according to the selected frequency coding or phase coding algorithm. When $\phi = 0$, $s(t)$ reverts to the basic rectangular pulse. (2.6) allows a natural extension to the LFM waveform described in detail in the following section.

Each pulse in the 'pulse train' or 'pulse burst' waveform is separated by a fixed time duration known as the 'Pulse Repetition Interval (PRI)'. The reciprocal of PRI is the 'Pulse Repetition Frequency (PRF)'. Following the basic radar working principles, the time delay between the emitted and the received signal is used to determine the position of the target. In other words, the distance to the target is determined by

$$r = \frac{R}{2} = \frac{c\tau}{2}, \tag{2.7}$$

where R is the total distance travelled by the signal, c is the speed of light, and τ is the time delay. The accuracy of the detected target distance r depends on the range resolution, δr, of the radar system, which is defined as the smallest distance between two targets that produces separable echos in the received signal.

In order to define δr, the spectrum of the rectangular pulse has to be examined. It is a sinc-function with the main lobe lying between the frequencies $\frac{-1}{T_p}$ and $\frac{1}{T_p}$. Since this spectrum is not band-limited, there are different ways to describe the bandwidth [R14, p.183]. In this work, bandwidth refers to the commonly used Rayleigh bandwidth where $B = \frac{1}{T_p}$. Theoretically, B is used to estimate the sampling frequency F_s, i.e, $F_s = B$. As a result, the sampling time is $T_s = \frac{1}{F_s} = \frac{1}{B}$. Following this, the range resolution is given by

$$\delta r = \frac{cT_s}{2} = \frac{c}{2B}. \tag{2.8}$$

The Matched Filter

In order to describe range detection by any radar system, it is important to take noise into consideration. A radar system has to provide robust detection when challenged by noise and clutter. Therefore, in order to accurately determine a target position, it is important to have a high 'Signal-to-Noise' ratio (SNR). In this section, the most popular filtering method used for optimizing the SNR , namely the 'matched filter', is discussed.

Before deriving the matched filter, it is important to note that commonly, radar signal processing takes place in the digital domain. The received signal $s(t-\tau)$ is sampled using an analog-to-digital converter (ADC) and then passed to the matched filter. Although there exists analog versions of the matched filter, the digital or time-discrete matched filter is the one used more commonly and is introduced in this section. The time-continuous version of the matched filter has theoretical importance and is introduced later in relation to the chirp waveform.

To derive the matched filter, consider $\mathbf{z}$ to be the N-dimensional received signal obtained after digitization by the ADC, $\mathbf{s}$ to be the N-dimensional digital representation of the transmitted signal $s(t)$, a to be the amplitude and $\mathbf{n}$ to be a vector representing white Gaussian noise having a mean value of zero and a variance of σ^2. Therefore,

$$\mathbf{z} = a\mathbf{s} + \mathbf{n} \tag{2.9}$$

represents the noisy signal available to the receiver. Now, the goal is to determine a weighting vector $\mathbf{w}$ that maximizes the SNR, which is given by

$$SNR(\mathbf{w}) = \frac{|a\mathbf{w}^H\mathbf{s}|^2}{\mathbb{E}\{|\mathbf{w}^H\mathbf{n}|\}^2} = \frac{|a|^2|\mathbf{w}^H\mathbf{s}|^2}{\mathbb{E}\{\mathbf{w}^H\mathbf{n}\mathbf{n}^H\mathbf{w}\}} = \frac{|a|^2|\mathbf{w}^H\mathbf{s}|^2}{\mathbf{w}^H\mathbb{E}\{\mathbf{n}\mathbf{n}^H\}\mathbf{w}}. \tag{2.10}$$

The expectation in the denominator of (2.10) is the covariance matrix of the additive noise $\mathbf{n}$, which is given by $R_n = \sigma^2\mathbf{I}_n$. Thus, by substitution in the denominator, the expression becomes

$$SNR(\mathbf{w}) = \frac{|a|^2|\mathbf{w}^H\mathbf{s}|^2}{\mathbf{w}^H\sigma^2\mathbf{I}_n\mathbf{w}} = \frac{|a|^2|\mathbf{w}^H\mathbf{s}|^2}{\sigma^2\|\mathbf{w}\|^2}. \tag{2.11}$$

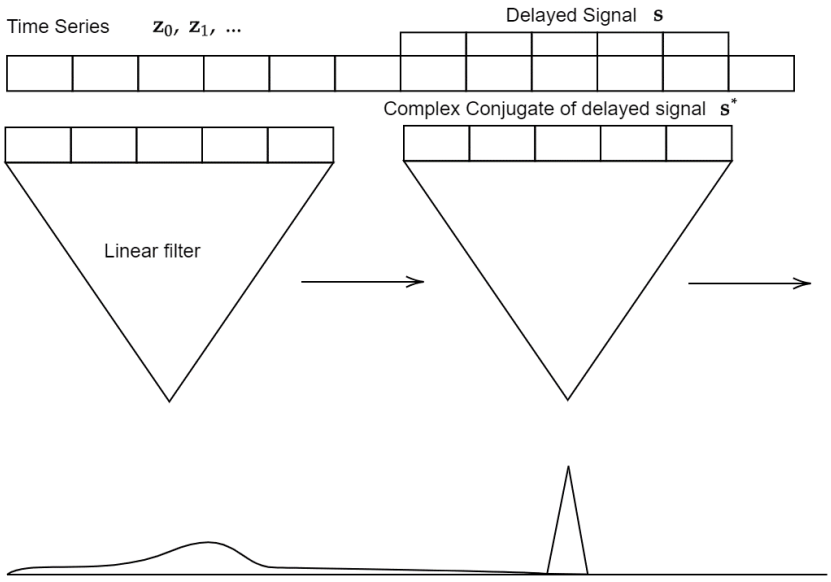

FIGURE 2.4: Matched Filter [E20].

Multiplying $\|\mathbf{s}^2\|$ in the numerator and denominator gives

$$SNR\left(\mathbf{w}\right) = \frac{|a|^2|\mathbf{w}^H\mathbf{s}|^2}{\sigma^2\|\mathbf{w}\|^2}\frac{\|\mathbf{s}\|^2}{\|\mathbf{s}\|^2} = \frac{|a|^2\|\mathbf{s}\|^2}{\sigma^2}|\rho\left(\mathbf{w},\mathbf{s}\right)|^2\,, \tag{2.12}$$

where $\rho\left(\mathbf{w},\mathbf{s}\right)$ is the correlation coefficient of the weight vector and the transmitted signal and can be expressed as

$$\rho\left(\mathbf{w},\mathbf{s}\right) = \frac{\mathbf{w}^H\mathbf{s}}{\|\mathbf{w}\|\|\mathbf{s}\|}\,. \tag{2.13}$$

The absolute value of $\rho\left(\mathbf{w},\mathbf{s}\right)$ ranges from 0 to 1. It is clear from (2.12) that the maximum SNR is achieved when the correlation coefficient is 1, i.e., when $\mathbf{w}$ and $\mathbf{s}$ are collinear. This is achieved when the weight vector is a scaled version of the transmitted signal given by

$$\mathbf{w}_{opt} = w\mathbf{s}, w \neq 0\,. \tag{2.14}$$

$\mathbf{w}_{opt}$ provides the coefficients of the matched filter. The principle of working of a matched filter is shown in Fig. 2.4. The convolution of the matched filter and the signal gives a single peak with maximum SNR only when there is a complete overlap, i.e., the filter response exactly 'matches' the received signal. Considering that the received signal was back-scattered by a target at range r, the peak of the matched filter occurs at the corresponding time delay $\tau = \frac{2r}{c}$. So, once τ is obtained, the range of the target can be easily determined.

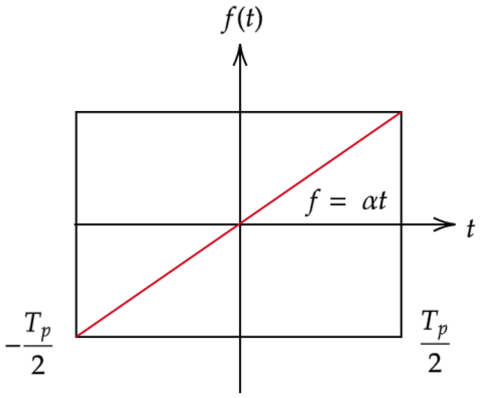

FIGURE 2.5: Chirp Frequency v/s Time.

2.2.2 The Chirp Waveform

For a simple rectangular pulse, the range resolution is directly proportional to the time duration of the pulse, since $B = \frac{1}{T_p}$. A short pulse results in a small δr value, i.e., a high range resolution, and can be used in near range systems such as ground penetrating radars.

However, the pulsed radar is unsuitable for long range target detection. The energy of a pulse is given by $A^2 T_p$. A long range detection requires increased pulse energy or a higher power, thereby an increased value of T_p, which is in direct conflict with the condition for better range resolution. To overcome this problem, pulse compression waveforms are commonly used. These waveforms decouple the energy and bandwidth by frequency modulation, and make it possible to meet both the energy and bandwidth requirements simultaneously. A large number of pulse compression waveforms exist in literature, out of which the chirp and the stepped frequency waveform are the ones most commonly used in high range resolution radars. The chirp waveform is re-used in the later chapters of this thesis. Therefore, in this chapter, the focus will be only on the chirp, which is formally known as the linear frequency modulated (LFM) waveform.

Waveform Characteristics

The chirp waveform is defined as

$$s(t) = A \,\text{rect}\left(\frac{t}{T_p}\right) e^{j2\pi\frac{\alpha}{2}t^2} , \tag{2.15}$$

where $\alpha = \frac{B}{T_p}$ is known as the chirp rate or the frequency modulation rate. Comparing with (2.6), it is evident that $\phi(t) = 2\pi\frac{\alpha}{2}t^2$, and therefore (2.15) is also referred to as the chirp-coded pulse. The instantaneous frequency of the chirp is the time derivative of the phase in (2.15) divided by 2π, and is given by

$$f(t) = \frac{1}{2\pi}\frac{\partial\left(2\pi\frac{\alpha}{2}t^2\right)}{\partial t} = \alpha t . \tag{2.16}$$

Due to the rect(.) window applied to the chirp, $f(t)$ spans the time interval $[-\frac{T_p}{2}, \frac{T_p}{2}]$, as shown in Fig. 2.5.

The Fourier transform of an LFM signal given by [KPD+60; LM04] is

$$s(f) = \frac{1}{\sqrt{T_p}} \int_{\frac{-T_p}{2}}^{\frac{T_p}{2}} e^{j\pi(\alpha t^2 - 2ft)} dt \ . \tag{2.17}$$

Fresnel Integrals [KPD+60; LM04] are used to compute this term as follows:

$$s(f) = \sqrt{\frac{1}{2BT_p}} e^{-j\pi\frac{f^2}{\alpha}} \left[Z\left(u_2\right) - Z\left(u_1\right) \right] , \tag{2.18}$$

where Z denotes the complex Fresnel integral, B the frequency bandwidth, and

$$\begin{aligned} Z(u) &= \int_0^u e^{j\pi\frac{\alpha^2}{2}} \\ u_1 &= -2f\sqrt{\frac{T_p}{2B}} - \sqrt{\frac{T_pB}{2}} \\ u_2 &= -2f\sqrt{\frac{T_p}{2B}} + \sqrt{\frac{T_pB}{2}} \ . \end{aligned}$$

The phase term can also be approximated by the principle of stationary phase (PSP) [R14], which defines a stationary point in time at which the first time derivative of the intergral phase is zero. The approximation of the integral in (2.17) is then given by

$$s(f) = j\sqrt{\frac{\pi}{\alpha T_p}} e^{\frac{-j\pi}{4}} e^{-j\frac{(\pi f)^2}{\alpha}} \text{rect}\left(\frac{f}{B}\right) \ . \tag{2.19}$$

Evaluation of the Fourier Tranform using Fresnel integrals shows ripples in the passband spectrum. This stems from the rectangular windowing of the signal in the time domain, which represents convolution with a sinc function in the frequency domain. The PSP approximation, on the other hand, works only at the points having stationary phase. Since the phase fluctuations are maximum near the edges, the PSP does not get a stationary point there. So, this approximation does not contain the ripple artifacts. With increase in the time-bandwidth product, the ripple artifact reduces, and the error between the Fresnel and the PSP-based frequency spectrum also reduces. Thus, a PSP-based Fourier Transform offers a good approximation to the one based on Fresnel.

The Matched Filter

How does such a frequency modulation based waveform help with the energy-bandwidth decoupling? Recall from Section 2.2.1 that the matched filter is the optimal filter that provides a high SNR for any general waveform. In this section, the matched filter response in continuous time domain is discussed for the chirp waveform.

Similar to 2.9, the continuous time domain received signal is given by

$$z\left(t\right) = as\left(t - \tau\right) + n\left(t\right) \ . \tag{2.20}$$

The output from the matched filter is

$$y\left(t\right) = \left(h * z\right)\left(t\right) \ , \tag{2.21}$$

where $h(t)$ denotes the response function of the filter. It can be derived that a maximum SNR is obtained for an optimal filter $h_{\text{opt}} = ws^*(-t)$. Using the optimal response function in (2.21), the output from the matched filter is

$$\begin{aligned} y(t) &= \left(h_{\text{opt}} * z\right)(t) \\ &= \int h_{\text{opt}}(\tau)\, z(t-\tau)\, d\tau \\ &= \int \mathrm{s}^*(-\tau)\, \mathrm{z}(t-\tau)\, d\tau \\ &= \int \mathrm{s}^*(\tau)\, \mathrm{z}(t+\tau)\, d\tau\,. \end{aligned} \tag{2.22}$$

Therefore, the matched filter output is basically the correlation of the noisy received signal with the time-inverted complex conjugate of the transmitted signal. If the noise is ignored, this is the auto-correlation of the signal, giving the point spread function of the waveform at the point of maximum overlap. Now, specifically using the chirp equation from (2.15) in (2.22) gives

$$p(t) = \int_{-\infty}^{\infty} \text{rect}\left(\frac{\tau - t}{T_p}\right) \text{rect}\left(\frac{\tau}{T_p}\right) e^{j2\pi\frac{\alpha}{2}\left(\tau^2 - (\tau - t)^2\right)}\, d\tau\,. \tag{2.23}$$

Since the autocorrelation is symmetric, (2.23) can be solved for $t \geq 0$ and be mirrored to the negative time. In this case, the rect $(.)$ simply defines the boundaries of the integral and the equation becomes

$$p(t) = e^{j2\pi\frac{\alpha}{2}t^2} \int_{t-\frac{T_p}{2}}^{\frac{T_p}{2}} e^{j2\pi\alpha\tau t}\, d\tau\,. \tag{2.24}$$

Solving this integral gives [KPD+60]

$$p(t) = \frac{\sin\left(\pi\alpha\left(T_p t - t^2\right)\right)}{\pi\alpha t}\,. \tag{2.25}$$

Substituting $\alpha = \frac{B}{T_p}$ in (2.25) and extending for negative time gives

$$p(t) = T_p \frac{\sin\left(\pi\left(B|t| - \alpha t^2\right)\right)}{\pi B|t|}\,. \tag{2.26}$$

Usually the term $\pi\alpha t^2$ can be ignored and the PSF can be approximated as

$$\mathbf{p}(t) = T_p \frac{\sin\left(\pi\left(B|t| - \alpha t^2\right)\right)}{\pi B|t|} \approx T_p \frac{\sin\left(\pi\left(B|t|\right)\right)}{\pi B|t|} = T_p\, \text{sinc}\left(Bt\right)\,. \tag{2.27}$$

In order to understand the decoupling of energy and resolution in the chirp waveform, it is compared to a simple pulse of the same duration T_p. Considering a large value of T_p is used , the waveform energy is sufficient and identical for both the pulse and the chirp. As before, the bandwidth of the simple pulse is $\frac{1}{T_p}$. However, the (swept) bandwidth for the chirp is αT_p, and can be much larger. From (2.27), the width of the main lobe of the PSF corresponding to the chirp depends on this swept bandwidth and is given by $\frac{1}{B} = \frac{1}{\alpha T_p}$, which is clearly much narrower than the width of the PSF of the simple pulse. Consequently, the value of the Rayleigh resolution of

the chirp waveform, given by $\frac{c}{2B}$, is much smaller, i.e., the resolution is much higher than that of the simple pulse. Thus, most of the energy is concentrated in the main lobe of the chirp PSF. The matched filter compresses the input to a pulse having the time duration corresponding to the actual bandwidth, and therefore, the matched filter output is sometimes called the compressed range profile.

Although such a filter provides an optimal SNR, the disadvantage is that the signal has to be sampled according to the Nyquist rate, implying that a large number of samples have to be stored, specially for wide band radars.

Deramping

Deramping, also known as stretch processing, is an alternative method to achieve the high resolution of a chirp waveform with reduced sampling requirements. The key idea is that the received chirp is demodulated with a complex conjugate time-delayed replica of the transmitted chirp, which results in a constant frequency signal. Considering the chirp waveform defined in (2.15) with a carrier frequency f_0, this replica, also known as the 'ramp', is given by

$$r\left(t\right) = e^{2\pi j\left(f_0(t-t_0)+\frac{\alpha}{2}(t-t_0)^2\right)} \ . \tag{2.28}$$

where t_0 is the time delay. The received signal has a time delay τ corresponding to the range of the target as before. Down-mixing of the received signal with the complex conjugate of the ramp results in

$$\mathrm{r}^*\left(t\right)\mathrm{s}\left(t-\tau\right) = \mathrm{rect}\left(\frac{t-\tau}{T_p}\right) e^{2\pi j\left(f_0(t_0-\tau)+\frac{\alpha}{2}\left(\tau^2-t_0^2\right)\right)} e^{2\pi j\alpha(t_0-\tau)t} \ . \tag{2.29}$$

The product of (2.29) can be split into three parts, the first term is the rect function, which represents a windowing in the time domain. The second term is an exponential term that represents a phase factor. The important component is the third term which has a constant frequency $\alpha(t_0-\tau)$, corresponding to the range of the target. The advantage of such a direct relation between the frequency and range is that a bandpass filter can be applied such that the frequencies in the pass band correspond to an adequate range window for the measurement. Thus, the bandwidth of the output corresponds to the passband and is much smaller than the bandwidth of the whole chirp. This reduces the sampling requirements, while preserving the original range resolution. The only drawback is that the ranges outside the range window are lost.

A brief note on k-space representation

For the upcoming sections on SAR and ISAR imaging, it is useful to consider the more commonly used wavenumber domain representation of the chirp, also called the 'k-space' notation. The wavenumber, k, is defined by $\frac{2\pi f}{c}$, and comes from the theory of propagation of electromagnetic waves. For a chirp, the wavenumber k_r of the propagating wave can be divided into 2 parts: 1) k_0, the contribution of the carrier frequency f_0, 2) k_b, the contribution of the baseband, αt. Thus,

$$k_r = k_0 + k_b = \frac{2\pi}{c}\left(f_0 + \alpha t\right) \ . \tag{2.30}$$

(2.30) corresponds to multiplication of the instantaneous chirp frequency with a constant factor of $\frac{2\pi}{c}$. Based on this notation, the output of de-ramping in (2.29) can be

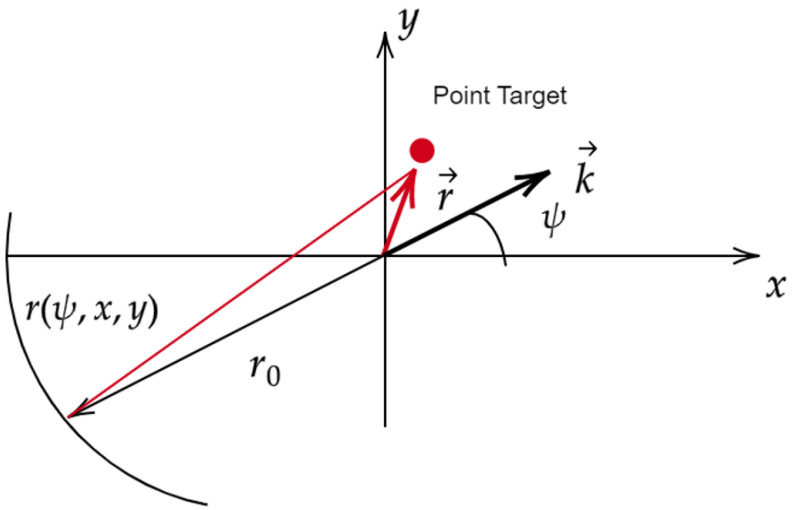

FIGURE 2.6: Turntable Imaging [E20].

expressed in the k-space as

$$s\left(k_r, R\right) = e^{-j2k_r R}. \tag{2.31}$$

This is known as the 'normal form' for a point scatterer at a range R, and is later used for deriving the ISAR signal model.

2.3 Basics of SAR and ISAR imaging

A detailed description of the working of SAR and ISAR systems is out of the scope of the thesis. However, since the algorithms developed in this work are tested on measurements obtained using SAR and ISAR systems, a brief description of only the relevant subtopics are provided in this section. A detailed description of the working principles of SAR and ISAR systems may be found in [S99a].

2.3.1 ISAR imaging

In ISAR, the target is in motion while the radar is stationary. Since such conditions can be created by placing a target on a rotating turntable , as shown in Fig. 2.6, it suffices to use turntable imaging as a reference for ISAR in this work.

Consider the target to be moving with a fixed rotational speed ω. The rotation is limited to the $x-y$ plane and no z-component is present. It is assumed that the radar is working in the far-field and the distance of the target to the radar, r_0, is much larger than the size of the target. The center of the $x-y$ coordinate system lies in the geometric center of the target and the x-axis corresponds to the line of sight (LOS) of the radar for an azimuth angle $\psi = 0$.

Assume a point scatterer at (x, y) in this $x-y$ coordinate system. For $r_0 \gg x, y$, the distance of the scatterer to the radar can be approximated as

$$\begin{aligned} r\left(\psi, x, y\right) &= \sqrt{\left(r_0 \cos\psi + x\right)^2 + \left(r_0 \sin\psi + y\right)^2} \\ &\approx r_0 + x\cos\psi + y\sin\psi\ . \end{aligned} \tag{2.32}$$

This can be substituted in the normal form in (2.31). In order to derive the signal model in the local coordinates x, y, the distance r_0 is subtracted from the scatterer range by multiplication with $e^{-j2k_r r_0}$. Therefore, the normal form of a scatterer in x, y coordinates is given by

$$s\left(k_r, \psi, x, y\right) = e^{-j2k_r\left(r(\psi,x,y)-r_0\right)} \approx e^{-j2k_r\left(x\cos\psi + y\sin\psi\right)} \ . \tag{2.33}$$

To calculate the received signal from the model, the target is assumed to be represented by the reflectivity distribution $a(x, y)$. With this distribution, the received noise-free signal can be written as

$$y\left(k_r, \psi\right) \approx \int\int e^{-j2k_r\left(x\cos\psi + y\sin\psi\right)} a\left(x, y\right) dxdy \ . \tag{2.34}$$

This is followed by a variable substitution step known as polar reformatting. The substitutions are given by

$$\begin{aligned} k_x &= 2k_r\cos\psi \ , \\ k_y &= 2k_r\sin\psi \ . \end{aligned} \tag{2.35}$$

Based on these definitions k_r and ψ can be expressed by

$$\begin{aligned} k_r &= \frac{1}{2}\sqrt{{k_x}^2 + {k_y}^2} \ , \\ \psi &= \text{atan2}\left(k_x, k_y\right) \ . \end{aligned} \tag{2.36}$$

Substituting these representations of k_r and ψ in (2.34), the received signal is given by

$$y\left(k_x, k_y\right) = \int\int e^{-j\left(k_x x + k_y y\right)} a\left(x, y\right) dxdy. \tag{2.37}$$

(2.37) corresponds to the spatial Fourier Transform of $a\left(x, y\right)$ in the variables k_x and k_y. This implies that an estimate of the target reflectivity $a\left(x, y\right)$ can be obtained by an inverse Fourier Transform of the received signal over a range of aspect angles. The range resolution of the estimate remains as described in (2.8), while the cross-range resolution depends on the range of aspect angles and is given by

$$\Delta CR = \frac{\lambda_0}{2\psi_{int}}, \tag{2.38}$$

where, λ_0 is the wavelength of the carrier frequency, and ψ_{int} is the covered range of all aspect angles, also called the integration angle.

In practice, a Fast Fourier Transform (FFT) is used to obtain the target estimate. However, a normal FFT works in rectangular coordinates, while ISAR imaging involves sampling on a circular ring segment. Therefore, a direct FFT leads to blurring effects, specially for large spans of the aspect angle. To avoid this effect, the standard procedure is to perform an interpolation from polar coordinates to a rectangular grid. This is called the Polar Format Processing. Nevertheless, the direct application of the FFT is also quite popular, since the errors that occur due to the wrong grid are negligible compared to errors due to imperfect knowledge of the target motion. The direct application of the FFT without interpolation is known as Range-Doppler processing. In this thesis, the algorithms are applied to images obtained using Polar Format Processing .

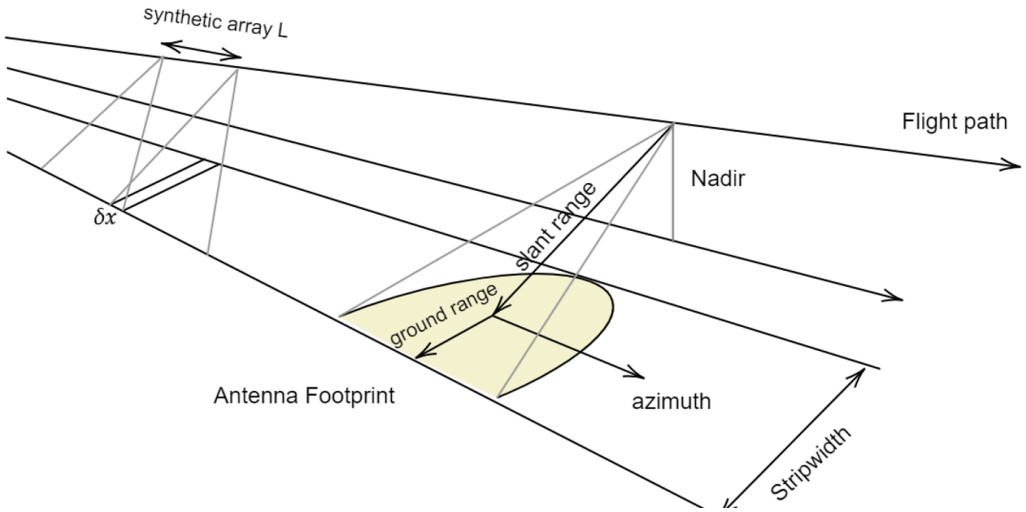

FIGURE 2.7: Synthetic Aperture Radar in Stripmap mode [E20].

2.3.2 SAR imaging

SAR Terminology

Based on Fig. 2.7, some terms commonly used in SAR are explained. Ideally, the platform moves along a straight line. The antenna is mounted to achieve a side looking geometry , i.e., the beam points orthogonal to the motion direction - or with a certain squint angle - to the earth surface. The look direction is tilted by the depression angle from the horizontal plane downwards. The area on ground covered by the antenna main beam is called antenna footprint .

A SAR mission may operate in different modes, and a detailed explanation may be found in [S99a]. In the 'stripmap' mode, the goal is to image a strip of a certain swath width slipped by the antenna footprint. In the 'spotlight' mode, the aim is to image a smaller area with finer resolution, and this is done by fixing the beam center is to a certain point on the earth surface. A high resolution in range is obtained by modulated transmit signals and pulse compression. It is important to differentiate between the range in the line-of-sight, which is called the slant range, and the range projected to the earth surface, known as the ground range. The ground range resolution is coarser than the slant range resolution.

To obtain sufficient resolution parallel to the flight direction, the beamwidth of the antenna for real aperture imaging has to be narrow enough, which requires the antenna length to be some hundreds or thousands of meters. This is not possible in practice. To overcome this handicap, the principle of a synthetic aperture is used, i.e, the motion of the platform is used to generate a synthetic aperture. By the platform's movement, time is transformed into space - a synthetic array is spanned, the recorded echoes are processed similar as for a real array by summing up the returns after compensating the phases. In this way a synthetic beam is generated leading to a fine resolution in azimuth direction.

SAR as Synthetic Antenna

Consider a synthetic array generated by the motion of the platform with velocity V at a pulse repetition interval ΔT. The positions of this synthetic array are $\xi_n = -\infty, \ldots, \infty$, with the spacing $\Delta x = V\Delta T$. Fig. 2.8 shows the principle of a synthetic

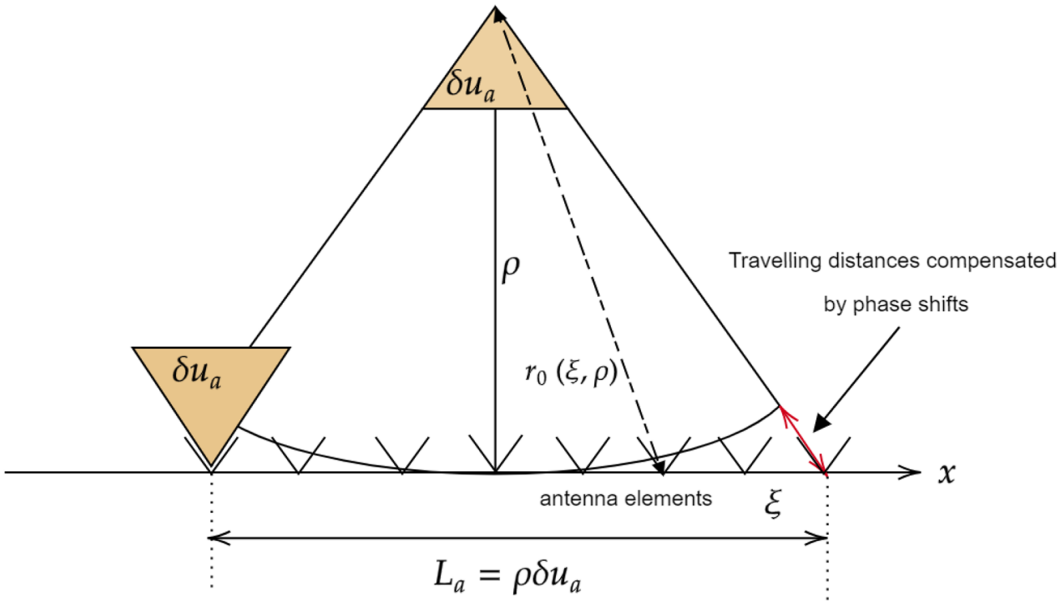

FIGURE 2.8: Focused SAR as synthetic array [E20].

array. Let a point scatterer be placed at the x-coordinate $x = 0$ at a distance ρ to the flight path. By compensation of the phases effected by the varying distances from the scatterer to the elements of the synthetic array, the received signals can be focused to this point. Since, the length of the synthetic array is not restricted according to the far field conditions, the phase terms of higher orders need to be accounted for. The distance of an element of this synthetic array at position ξ to the point scatterer is given by $r_0\,(\xi;\rho) = \sqrt{\rho^2 + \xi^2}$.

To focus a beam to the scatterer, the phase $\psi\,(\xi;\rho) = -2k_r r_0\,(\xi;\rho)$ has to be compensated by a 'phase shifter'. Since the array is synthetic, this phase shift has to be performed in the processor. If all elements of the synthetic array along a synthetic aperture of size L_x are taken into account, a beam is generated with a beamwidth in terms of directional cosine of size $\delta u = \frac{\lambda}{2L_x}$. The achieved resolution of the scene in direction of the flight (azimuth resolution) will be $\delta x = \rho \delta u = \rho \frac{\lambda}{2L_x}$. This requires that the scatterer is illuminated during the whole time where the platform is moving along the synthetic aperture of length L_x. If the antenna has a fixed look direction - as is the case for stripmap mode - and has the real beamwidth δu_a, only a restricted azimuth length L_a of the scene is illuminated,i.e. the azimuth length of the antenna footprint. This length is given by $L_a = \rho \delta u_a$.

For stripmap SAR, the distance the platform is flying from a scatterer entering into the mainbeam until its disappearance is La, too. So for this mode, the length of the synthetic array L_x is bounded by $L_x \leq L_a$. Consequently, the achievable azimuth resolution for stripmap SAR is

$$\delta x_{\min} = \rho \frac{\lambda}{2L_a} = \rho \frac{\lambda}{2\rho \delta u_a} = \frac{\lambda}{2\delta u_a}. \tag{2.39}$$

Using $\delta u_a = \frac{\lambda}{l_x}$ for the beamwidth of an antenna with real aperture l_x, in (2.39),

$$\delta x_{\min} = \frac{\lambda}{2\delta u_a} = \frac{\lambda}{2\lambda l_x} = \frac{l_x}{2}. \tag{2.40}$$

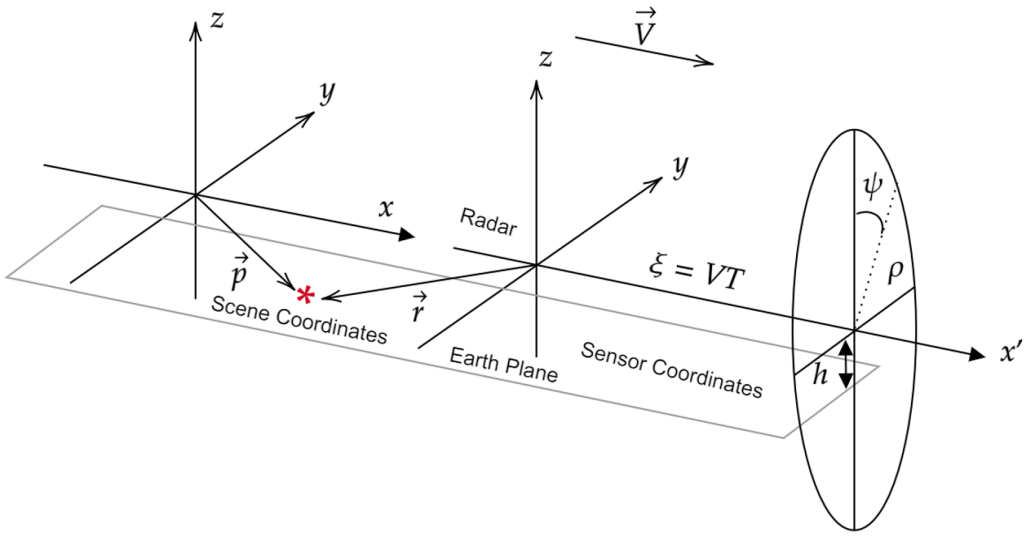

FIGURE 2.9: Cylinder coordinates (x, ρ, v) for the description of signals from point scatterers [E20].

The key takeaway is that the minimum obtainable azimuth resolution of a SAR in stripmap mode with an antenna of length l_x is independent on the range and the wavelength equal to the half length of the antenna.

2.3.3 SAR Geometry-cylinder coordinates and dimensions

The three dimensional SAR geometry can be reduced to two dimensions if the flight path is considered to be a straight line. This transition in coordinates serves the basis of the derivation of the signal model from the scatterer model. The three dimensional geometry is illustrated in Fig. 2.9. The phase center of the antenna is placed in the origin of the sensor coordinate system (x', y, z), which is identically orientated as the scene coordinate system (x, y, z). The platform moves at an altitude h with the constant velocity $\vec{V}$ in direction of the x-axis, so the phase center is at the time T at the position $\vec{R}(T) = (VT, 0, 0)^t$ measured in the scene coordinate system. We denote the x-component with $\xi = VT$. A scatterer at the position $\vec{p}$ in sensor coordinates is seen by the radar at the vector $\vec{r}(\xi)$ whose length depends only on the x-position and the slant range $\rho = \sqrt{y^2 + z^2}$. Therefore, it is convenient to introduce a cylindrical coordinate system (x, ρ, v), where the third parameter, the elevation angle does not influence the range function. It merely modulates the signal amplitude by the antenna characteristics. So, ignoring the elevation, the geometry can be reduced to two dimensions, (x, ρ) and (x', ρ).

Let the position of a fixed scatterer be at (x, ρ). Range and directional cosine to this scatterer as functions of ξ are given by

$$r(\xi; x, \rho) = \sqrt{(x - \xi)^2 + \rho^2}\,, \tag{2.41}$$

and

$$u(\xi; x, \rho) = \frac{x - \xi}{r(\xi; x, \rho)}\,, \tag{2.42}$$

where, $u(\xi; x, \rho) = \cos\alpha(\xi; x, \rho)$ is the x-component of the LOS vector $u(\xi; x, \rho)$ pointing to the scatterer, where α is the cone angle between x-axis and scatterer.

The range and directional cosine functions of ξ are called the range history and the directional cosine history. If a scatterer is considered at $x = 0$, its histories are representative for any scatterer with an arbitrary x-coordinate, since they only have to be shifted in the ξ-variable by x to get the histories of this scatterer. Consequently the representative histories are given by $r_0(\xi;\rho) = r(\xi;0,\rho)$ and $u_0(\xi;\rho) = u(\xi;0,\rho)$, so $r(\xi;x,\rho) = r_0(\xi - x;\rho)$ and $u(\xi;x,\rho) = u_0(\xi - x;\rho)$. From the geometry, the following expressions are obtained

$$r_0(\xi;\rho) = \sqrt{\xi^2 + \rho^2}\,, \quad u_0(\xi;\rho) = -\frac{\xi}{r_0(\xi;\rho)} \tag{2.43}$$

2.3.4 The signal in two dimensions

Consider $s(r)$ to be the transmitted signal, written as a function of the spatial variable r defined in the previous section. The SAR signal in the (ξ, r) plane from a scatterer at (x, ρ) can be expressed as follows:

$$s^{\xi,r}(\xi, r; x, \rho) = s\left(r - r_0(\xi - x;\rho)\right) e^{-j2k_0 r_0(\xi - x;\rho)} D(u_0(\xi - x;\rho)), \tag{2.44}$$

where k_0 is the wave number corresponding to the carrier frequency f_0, and $D(.)$ refers to the two-way antenna characteristics.

As an aside, if the transmitted signal is a chirp, $s(r)$ is expressed in the spatial variable r as

$$s(r) = \text{rect}\left(\frac{r}{r_s}\right) e^{j\alpha\pi\left(\frac{r}{r_s}\right)^2}, \tag{2.45}$$

where, the time duration of the chirp t_s is transferred to the spatial extension $r_s = \frac{t_s c}{2}$. Based on this, (2.44) becomes

$$s^{\xi,r}(\xi, r; x, \rho) = \text{rect}\left(\frac{r - r_0(\xi - x;\rho)}{r_s}\right) e^{j\alpha\pi\left(\frac{r - r_0(\xi - x;\rho)}{r_s}\right)^2} e^{-j2k_0 r_0(\xi - x;\rho)} D(u_0(\xi - x;\rho)). \tag{2.46}$$

In the two-dimensional representation of the SAR signal in (2.46), it is observed that the range shifted transmitted chirp is multiplied with the azimuth chirp in the ξ dimension.

Next, an application of the Fourier Transform along the r dimension transfers the signal from the (ξ, r) domain to the (ξ, k_r) domain. The resultant signal model is as follows:

$$s^{\xi,k_r}(\xi, k_r; x, \rho) = e^{-j2k_r r_0(\xi;\rho)} D\left(u_0(\xi;\rho)\right). \tag{2.47}$$

Similarly, a spatial Fourier Transform along ξ gives

$$\begin{aligned} s^{k_x,k_r}(k_x, k_r; x, \rho) &= e^{-jk_x x} s^{k_x,k_r}(k_x, k_r; 0, \rho) \\ &= e^{-jk_x x} \int e^{-jk_x \xi} e^{-j2k_r r_0(\xi;\rho)} D(u_0(\xi;\rho)) d\xi\,. \end{aligned} \tag{2.48}$$

2.3.5 SAR processing

Principally, the raw 2D data could be processed to an image optimally, if for each possible position of a point scatterer, the two-dimensional normalized matched filter for the model signal is applied. However, this leads to a very large computational load. To avoid this, popular SAR processors exist where the range compression and

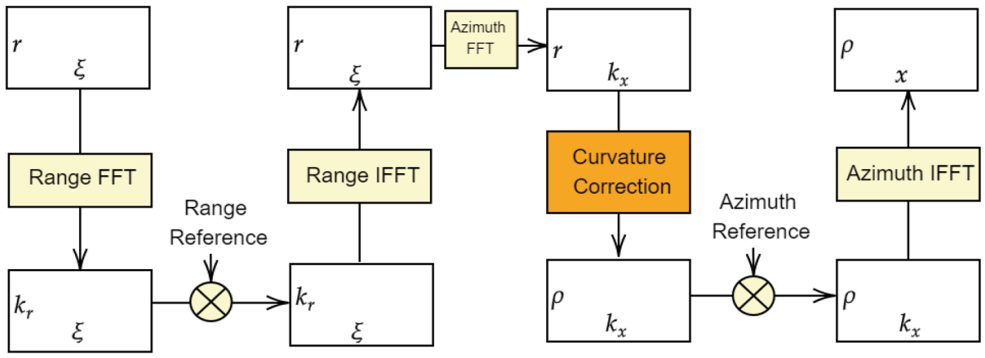

FIGURE 2.10: Range Doppler Processor.

azimuth compression are usually applied one after the other. This section briefly discusses two of the major processors: Range-Doppler processor and Omega-k processor. A more detailed discussion on SAR processors is out of the scope of this work and can be found in [S99b].

Range-Doppler Processor

The Range-Doppler processor starts with the classical range compression performed in the range frequency domain. After range compression, the echoes of a point scatterer are not aligned in a straight row of the data matrix, but will migrate through the range lines due to the hyperbolic variation of range along slow time. This is called the range curvature problem. To solve this, first the data is transformed by an azimuth FFT into the k_x domain which was introduced in Section 2.3.4. The signals of scatterers with the same ρ but varying x-coordinates are shifted in slow time; but by the Fourier transform, the paths in the k_x-domain are overlayed. Therefore, the range curvature correction can be performed in the k_x-domain simultaneously.

The phase for a certain k_x can be transferred to the range by

$$r\left(\xi_0, \rho\right) = \frac{\rho\sqrt{4{k_r}^2 - {k_x}^2}}{2k_r}. \tag{2.49}$$

From this, the variation of range over k_x is obtained. All echoes are shifted back to the value ρ. This can be performed either by interpolation or by an approximate range curvature relating to the mean distance which can be executed in the range frequency domain. Only for the reference ρ the correction is perfect. For smaller or larger slant ranges, errors can be neglected while for others,a procedure called differential range correction has to be performed. Finally, the azimuth compression is completed by fast convolution along the rows. Fig. 2.10 gives the block diagram for a Range-Doppler Processor.

Omega-k Processor

The signal of a point scatterer at (x, ρ) in the k_x, k_r-domain was given in (2.48). Using the principle of stationary phase, a simpler approximation of (2.48) is given by

$$s^{k_x,k_r}(k_x, k_r; x, \rho) \approx C(k_x) e^{-j(k_x x + \rho\sqrt{4{k_r}^2 - {k_x}^2})} D\left(\frac{k_x}{2k_r}\right) . \tag{2.50}$$

Therefore, the data will be the superposition of these signals with the azimuth reflectivity:

$$\begin{aligned} z^{k_x,k_r}(k_x, k_r) &= \int\int s^{k_x,k_r}(k_x, k_r; x, \rho)\, a(x, \rho)\, dx d\rho \\ &\approx C(k_x) \int\int e^{-j(k_x x + \rho\sqrt{4{k_r}^2 - {k_x}^2})} D\left(\frac{k_x}{2k_r}\right) a(x, \rho)\, dx d\rho . \end{aligned} \tag{2.51}$$

Using $k_\rho = \sqrt{4{k_r}^2 - {k_x}^2}$, and performing the substitution

$$z^{k_x,k_\rho}(k_x, k_\rho) = z^{k_x,k_r}\left(k_x, 2\sqrt{{k_x}^2 + {k_\rho}^2}\right) , \tag{2.52}$$

the data in the k_x, k_ρ domain is given by,

$$\begin{aligned} z^{k_x,k_\rho}(k_x, k_\rho) &\approx C(k_x)\, D\left(\frac{k_x}{\sqrt{{k_x}^2 + {k_\rho}^2}}\right) \int\int e^{-j(k_x x + k_\rho \rho)} a(x, \rho) dx d\rho \\ &= C(k_x)\, D\left(\frac{k_x}{\sqrt{{k_x}^2 + {k_\rho}^2}}\right) A(k_x, k_\rho) , \end{aligned} \tag{2.53}$$

with $A(k_x, k_\rho)$ being the two dimensional Fourier Transform of the reflectivity. Therefore, the substitution transfers the data from the (k_x, k_r) domain into the 2D Fourier Tranform of the reflectivity distribution, modulation by the antenna characteristics. Stolt interpolation is applied to transfer the grid in (k_x, k_r) domain to (k_x, k_ρ) domain. Finally, only a two dimensional inverse Fourier Transform is required to obtain the focused SAR image. Fig. 2.11 gives the block diagram for the Omega-k processor.

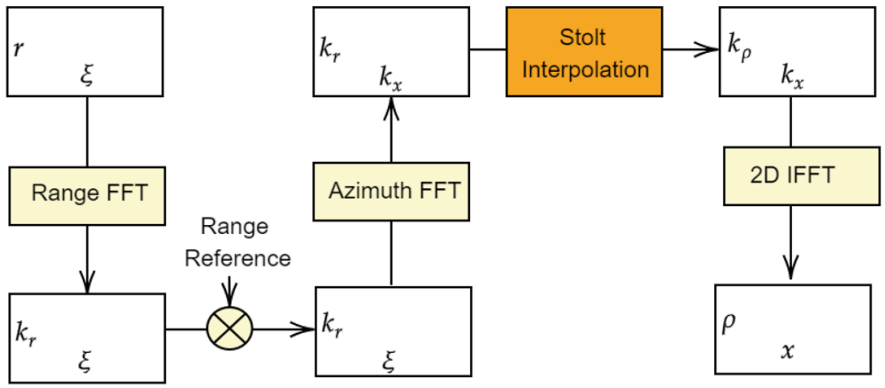

FIGURE 2.11: Omega-k processor.

Chapter 3

Basics of Compressed Sensing

In the last few years, the notion of 'sparsity' or 'sparse representation' has become popular across multiple research areas in signal processing, machine learning and any application involving optimization. Closely tied to this idea of sparsity is the now well-established theory of Compressed Sensing (CS) [D06]. In this chapter, an overview of these concepts is presented. A very important metric of evaluation of CS sensing matrices, namely the coherence parameter, is discussed. Improvement of this parameter becomes a major focus of a large part of the work done in this thesis.

3.1 The Signal: Sparsity and Compressibility

'Sparsity' of a signal refers to the maximum number of non-zero elements needed to represent the signal in a certain basis. Let $\mathbf{x}$ be a vector representing a sparse signal. The support of a vector, supp, refers to the set of indices corresponding to the non-zero elements in the vector. The l_0 norm of vector $\mathbf{x}$ is given by

$$\|\mathbf{x}\|_0 := \lim_{p \to 0} \|\mathbf{x}\|_p^p = |\text{supp}\,(\mathbf{x})|, \tag{3.1}$$

which refers to the cardinality of the support of vector $\mathbf{x}$. $\mathbf{x}$ is known as an 's-sparse vector' if

$$\|\mathbf{x}\|_0 \leq s. \tag{3.2}$$

A more relaxed version of the concept of sparsity is 'compressibility'. A vector is said to be compressible if the error of its best s-term approximation decays quickly in s. This means that the vector has s significantly large coefficients that can be used to get the best s-term approximation.

By extension, the concept of sparsity or compressibility holds true when dealing with a collection of vectors, i.e., a matrix. In the current work, 'sparsity of a scene' being detected by a radar system comes up in the later chapters. This refers to the fact that the 2D matrix of scene reflectivities is 'sparse', i.e., the number of non-zero reflectivities are small in comparison to the dimension of the grid used to discretize the scene.

It is found that most signals in nature are sparse in some domain, i.e., they can be represented by a small (sparse) number of non-zero components without loss of important information. From this idea, stems the hunt for 'sparse representation' of a signal. The main idea behind the theory of CS is this hunt for the best sparse representation of a signal in a given basis, given a reduced set of measurements.

3.2 The Sampling: why CS is necessary

But why is such a sparse representation necessary in the first place? In order to understand the importance of sparse representation and CS, it is necessary to briefly focus on the sampling of a signal.

The famous Shannon sampling theorem, also called Nyquist-Shannon theorem (Theorem 1 of [S49]), states that, if a function, defined in time domain over a certain interval, contains no frequencies higher than $f_{\max}$, it is completely determined by equally-spaced temporal samples at a rate $2f_{\max}$ (considering real-valued signals). The proof given in [S49] is based on the fact that a sampling in the time domain at this rate is sufficient to determine the Fourier transform of the signal, provided that it is only non-zero in the frequency interval $[-f_{\max}, f_{\max}]$. If the signal in the frequency domain is determined, it follows that it is also completely determined in the time domain. Similarly, the sampling rate needed for a complex-valued signal in the same frequency-interval is found to be $f_{\max}$.

This sampling rate is known as the Nyquist-rate, and is a widespread standard for the sampling of any band-limited signal. However, with the recent advent of high resolution imaging, there is a need to sample large volumes of high frequency data. Nyquist-rate sampling, in this case, gives rise to an excessive volume of data that cannot be transmitted, stored or analyzed effectively. This leads to the original idea of 'compression' after sampling, i.e., a lot of data samples gathered in the sensing step have to be condensed into few in the compression step, so that the data can be processed effectively. In other words, the sensor gathers redundant information.

To prevent this wastage of effort at sampling, the concept of compressive sensing was introduced. It entails compression at sensing and not after sensing. In other words, the sensing gathers only non-redundant information. Differently from the Shannon sampling theorem, that requires the signal to be band-limited, CS theory is more general and requires the signal to be sparse in some known basis. Depending on the signal sparsity, the number of measurements required to achieve lossless reconstruction might be much lower than that suggested by the Nyquist rate.

Based on this traditional view of 'Compression at Sensing', the problem can also be examined from a different perspective. What if this compression at sensing is forced by environmental conditions or lack of resources? By the same logic, reconstruction should still be possible, if the signal is sparse in some domain. In recent years, such a 'forced compression at sensing' has been caused by an exponential rise in spectrum congestion [LMP+20]. The frequency spectrum is becoming a scare resource that needs to be efficiently used. This has given rise to many spectrum-efficient approaches such as spectrum sharing and joint communication and sensing. These approaches explicitly place a limitation on the number of samples that can be obtained in the sensing stage, thereby making the use of smart sensing schemes like CS more popular.

3.3 The Sensing Matrix: CS Formulation

Any CS problem consists of three main components: the signal to be reconstructed, the sensing matrix (composed of the measurement matrix and the sparsifying basis) and the signal reconstruction method. This section provides the general mathematical formulation of a CS problem.

Let, the vector $\mathbf{z} \in \mathbb{C}^N$ represent a complex-valued signal with N samples that has to be sensed. $\mathbf{z}$ is represented using a weighted linear combination of a number

of elementary signals. These elementary signals constitute the columns of a matrix $\boldsymbol{\psi} \in \mathbb{C}^{N \times N}$, which is commonly known as the 'basis'. The weighting of these elementary signals are represented by the non-zero coefficients of the true sparse vector $\mathbf{x_0} \in \mathbb{C}^N$, corresponding to $\mathbf{z}$. Consolidating this in an expression gives

$$\mathbf{z} = \boldsymbol{\psi}\mathbf{x_0}. \tag{3.3}$$

Thus the sparsifying basis $\boldsymbol{\psi}$ transforms the dense signal $\mathbf{z}$ into its true sparse representation $\mathbf{x_0}$.

Till now, only the signal has been taken into consideration. The next important component of the CS formulation is the measurement process, encapsulated in the measurement matrix $\boldsymbol{\phi} \in \mathbb{C}^{m \times N}$. Consider, as before, the signal $\mathbf{z} \in \mathbb{C}^N$ to be sensed in the original domain. The measurement vector $\mathbf{y} \in \mathbb{C}^m$ is obtained by collecting m discrete measurements of $\mathbf{z}$, where typically $m \ll N$. The measurements are gathered via the sensing process which is represented by matrix $\boldsymbol{\phi}$. This can be written as,

$$\mathbf{y} = \boldsymbol{\phi}\mathbf{z}. \tag{3.4}$$

Combining (3.3) and (3.4) gives

$$\begin{aligned} \mathbf{y} &= \boldsymbol{\phi}\boldsymbol{\psi}\mathbf{x_0} \\ &= \boldsymbol{A}\mathbf{x_0}, \end{aligned} \tag{3.5}$$

where, $\boldsymbol{A} \in \mathbb{C}^{m \times N}, m \ll N$. Matrix $\boldsymbol{A}$ represents the measurement process as well as the transformation by the sparsifying basis and is commonly known as the sensing matrix.

(3.5) gives the general CS formulation. It presents a system of linear equations that is typically highly under-determined and therefore, cannot be directly solved. An alternative to a direct inversion that can be used is the pseudo-inversion or the Moore-Penrose inversion. However, this approach does not take into account that the vector $\mathbf{x_0}$ is sparse, and leads to a dense final estimate $\hat{\mathbf{x}}$ having non-zero weights for many of its coefficients.

A better but idealistic approach is the minimization of the l_0 norm of $\mathbf{x}$, i.e.,

$$\hat{\mathbf{x}} = \arg\min \|\mathbf{x}\|_0 \;\; s.t. \;\; \mathbf{y} = \boldsymbol{A}\mathbf{x} \; . \tag{3.6}$$

But minimizing the l_0 norm is NP-hard [NSI+19] and the main way to tackle this is by using the convex relaxation of the l_0 norm, i.e., the l_1 norm minimization, given by

$$\hat{\mathbf{x}} = \arg\min \|\mathbf{x}\|_1 \;\; s.t. \;\; \mathbf{y} = \boldsymbol{A}\mathbf{x} \; . \tag{3.7}$$

In practice, the measurement vector $\mathbf{y}$ is always affected by noise, and therefore, the equality condition in (3.7) is too strict and may lead to a non-optimal solution. The extension of (3.7) to the noisy scenario gives

$$\hat{\mathbf{x}} = \arg\min \|\mathbf{x}\|_1 \;\; s.t. \;\; \|\boldsymbol{A}\mathbf{x} - \mathbf{y}\|_2 \leq \eta \; , \tag{3.8}$$

where η is the l_2 norm of the noise vector in the measurement domain.

3.4 Metrics to determine the quality of the Sensing Matrix

In theory, the sensing matrix $\boldsymbol{A}$ is required to fulfill certain conditions to ensure a successful reconstruction of the desired vector $\mathbf{x}$. This section briefly discusses these conditions, namely the Null Space Property (NSP), the Restricted Isometric Property (RIP), and a very important engineering workaround to the RIP, i.e., the coherence.

The null space of a matrix $\boldsymbol{A}$ is defined as the set of vectors that are projected to the zero vector by it, i.e.,

$$\mathcal{N}(\boldsymbol{A}) := \{\mathbf{x} | \boldsymbol{A}\mathbf{x} = 0\}. \tag{3.9}$$

Let $\mathbf{p}$ and $\mathbf{q}$ be two distinct s-sparse vectors of length N, and $\mathbf{p}, \mathbf{q} \in \sum_s$, where $\sum_s$ denotes the subset of $\mathbb{C}^N$ containing all s-sparse vectors. Their difference vector is $(\mathbf{p} - \mathbf{q}) \in \sum_{2s}$. The uniqueness of a reconstructed sparse vector can be ensured only if $\mathcal{N}(\boldsymbol{A}) \cap \sum_{2s} = 0$. This means that the same $\mathbf{y}$ cannot be obtained from different $\mathbf{x}$ vectors, since that would make it impossible to uniquely recover the signal.

Extending this idea to 'compressible vectors', there must exist only one 'most compressible' vector for a certain cardinality of the vector support, so that the uniqueness of the solution holds. Based on this idea, the matrix $\boldsymbol{A}$ is said to satisfy the Null Space Property relative to a set $S \subset [N]$ if for any vector $\mathbf{v} \in \mathcal{N}(\boldsymbol{A})$

$$\|\mathbf{v}_S\|_1 < \|\mathbf{v}_{\bar{S}}\|_1. \tag{3.10}$$

If (3.10) is satisfied for all S with $\text{card}(S) \leq s$, it is said to satisfy the null space property of order s. If the matrix $\boldsymbol{A}$ satisfies the null space property of order s, it means that there exists a unique s-sparse solution of (3.7) having a minimal l_1 norm.

The sensing matrix $\boldsymbol{A}$ is said to satisfy the Restricted Isometric Property (RIP) of order s if there exists $\delta_s \in (0, 1)$ such that

$$(1 - \delta_s) \leq \frac{\|\boldsymbol{A}\mathbf{x}\|_2^2}{\|\mathbf{x}\|_2^2} \leq (1 + \delta_s) \tag{3.11}$$

for all $\|\mathbf{x}\|_0 \leq s$. The RIP condition ensures that any subset of s columns of $\boldsymbol{A}$ consists of vectors which are nearly orthogonal. If the matrix satisfies the RIP of order $2s$, then it implies that two different s-sparse vectors will not map to the same measurement vector $\mathbf{y}$ and their distance is approximately preserved.

This RIP condition provides the foundation for a number of recovery guarantees in CS literature. However, it is almost impossible to use the RIP condition in practice , since it involves checking all the possible combinations of s columns of $\boldsymbol{A}$ to verify if the condition given in (3.11) holds. A metric that provides a practical engineering work around to the RIP is the 'coherence' of the sensing matrix.

The coherence $\mu := \mu(\boldsymbol{A})$ of a matrix $\boldsymbol{A}$ is defined as

$$\mu := \max_{1 \leq i \neq j \leq N} \frac{|\langle \mathbf{a_i}, \mathbf{a_j} \rangle|}{\|\mathbf{a_i}\| \|\mathbf{a_j}\|}, \tag{3.12}$$

where, $\mathbf{a_i}$ denotes the i^{th} column of $\boldsymbol{A}$. It gives the maximum correlation between any two columns of the matrix $\boldsymbol{A}$. The coherence value represents the dependence or similarity between the columns in a sensing matrix. A low value of coherence implies that the columns are nearly orthogonal and therefore, a low coherence (or high incoherence) is always desired for a better sparse reconstruction.

Intuitively, this can be explained as follows. The l_1-norm minimization attempts to provide a sparse $\mathbf{x}$ by concentrating the non-zero weights only on certain columns of $\boldsymbol{A}$, such that the resultant linear combination can best describe the signal $\mathbf{y}$. If the

columns are similar, such a concentration of energy on specific columns to obtain a unique representation of $\mathbf{y}$ is difficult. Similar non-zero weights will be assigned to the similar columns, causing a failure of the l_1-minimization. There are many theoretical results associated with coherence, and the most relevant ones are briefly described in this section.

A popular way to visualize the coherence is by using the Gram matrix, $\boldsymbol{G}$, of $\boldsymbol{A}$, which is defined as

$$\boldsymbol{G} = \boldsymbol{A}^H \boldsymbol{A}. \tag{3.13}$$

If the columns of $\boldsymbol{A}$ are normalized, the coherence can be directly obtained by finding the maximum of the absolute values of the off-diagonal elements of $\boldsymbol{G}$, i.e.,

$$\mu(\boldsymbol{A}) = \max_{i \neq j} |g_{i,j}|, \tag{3.14}$$

where $g_{i,j}$ denotes the element in the i^{th} row and j^{th} column of $\boldsymbol{G}$. The maximum value of μ is 1 for two identical columns, while the minimum bound is given by

$$\mu(\boldsymbol{A}) \geq \sqrt{\frac{m-N}{N(m-1)}}, \tag{3.15}$$

which is commonly known as the Welch bound and is 0 for a square matrix $(m = N)$. From the coherence of $\boldsymbol{A}$, a bound on the spark, which is defined as the smallest number of columns of $\boldsymbol{A}$ that are linearly dependent, can be obtained, as shown in (3.16). Provided that the condition $\text{spark}(\boldsymbol{A}) > 2s$ is sufficient to ensure uniqueness of the solution to (3.7) and $|\text{supp}(\mathbf{x})| = s$, (3.16) leads to the sparsity requirement in (3.17), given by

$$\text{spark}(\boldsymbol{A}) \geq 1 + \frac{1}{\mu(\boldsymbol{A})} \tag{3.16}$$

$$s < \frac{1}{2}\left(1 + \frac{1}{\mu(\boldsymbol{A})}\right). \tag{3.17}$$

From (3.17), the coherence requirement for a given sparsity s becomes

$$\mu(\boldsymbol{A}) < \frac{1}{2s-1}. \tag{3.18}$$

(3.17) shows that if the coherence value is low, even not-so-sparse vectors, with higher values of s may be recovered successfully. This is apparent if the extreme case is considered, where $\mu = 0$ and $m = N$. In such a case, there exists a one-to-one mapping between $\mathbf{x}$ and $\mathbf{y}$, and thus, $\mathbf{x}$ may be recovered irrespective of its sparsity.

For a small coherence value of $\mu(\boldsymbol{A}) < \frac{c}{\sqrt{m}}$, the condition from (3.18) is satisfied if the number of measurements,

$$m \geq Cs^2, \tag{3.19}$$

where $C > 0$ is a constant. The coherence parameter may also be used to ensure that $\boldsymbol{A}$ satisfies the RIP condition. If

$$\delta_s = (s-1)\,\mu(\boldsymbol{A}),\ s < \frac{1}{\mu(\boldsymbol{A})}, \tag{3.20}$$

then $\boldsymbol{A}$ satisfies the RIP condition with order s and restricted isometry constant δ_s.

3.5 Classes of CS Algorithms

There are many approaches to solve (3.5) in order to obtain the sparsest representation of $\mathbf{x}$. This section provides an overview of the three main classes of algorithms that are used to solve the CS problem, namely:

1. Greedy approaches
2. Convex-optimization based approaches
3. Iterative Thresholding based approaches

3.5.1 Greedy Approaches

These approaches use locally optimal or 'greedy' decisions at every iteration to construct an estimate $\hat{\mathbf{x}}$ of the sparse vector $\mathbf{x}$. Most algorithms belonging this category proceed in two main steps:

- Projection of the residual: The residual $\mathbf{r} = \mathbf{y} - \boldsymbol{A}\hat{\mathbf{x}}$ is projected over the sensing matrix $\boldsymbol{A}$,
$$\mathbf{c} = \boldsymbol{A}^H \mathbf{r}. \tag{3.21}$$
For the first iteration, $\hat{\mathbf{x}}$ is an initial estimate which depends on the specific scenario or algorithm used.
- Updating $\hat{\mathbf{x}}$: The elements of $\mathbf{c}$ having the largest magnitudes are selected and used to determine the current support, supp, for $\hat{\mathbf{x}}$. The coefficients of $\hat{\mathbf{x}}$ are updated for the minimization of the data fidelity term $\|\mathbf{y} - \boldsymbol{A}_{\text{supp}}\hat{\mathbf{x}}_{\text{supp}}\|_2^2$.

Since greedy methods are not the focus of this work, only the most popular greedy algorithm, i.e., the Orthogonal Matching Pursuit (OMP), is discussed in this section. The main steps of OMP are shown in Algorithm 1.

Algorithm 1: Orthogonal Matching pursuit (OMP)

Input: $\mathbf{y}$, $\boldsymbol{A}$, η, N_{it}
Initialization: $\hat{\mathbf{x}}^{[0]} = 0$, $\mathbf{r}^{[0]} = \mathbf{y}$, $\text{supp}\left(\hat{\mathbf{x}}^{[0]}\right) = \{\}$, $it = 1$
Result: $\hat{\mathbf{x}}^{[it]}$, $\mathbf{r}^{[it]}$
while *stopping criteria not met* **do**
  $\mathbf{c}^{[it]} = \boldsymbol{A}^H \mathbf{r}^{[it-1]}$;
  $i^{[it]} = \arg\max_i |c_i^{[it]}| / \|\boldsymbol{A}_i\|_2$;
  $\text{supp}\left(\hat{\mathbf{x}}^{[it]}\right) = \text{supp}\left(\hat{\mathbf{x}}^{[it-1]}\right) \cup i^{[it]}$;
  $\hat{\mathbf{x}}^{[it]}_{\text{supp}\left(\hat{\mathbf{x}}^{[it]}\right)} = \boldsymbol{A}^{\dagger}_{\text{supp}\left(\hat{\mathbf{x}}^{[it]}\right)} \mathbf{y}$, $\hat{\mathbf{x}}^{[it]}_{\text{supp}\left(\overline{\hat{\mathbf{x}}^{[it]}}\right)} = 0$;
  $\mathbf{r}^{[it]} = \mathbf{y} - \boldsymbol{A}\hat{\mathbf{x}}^{[it]}$;
  if $\|\mathbf{r}^{[it]}\|_2^2 \leq \eta$ or $it = N_{it}$ **then**
    stop pursuit
  else
    $it = it + 1$
  end
end

Following the general greedy algorithm structure, the residual $\mathbf{r}$ is projected onto all the columns of the sensing matrix $\boldsymbol{A}$ to obtain the coefficient vector $\mathbf{c}$. The goal is

to remove the highest energy elements from the residual at every step. Therefore, index positions corresponding to the largest elements of $\mathbf{c}$ are added to the support and $\hat{\mathbf{x}}$ is recalculated over the support by $\boldsymbol{A}^{\dagger}\mathbf{y}$, where $\boldsymbol{A}^{\dagger}$ is the Moore-Penrose pseudoinverse $\boldsymbol{A}^{H}(\boldsymbol{A}\boldsymbol{A}^{H})^{-1}$. This allows all the non-zero elements of $\hat{\mathbf{x}}$ to be re-determined at every step. This also ensures that the residual is orthogonal to the currently selected columns of $\boldsymbol{A}$ (hence the name orthogonal matching pursuit), so that the same support index is not re-selected in the next iteration.

3.5.2 Convex-Optimization based Approaches

The relaxation of the l_0 norm to l_1 norm discussed in [E10a] is known as 'convex relaxation'. Such a relaxation allows the use of the convex optimization approach to solve the l_1-minimization problem, and is commonly known as 'basis pursuit' for (3.7), or 'basis pursuit for denoising' for (3.8). A reiteration of the noisy form follows for ease of the reader:

$$\hat{\mathbf{x}} = \arg\min \|\mathbf{x}\|_1 \;\; s.t. \;\; \|\boldsymbol{A}\mathbf{x} - \mathbf{y}\|_2^2 \leq \eta \; . \tag{3.22}$$

This pursuit of the best basis encompasses many algorithms but in this section, the focus is placed on the algorithms that are very popularly used or the ones that have been used in later chapters for performance comparison.

An alternate version of the basis pursuit formulation arises from the statistics and machine learning domain and is popularly known as the Least Angle Selection and Shrinkage Operator (LASSO). It is given by,

$$\hat{\mathbf{x}} = \arg\min_{\mathbf{x}} \|\boldsymbol{A}\mathbf{x} - \mathbf{y}\|_2^2 \;\; s.t. \;\; \|\mathbf{x}\|_1 \leq \tau \tag{3.23}$$

Both (3.22) and (3.23) have the same objective with slight variations arising from the domains in which they are used. In signal processing, information about the noise in the measurement, η is given more importance. On the other hand, in machine learning, the level of sparsity can be determined and as a result an upper bound on the l_1 norm is more suitable.

Both BP and LASSO are open-form constrained problems. An equivalent unconstrained form is given by

$$\hat{\mathbf{x}} = \arg\min_{\mathbf{x}} \|\boldsymbol{A}\mathbf{x} - \mathbf{y}\|_2^2 + \lambda\|\mathbf{x}\|_1 \; , \tag{3.24}$$

where λ is a regularizer that controls the trade-off between the data fidelity term, $\|\boldsymbol{A}\mathbf{x} - \mathbf{y}\|_2^2$ and the sparsity term, $\|\mathbf{x}\|_1$. (3.24) is an important starting point for the algorithms used to solve the BP/LASSO problems. It also reappears in the Iterative Thresholding algorithms discussed in the next section.

Following the widely referenced work from [CDS01], there are four main classes of algorithms used to solve BP.

- Simplex Methods: The simplex method makes the temporal solution walk along the edges of the convex polytope (i.e., a simplex). These methods start by selection of an initial support such that the corresponding $\hat{\mathbf{x}}_0$ has no negative elements. The algorithm works iteratively, by swapping one element in the current support with another not included the set, till the support corresponding to the best l_1 minimization is achieved. Anti-cyclic rules are followed to ensure that the swapping guarantees convergence to an optimal solution. The Frank-Wolfe algorithm falls under the category of simplex methods and

a Frank-Wolfe implementation of Beurling LASSO (BLASSO) has been later used in the thesis [dG12], [LJS+13]. The basic steps of BLASSO are described in Algorithm 2.

- Interior Point Methods: These methods, also called barrier methods, make the solution traverse the interior of the polytope, thus starting from a point that is well inside the interior. Starting with an estimate $\hat{\mathbf{x}}_0 > 0$ which satisfies $\mathbf{y} = \boldsymbol{A}\mathbf{x}$ (or its noisy variations based on the data), these methods iteratively sparsify the solution (eg: via thresholding), until the significant non-zero components stand out.

- Projected Gradient Methods: These methods iteratively move in the direction of the negative gradient, and then project onto a feasible set. In the BP case, the feasible set is determined by the sparsity constraint. This thesis uses a specific implementation of such a method known as the Spectral Projection Gradient (SPG) [BF08], [BF19]. SPG (or SPGL1) solves the BP problem by solving a sequence of LASSO problems for different values of τ. From the solution to the LASSO problem at each step, the gradient of the Pareto curve is determined, which then allows root-finding as detailed in [BF08]. A big advantage of SPGL1 is that it can be used on complex datasets, which is important for the applications discussed in this work.

- Homotopy Methods: A homotopy between two continuous functions, say f and g, is described as a continuous deformation from f into g. In the context of l_1 minimization given in (3.24), λ is the parameter that defines the homotopy. If $\hat{\mathbf{x}}$ is the minimizer, it can be proved that $\hat{\mathbf{x}} = \lim_{\lambda \to 0^+} x_\lambda$. This implies that for a vanishing sequence of values of λ, the homotopy method gives a sequence of minimizers that converges to the solution $\hat{\mathbf{x}}$ [H17].

Algorithm 2: Frank-Wolfe Implementation of Beurling LASSO (BLASSO)

Input: $\mathbf{y}$, $\boldsymbol{A}$, N_{it},T
a**Initialization:** $\hat{\mathbf{x}}^{[\mathbf{0}]} = 0$, $\mathbf{s}^{[\mathbf{0}]} = 0$, $\mathbf{r}^{[\mathbf{0}]} = \mathbf{y}$, $a = \frac{1}{\lambda_{\max}(\boldsymbol{A}^H \boldsymbol{A})}$, $it = 1$
Result: $\hat{\mathbf{x}}^{[\mathbf{it}]}$
while *stopping criteria not met* **do**
  $\gamma = \frac{2}{it+2}$;
  $\nabla^{[\mathbf{it-1}]} = \boldsymbol{A}^H \left(\mathbf{r}^{[\mathbf{it-1}]} \right)$;
  $ind = \underset{ind \in N}{\arg\max} \left(|\nabla^{[it-1]}(ind)| \right)$;
  $\mathbf{s}^{[\mathbf{it-1}]}(ind) = a \, \frac{\left(\nabla^{[\mathbf{it-1}]}(ind)\right)}{|\left(\nabla^{[\mathbf{it-1}]}(ind)\right)|}$;
  $\hat{\mathbf{x}}^{[\mathbf{it}]} = (1-\gamma)\, \hat{\mathbf{x}}^{[\mathbf{it-1}]} + \gamma \mathbf{s}^{[\mathbf{it-1}]}$;
  $\mathbf{r}^{[\mathbf{it}]} = \mathbf{y} - \boldsymbol{A}\hat{\mathbf{x}}^{[\mathbf{it}]}$;
  if $\|\mathbf{r}^{[\mathbf{it}]}\|_2^2 \leq T$ or $it = N_{it}$ **then**
    stop
  else
    $it = it + 1$
  end
end

3.5.3 Iterative Thresholding Approaches

The Iterative Thresholding approaches belong to the class of greedy methods. However, they have been extensively used in the thesis, and are therefore described separately in this section.

The two basic thresholding operators, soft and hard thresholding are first discussed. The hard thresholding operator, $H_T(\mathbf{x})$, assigns the values of all elements below a certain threshold T to 0, i.e.,

$$H_T(\mathbf{x}) = \begin{cases} \mathbf{x}, & \text{for } |\mathbf{x}| \geq T \\ 0, & \text{for } |\mathbf{x}| < T \,. \end{cases} \tag{3.25}$$

The soft thresholding operator, $S_T(\mathbf{x})$, is defined by

$$S_T(\mathbf{x}) = \begin{cases} \frac{\mathbf{x}}{|\mathbf{x}|}(|\mathbf{x}| - T), & \text{for } |\mathbf{x}| > T \\ 0, & \text{else} \,, \end{cases} \tag{3.26}$$

and $\mathbf{S}_T(\mathbf{x})$ represents the vector with the S_T applied to each element of $\mathbf{x}$. Since the hard thresholding is quite straightforward, and Iterative Soft Thresholding Algorithm (ISTA) reappears later in the thesis, this section focuses on discussing the soft-thresholding operation.

Consider $h(\mathbf{x})$ be a cost function which is differentiable for $\mathbf{x} \in \mathbb{C}^N$. The gradient of $h(\mathbf{x})$ maybe given by $g(\mathbf{x}) = \nabla_{\mathbf{x}} h(\mathbf{x})$. Then, a gradient algorithm for minimizing h would follow

$$\mathbf{x^{it+1}} = \mathbf{x^{it}} - \mu g\left(\mathbf{x^{it}}\right) \,, \tag{3.27}$$

where μ controls the gradient step size. From (3.24), the cost function $h(\mathbf{x}) = \arg\min_{\mathbf{x}} \|\boldsymbol{A}\mathbf{x} - \mathbf{y}\|_2^2 + \lambda\|\mathbf{x}\|_1$ is examined. This consists of two parts, $h_1(\mathbf{x}) = \arg\min_{\mathbf{x}} \|\boldsymbol{A}\mathbf{x} - \mathbf{y}\|_2^2$ and $h_2(\mathbf{x}) = \lambda\|\mathbf{x}\|_1$. The gradient method can be applied alternately, i.e., first, the first part is decreased using the gradient g_1 of h_1, resulting in an intermediate value $\tilde{\mathbf{x}}$. Starting with this, the second part is decreased by application of a modified gradient g_2 of h_2 and varying μ over the coefficients.

While the first part is differentiable for all $\mathbf{x} \in \mathbb{C}^N$ with the gradient $g_1(\mathbf{x}) = \nabla_{\mathbf{x}}\|\boldsymbol{A}\mathbf{x} - \mathbf{y}\|_2^2 = \boldsymbol{A}^H(\boldsymbol{A}\mathbf{x} - \mathbf{y})$, the second term $\|\mathbf{x}\|_1 = \sum_{n=1}^{N} |x_n|$ is not differentiable if one or more coefficients of $\mathbf{x}$ are equal to zero. Upon closer inspection of h_2, it is noted that $f(z) = |z|$ with complex z is differentiable everywhere, except for $z = 0$. Precisely:

$$\nabla_z |z| = \begin{cases} \text{undefined}, & \text{if } z = 0 \\ \frac{z}{|z|}, & \text{else} \,. \end{cases} \tag{3.28}$$

Let the sign function extended to the complex numbers be defined by

$$\operatorname{sgn}(z) = \begin{cases} 0, & \text{if } z = 0 \\ \frac{z}{|z|}, & \text{else} \,. \end{cases} \tag{3.29}$$

Obviously, $\nabla_z |z| = \operatorname{sgn}(z)$ for $z \neq 0$. For the coefficients x_n of $\mathbf{x^{it}}$ which are zero, nothing should be changed since $|x_n|$ is already at the minimum value, i.e., the function g_2 replacing the gradient of $\lambda\|\mathbf{x}\|_1$ should be zero for those indices with zero coefficient, which is already implemented in the function. Therefore, $(g_2(\mathbf{x}))_n = \operatorname{sgn}(x_n)$ for all $n = 1, \ldots, N$.

A second refinement does not use only one μ for all coefficients, but introduces values μ_n which may deviate from μ. It relates to those elements which are not

zero, but a gradient step would 'overshoot' zero: x_n would be replaced by $x_n - \mu\lambda \text{sgn}(x_n) = (|x_n| - \mu\lambda)\,\text{sgn}(x_n)$. In the case $|x_n| < \mu\lambda$, such an overshooting would happen and it would be optimum to replace μ with $\mu_n = \frac{|x_n|}{\lambda}$ resulting in the lowest possible value zero.

The updated value $\tilde{\mathbf{x}} \to \hat{\mathbf{x}}$ in the second step results to

$$\hat{x}_n = \tilde{x}_n - \mu\left(g_2\left(\tilde{\mathbf{x}}\right)\right) \tag{3.30}$$

$$= \begin{cases} \tilde{x}_n - \mu\lambda \text{sgn}\left(\tilde{x}_n\right) = \left(|\tilde{x}_n| - \mu\lambda\right)\text{sgn}\left(x_n\right), & \text{if } |\tilde{x}_n| \geq \mu\lambda \\ 0 & \text{else .} \end{cases} \tag{3.31}$$

This is equivalent to the application of the soft thresholding operator with threshold $T = \mu\lambda$.

(3.31) presents the main update step behind the iterative soft thresholding algorithm (ISTA). Many variations of ISTA are available in literature, such as FISTA [BT09], Turbo-ISTA (TSTA) [P23], etc. The basic form of the ISTA is summarized in Algorithm 3.

Algorithm 3: Iterative Soft Thresholding Algorithm (ISTA)

Input: $\mathbf{y}$, $\boldsymbol{A}$, T, N_{it}
Initialization: $\hat{\mathbf{x}}^{[\mathbf{0}]} = 0$, $\mathbf{r}^{[\mathbf{0}]} = \mathbf{y}$, $\mu = \frac{1}{\lambda_{\max}(\boldsymbol{A}^H\boldsymbol{A})}$, $it = 1$
Result: $\hat{\mathbf{x}}^{[\mathbf{it}]}$, $\mathbf{r}^{[\mathbf{it}]}$
while *stopping criteria not met* **do**
  $\mathbf{x}^{[\mathbf{it}]} = S_T\left(\mathbf{x}^{[\mathbf{it-1}]} + \mu\boldsymbol{A}^H\mathbf{r}^{\mathbf{it-1}}\right)$;
  $\mathbf{r}^{[\mathbf{it}]} = \mathbf{y} - \boldsymbol{A}\mathbf{x}^{[\mathbf{it}]}$;
  if $\|\mathbf{r}^{[\mathbf{it}]}\|_2^2 \leq T$ or $it = N_{it}$ **then**
    stop thresholding
  else
    $it = it + 1$
  end
end

Chapter 4

Compressed Sensing for Radar

Till now, the working principle of a radar system and the theory of Compressed Sensing (CS) were discussed separately. This chapter serves as the link between the two areas and discusses compressed sensing applied to radars. An overview of the various applications of CS to radar can be found in [E10b], [HAJ+15]. Here, the focus is placed on radar scene reconstruction, under the logical assumption that the scene is sparse. The CS formulation discussed in Chapter 3 is applied to the radar scene detection problem mentioned in Chapter 2. Specifically, a radar-waveform dependant, structured CS formulation is presented, which later serves as the foundation for the main problem addressed in this thesis, i.e., CS for gapped-bands.

4.1 CS formulation for a general radar system

In Section 3.2, the importance of sparse representations in new-age signal processing was discussed. Now, the focus is placed on signal processing for radar systems in particular. As discussed in Chapter 2, traditional radar systems involve matched filtering of the received signal sampled at the Nyquist rate. This, coupled with the use of wide-band radar systems, leads to an enormous volume of data that requires massive computational power to be analyzed in real time. In contrast, the scene that is being detected is 'sparse', i.e., the number of objects of interest are quite small compared to the dimensions of the scene. Consequently, it makes sense to employ CS for the general radar scene reconstruction problem.

In addition to the sampling issue, the requirement of a better range resolution also favours the use of CS. A generic radar system can be viewed as a linear system, where the goal is to establish a map between the measurement samples and the scene reflectivities. Therefore, the reconstruction of the scene becomes a linear inverse problem. The additional demand for a high range resolution implies that the scene reconstruction must take place in a finer range grid, as compared to the coarser grid defined by the measurement samples. This gives rise to an ill-posed linear inverse problem or an under-determined system of linear equations. Based on the discussions in Chapter 3, this further strengthens the argument that the CS approach is a sensible way to tackle this problem.

In Chapter 2, the discussion focused on the properties of the commonly used radar waveforms. Now, based on the idea of a 'sparse scene', the radar signal model for scene reconstruction is discussed. Some super-script and sub-script notations are introduced to identify the stage of the signal in the processing workflow. The baseband representations are identified by the superscript b, while the sub-scripts Tx and Rx refer to the transmitted and received signals respectively. It is noted that the arbitrary signal $s(t)$ was considered in the baseband in Chapter 2 and here, it corresponds to s^b_{Tx}.

The sparse scene is modelled as a reflectivity distribution given by

$$h_{\text{Range}}(t) = \sum_{i=1}^{s} \rho_i \delta(t - \tau_i) \,, \tag{4.1}$$

where $\rho_i \in \mathbb{C}$ denotes the complex-valued reflectivities of each target, s denotes the number of targets (and consequently the sparsity in the CS problem) and the impulse responses $\delta(t - \tau_i)$ correspond to the peaks on the delay grid.

After convolution of the transmitted signal with the reflectivity distribution of the scene, the received signal s_{Rx} is given by

$$s_{\text{Rx}}(t) = (s_{\text{Tx}} * h_{\text{Range}})(t) = \sum_{i=1}^{s} \rho_i \mathcal{U}^{\tau_i}[s_{\text{Tx}}](t) \,, \tag{4.2}$$

where $\mathcal{U}^{\tau_i}$ is the time-shift operator, and s_{Tx} is the signal transmitted with the carrier frequency f_{Tx}. Down-mixing of s_{Rx} with the reference signal leaves only one additional phase term in the baseband signal due to f_{Tx}, i.e.,

$$s^b_{\text{Rx}}(t) = \sum_{i=1}^{s} \rho_i s^b_{\text{Tx}}(t - \tau_i) e^{-j2\pi f_{\text{Tx}} \tau_i} \,, \tag{4.3}$$

A more exhaustive discussion of this convolution-based interpretation of radar operation can be found in [R14, pp. 90 - 99]. The DFT block now performs a Fourier transform on the baseband signal and the resulting frequency-domain signal is given by

$$\mathcal{F}[s^b_{\text{Rx}}](f) = \sum_{i=1}^{s} \rho_i \mathcal{F}[s^b_{\text{Tx}}(t - \tau_i)](f) e^{-j2\pi(f + f_{\text{Tx}})\tau_i} \,. \tag{4.4}$$

Thus, (4.4) provides the expression for a general received signal in baseband in the frequency domain. It serves as the building block for the CS formulation and the expression for any waveform can be plugged into it.

Reviewing the general CS formulation given in (3.5) from a radar perspective, $\mathbf{y}$ is a vector of dimension m containing the available measurements, $\boldsymbol{A}$ is a sensing matrix of dimension $m \times N$, where $m \ll N$, weighted by the spectrum of the signal at hand, and $\mathbf{x}$ is an s-sparse reflectivity vector of dimension N, constructed from the reflectivities ρ_j of targets in the scene. Considering the effects of white Gaussian noise on the measurement vector $\mathbf{y}$ gives

$$\mathbf{y} = \boldsymbol{A}\mathbf{x} + \mathbf{n} \,. \tag{4.5}$$

Expanding (4.5) for frequency domain representations based on (4.4) gives

$$\begin{aligned} &\mathbf{y} = \boldsymbol{\phi}\boldsymbol{\psi}\mathbf{x} + \mathbf{n} \\ \implies &\mathbf{y} = \underbrace{\begin{bmatrix} s^b_{\text{Tx}}(f_1) & & \\ & \ddots & \\ & & s^b_{\text{Tx}}(f_m) \end{bmatrix}}_{\boldsymbol{\phi}} \\ &\underbrace{\begin{bmatrix} e^{-j2\pi(f_1+f_{\text{Tx}})\tau_1} & \dots & e^{-j2\pi(f_1+f_{\text{Tx}})\tau_N} \\ e^{-j2\pi(f_2+f_{\text{Tx}})\tau_1} & \dots & e^{-j2\pi(f_2+f_{\text{Tx}})\tau_N} \\ \vdots & \ddots & \vdots \\ e^{-j2\pi(f_m+f_{\text{Tx}})\tau_1} & \dots & e^{-j2\pi(f_m+f_{\text{Tx}})\tau_N} \end{bmatrix}}_{\boldsymbol{\psi}} \underbrace{\begin{bmatrix} \rho(\tau_1) \\ \rho(\tau_2) \\ \vdots \\ \rho(\tau_N) \end{bmatrix}}_{\mathbf{x}} + \mathbf{n} \,, \end{aligned} \tag{4.6}$$

where $\boldsymbol{\psi}$ represents a Fourier-like orthogonal sparsifying basis and $\boldsymbol{\phi}$ represents the synthesis matrix corresponding to a complete set of measurements as described in [CT06].

Following the structure of the radar waveforms discussed in Section 2.2, the next sections use (4.6) to formulate the problem based on different radar waveforms, namely the pulsed waveform, the chirp or LFM waveform, and a special case of the chirp, i.e., the FMCW.

4.1.1 CS Model for a Pulsed Radar

Following Section 2.2.1, the received signal vector from a single unit scatterer for a rectangular pulsed radar, after baseband conversion, in the time domain is

$$\begin{aligned} y(t) &= s^b_{\mathrm{Rx}}(t) \\ &= \rho s^b_{\mathrm{Tx}}(t-\tau)e^{-j2\pi f_{\mathrm{Tx}}\tau} . \end{aligned} \tag{4.7}$$

Considering the discrete version of $y(t)$

$$\begin{aligned} \mathbf{y} &= \sum_{i=1}^{s} \rho_i s^b_{\mathrm{Tx}}(t-\tau_i)e^{-j2\pi f_{\mathrm{Tx}}\tau_i} \\ &= \sum_{i=1}^{s} \rho_i \mathrm{rect}\left(\frac{t-\tau_i}{T_p}\right) e^{-j2\pi f_{\mathrm{Tx}}\tau_i} . \end{aligned} \tag{4.8}$$

A Fourier transform of (4.8) gives

$$y(f) = \sum_{i=1}^{s} \rho_i T_p \,\mathrm{sinc}\left(\pi f T_p\right) e^{-j2\pi(f+f_{\mathrm{Tx}})\tau_i} . \tag{4.9}$$

From (4.9), $s^b_{\mathrm{Tx}}(f) = T_p \,\mathrm{sinc}(\pi f T_p)$ can be used in (4.6), thereby giving the CS model for a pulsed radar. Expanding the more concise CS formulation from (4.5) gives,

$$\begin{bmatrix} y(f_1) \\ y(f_2) \\ \vdots \\ y(f_m) \end{bmatrix} = \begin{bmatrix} a(f_1,\tau_1) & \cdots & a(f_1,\tau_N) \\ a(f_2,\tau_1) & \cdots & a(f_2,\tau_N) \\ \vdots & \ddots & \vdots \\ a(f_m,\tau_1) & \cdots & a(f_m,\tau_N) \end{bmatrix} \begin{bmatrix} \rho(\tau_1) \\ \rho(\tau_2) \\ \vdots \\ \rho(\tau_N) \end{bmatrix} + \mathbf{n} , \tag{4.10}$$

where $a(f_i,\tau_j) = s^b_{\mathrm{Tx}}(f_i)e^{-j2\pi(f_i+f_{\mathrm{Tx}})\tau_j} = T_p \,\mathrm{sinc}(\pi f_i T_p)e^{-j2\pi(f_i+f_{\mathrm{Tx}})\tau_j}$.

4.1.2 CS Model for a Chirp Radar

Similarly, following Section 2.2.2, the received signal vector from a single target with a delay τ, in baseband, for an LFM radar or Chirp radar in the time domain is

$$\begin{aligned} y(t) &= s^b_{\mathrm{Rx}}(t) \\ &= \rho s^b_{\mathrm{Tx}}(t-\tau)e^{-j2\pi f_{\mathrm{Tx}}\tau} . \end{aligned} \tag{4.11}$$

Considering the discrete version,

$$\begin{aligned} \mathbf{y} &= \sum_{i=1}^{s} \rho_i s^b_{\mathrm{Tx}}(t-\tau_i)e^{-j2\pi f_{\mathrm{Tx}}\tau_i} \\ &= \sum_{i=1}^{s} \rho_i \mathrm{rect}\left(\frac{t-\tau_i}{T_p}\right) e^{j2\pi\frac{\alpha}{2}(t-\tau_i)^2} e^{-j2\pi f_{\mathrm{Tx}}\tau_i} . \end{aligned} \tag{4.12}$$

A Fourier transform of (4.12) gives

$$\mathbf{y} = \sum_{i=1}^{s} \rho_i s(f_i) e^{-j2\pi(f_i+f_{\text{Tx}})\tau_i} \,, \tag{4.13}$$

where $s(f_i)$ may be obtained used the Fresnel Integrals as in (2.18) or approximated by PSP as in (2.19). As before, expanding into the matrix-form CS model gives,

$$\begin{bmatrix} y(f_1) \\ y(f_2) \\ \vdots \\ y(f_m) \end{bmatrix} = \begin{bmatrix} a(f_1,\tau_1) & \cdots & a(f_1,\tau_N) \\ a(f_2,\tau_1) & \cdots & a(f_2,\tau_N) \\ \vdots & \ddots & \vdots \\ a(f_m,\tau_1) & \cdots & a(f_m,\tau_N) \end{bmatrix} \begin{bmatrix} \rho(\tau_1) \\ \rho(\tau_2) \\ \vdots \\ \rho(\tau_N) \end{bmatrix} + \mathbf{n} \,, \tag{4.14}$$

where $a(f_i, \tau_j) = s(f_i) e^{-j2\pi(f_i+f_{\text{Tx}})\tau_j}$.

Modeling a chirp radar with stretch processing : FMCW radar

Deramping or stretch processing is popularly used to exploit the high resolution capabilities of a chirp radar while at the same time reducing the sampling requirements. If a chirp radar with deramping is considered, the design of the sensing matrix will be different, i.e., it will constitute the beat frequency signals discussed in (2.29).

Based on (2.29), the received signal after deramping is

$$\begin{aligned} y(t) &= s_{\text{Rx}}(t) \; r^*(t) \\ &= \rho \; s_{\text{Rx}}(t-\tau) \; r^*(t) \\ &= \rho \; \text{rect}\left(\frac{t-\tau}{T_p}\right) e^{2\pi j\left(f_{\text{Tx}}(t_0-\tau)+\frac{\alpha}{2}\left(\tau^2-t_0^2\right)\right)} e^{2\pi j(\alpha t(t_0-\tau))} \,. \end{aligned} \tag{4.15}$$

Now, considering the discretized version,

$$\mathbf{y} = \sum_{i=1}^{s} \rho_i \text{rect}\left(\frac{t-\tau_i}{T_p}\right) e^{2\pi j\left(f_{\text{Tx}}(t_0-\tau_i)+\frac{\alpha}{2}\left(\tau_i^2-t_0^2\right)\right)} e^{2\pi j(\alpha t(t_0-\tau_i))} \,. \tag{4.16}$$

As discussed in Section 2.2.2, the last term $e^{2\pi j\alpha t(t_0-\tau_i)}$ has a constant frequency $\alpha(t_0-\tau_i)$, which corresponds to a specific range value. Therefore, (4.15) can be directly expanded to the matrix-form CS model giving,

$$\begin{bmatrix} y(t_1) \\ y(t_2) \\ \vdots \\ y(t_m) \end{bmatrix} = \begin{bmatrix} a(t_1,\tau_1) & \cdots & a(t_1,\tau_N) \\ a(t_2,\tau_1) & \cdots & a(t_2,\tau_N) \\ \vdots & \ddots & \vdots \\ a(t_m,\tau_1) & \cdots & a(t_m,\tau_N) \end{bmatrix} \begin{bmatrix} \rho(\tau_1) \\ \rho(\tau_2) \\ \vdots \\ \rho(\tau_N) \end{bmatrix} + \mathbf{n} \,, \tag{4.17}$$

where $a(t_i, \tau_j) = \text{rect}\left(\frac{t-\tau_i}{T_p}\right) e^{2\pi j\left(f_{\text{Tx}}(t_0-\tau_i)+\frac{\alpha}{2}\left(\tau_i^2-t_0^2\right)\right)} e^{2\pi j(\alpha t(t_0-\tau_i))}$.

Chapter 5

State of the Art (Methods) of missing data recovery

In Section 3.2, it was mentioned that a lack of natural resources may lead to 'forced compression at sensing'. The frequency spectrum has been known as one such 'limited natural resource' since the late 80's [J],[A94]. Concerns about spectrum allocation and congestion have existed for a very long time. However, a rapid increase in the number of users of the frequency spectrum in the recent years has once again brought this problem to light. Specifically, for radars and other remote sensing modalities, there has been an increasing demand for better range resolution, for various applications such as tracking and surveillance, environmental monitoring, and disaster management [GBC+13], [GCW+15]. Traditionally, such high range resolutions are possible only when a scene is detected using a wide-band radar. However, an exponential increase in spectrum congestion [LMP+20] has massively hindered the availability of such wide frequency bands. With the exponential increase of wireless communication systems and sensing devices each year, this problem continues to grow.

Due to such limitations on the frequency spectrum, sometimes only narrow-band radars in disjoint frequency bands are be available for target detection. From a different perspective, these narrow disjoint frequency bands can be viewed as a wide band with continuous gaps or blocks of missing data. Recasting the disjoint frequency band problem into such a 'gapped-band' problem naturally opens up a plethora of possibilities —- the massive body of work done on missing data estimation by various research communities may now be used to tackle this issue. This chapter aims to provides an overview of the literature on missing data estimation techniques that may be applied to the gapped frequency band problem.

5.0.1 Approaches from Spectral Estimation

The earliest work dealing with the estimation of missing data comes under the topic of 'spectral estimation'. In [SLL00], the popular amplitude and phase estimation approach (APES) was extended to 'gapped' amplitude and phase estimation (GAPES) under the assumption that the spectral content of the unavailable samples was the same as that of the available samples. The key idea behind the filter-bank approach from APES was to improve the SNIR significantly enough to counterbalance the reduction in the number of samples and obtain a better spectral estimate. GAPES used this spectral estimate to obtain the missing data samples. [SLL+09] provides another missing data estimation technique based on the Iterative Adaptive Approach (IAA). Here also, first an estimate of the spectrum was obtained from the available data, which was then used to estimate the missing data samples. In [SLL+09], the focus was placed on arbitrarily missing samples, and not on blocks or clusters of missing

data. However, both these techniques posed a very high computational complexity and were impractical for real-world applications. To combat this, [KRX+14] provided a fast implementation of IAA with applications to notched spectrum SAR, that could deal with a small cluster of missing data samples ($< 50\%$). [VXX+12] also considered missing data samples in arbitrary patterns and provided faster implementations of IAA and Sparse-learning via Iterative Minimization (SLIM) algorithms.

It was observed in [SLL+09] that the IAA is very well suited for applications where the estimate is sparse or atleast compressible. Such a scenario is a good fit for radar applications since the number of targets in a scene being detected is quite sparse in comparison to the dimensions of the scene. From this emerges the idea of leveraging the sparsity of the scene for better estimation, which naturally leads to the application of sparsity-aware signal processing techniques, a.k.a, CS, to the gapped-band problem.

Recent research under the umbrella of CS includes a large amount of work on obtaining good sparse estimates in the presence of missing data. Most of these methods work on solving an l_1-minimization problem, under the assumption that the sensing matrix satisfies the necessary coherence bounds. However, due to the unavailability of a wide, contiguous frequency band, such coherence bounds are not met, thus causing a failure of the conventional CS approaches. For instance, [YBZ20] discusses a CS method for reconstruction of a SAR image in the presence of periodically missing data along the azimuth. This problem is not as ill-posed as having a continuous block of missing data, and therefore, the discussed l_p minimization may fail when directly applied to the gapped-band problem. [GCB+18] discusses CS for ISAR image super-resolution in the presence of missing data in the frequency or slow time domain, and also provides an insightful performance comparison with traditional super-resolution methods. However, it is assumed that the under-complete Fourier matrices satisfy the RIP and provide sufficient non-coherence. The specific case of having blocks of missing data is also not considered. [WX22] presents a gridless CS approach based on atomic norm minimization to deal with tomographic SAR reconstruction in the presence of noise and limited data acquisitions. It highlights how moving to finer grids contradicts the traditional CS sensing matrix requirements and provides a new approach to tackle this issue.

A sub-branch of CS deals with the problem of missing data using 'group sparsity' [YL06], [HZ10]. However, due to the unique structure of the sensing matrix dictated by the radar system, the minimization used in such problems cannot be directly applied to the gapped-band problem. The problem of 'missing information' has also been addressed from the aspect of noisy sensor networks in a series of papers based on the mathematical model of Fusion Frames [ABL18], [CKL08]. The underlying assumption of distributed sparsity involving sub-division of the scene itself does not directly align with the band gap problem. Nevertheless, the concept of sub-division may be used to deal with the gaps in the frequency band, as described later in the thesis.

5.0.2 Deep Learning Approaches

Deep learning approaches to deal with general missing data estimation is vast. Here, the focus is placed on super-resolution and missing data estimation techniques for the specific case of radar signals and radar scene reconstruction. [YMS22] discusses how to obtain a high resolution SAR image from a medium resolution image using SRGAN-SSIM. It adapts an existing SRGAN network for SAR and includes a

SAR specific pre-processing step based on speckle noise suppression. [ZLQ19] proposes a lightweight deep neural network for SAR super-resolution inspired by SR-CNN [DLH+15] and aims to learn from residual features to reduce the number of model parameters and improve the speed. [WZD+18] proposes a GAN model for single image SAR super-resolution and experiments with a perceptual loss function consisting of content loss and adversarial loss. [ABB+23] motivates that getting a fine spatial resolution requires transmission of relatively large bandwidths, which is difficult because of hardware limitations and frequency allocation issues. The proposed DC2SCN network accounts for both real and imaginary components of the SAR data, thereby retaining the phase information. As mentioned by other papers, [ST23] also states the difficulties in operating a high-bandwidth system, and proposes deep-learning based multi-band signal fusion as an alternative solution. Specifically, it implements a complex valued CNN called the kR-Net that allows the model to learn features in both the wavenumber domain, or k-domain, and its spectral domain, the R-domain. The proposed CV-CNN architecture fuses multi-band data in the wavenumber domain to form an equivalent wide bandwidth signal and claims to be the first to leverage the relationship between the k-domain and R-domain. Apart from the model itself, the concept of multiband fusion relates closely to the JCS approach, where such multiple bands might occur due to spectral occupancy by communication signals. An interesting point in [ST23] is that it negates the sparsity-based approaches based on the fact that traditional CS requires random sampling to meet coherence requirements, which is not possible in practice. However, it does not delve into the structured CS formulation.

Deep learning has also been used in conjunction with concepts from CS to achieve better resolution. In some cases deep learning is used for constructing adaptive priors, while in others it is used for dictionary learning. [HLX+12] proposes a multi-dictionary (sparse-basis) learning based CS for SAR super-resolution and uses fundamental concepts from CS theory to ensure better reconstruction. Multi-dictionary training is based on the fact that the high and low resolution representations of a target patch map to the same (unique) sparse representation. Additionally, [HLX+12] also discusses the optimization of the observation matrix to reduce the coherence of the CS problem for lower reconstruction errors. [HZJ18] also uses a similar idea to train a global joint dictionary model for adaptive super-resolution of SAR images. [ASE23] proposes to use a generative model as a prior to the under-determined inverse problem pertaining to super-resolution of SAR images. MrSARP is trained in conjunction with a critic that scores multi resolution images jointly to decide if they are realistic images of a target at different resolutions. This deep generative model can be used to retrieve the high spatial resolution image from low resolution images of the same target. The generative model is interpreted as a learned projection function that can directly be used in CS algorithms such as Projected Gradient Descent optimization and it offers more flexibility on the commonly used sparsity prior.

A more interpretable deep learning approach based on unrolling or unfolding tradition CS algorithms into a deep neural network has gained a lot of attention in the recent years. [GL10] discussed this learned algorithm unrolling approach for different versions of the Iterative Soft-Thresholding Algorithm. [MLE20] provides a general overview of algorithm unrolling applied to image and signal processing and its role in making deep learning networks more interpretable. [LLM+19], [ZG18] discusses applications of algorithm unrolling in multi-spectral image fusion and super-resolution of optical images respectively.

One of the main problems with most deep-learning based methods is that they

rely heavily on existing high-resolution scenes for training, and suffer from the lack of reproducibility of results. However, explainable deep learning networks based on algorithm unrolling are paving the way for a combination of model-based and data-driven approaches, for better adaptive reconstruction. Again, it is observed, that the notion of sparsity and CS plays a very important role in many of the existing works, and are used as the foundation for many deep learning approaches.

5.0.3 Joint Communication and Sensing Approaches

The topic of joint communication and sensing (JCS) has become very popular in recent years and has reappeared in literature under different names, like Dual-Function Radar Communications (DFRC), Integrated Sensing and Communications (ISAC), Joint Communication and Radio Sensing (JCAS), Joint Radar (and) Communications (JRC), Joint Communications (and) Radar (JCR) etc.

[LZC+23] presents a systematic overview of the topic, separately highlighting the most important developments in radar and communication systems, from a signal processing point of view. Then, the components from both areas are used to formulate a signal model for ISAC. [LZC+23] states that in order to combat the intense competition for spectral resources, 'a variety of R&C systems have to cohabitate within multiple frequency bands, which, inevitably, incurs significant mutual interference between the two functionalities'. Focusing on the first level of such an integration, radar and communication systems need to share the frequency spectrum without interfering with one another. Traditionally this is done by allocating narrow bands to radars, with enough margin to ensure manageable interference levels. Following this approach, it is easy to recast the disjoint narrow bands into the gapped-band problem.

[TDJ+21] provides an overview of the recent developments in JCS with a focus on different system and network architectures and mentions how JCS may be considered a 'green' resource saving approach. Under the topic of 'radar-centric' signal processing approaches, [TDJ+21] discusses how OFDM and TDMA are controlled by the communication resource allocation, causing a sparse allocation of carriers in the frequency-time plane. It is mentioned that this has detrimental effects on the ambiguity function and CS maybe used to tackle such an issue. From the communications perspective, the need for data fusion in such a distributed sensing system is also mentioned.

[ZLM+21] gives another detailed overview of JCS from a signal processing point of view, particularly aiming to cover the gap in literature for receiver signal processing. As before, the discussion is divided into 2 parts: communication-centric design and radar-centric design. For the former, it is stated that since most communication systems are complicated in terms of resource usage, 'they may be discontinuous in one and more domains of space, frequency, and time'. This requires sensing algorithms that have the capacity to handle 'discontinuous and varying-interval samples'. This observation directly enforces the validity of the 'gapped-band' perspective. Furthermore, the advantages and disadvantages of using on-grid/off-grid CS to solve this issue are also discussed, with the main disadvantages being lack of sparsity and complexity of CS formulation for real data. For the radar centric design, the index modulation (IM) approach is given importance. IM in the spatial domain has been used in [MSH+21], while IM in the frequency domain again points to the gapped-band problem.

[WSL+21] also provides an interesting overview of JCS in terms of its role and challenges in the shift from 5G to 6G. The paper states that localization and sensing

need to be considered as an integral part of the communication network, and as not an add-on. It highlights the technical enablers as well as the challenges in closing this gap. Focusing on the discussion on joint waveforms and joint hardware as technical enablers, the authors mention that one of the most significant challenges for orthogonal frequency-division multiplexing (OFDM) radar will be inter-carrier interference (ICI), which destroys the orthogonality of sub-carriers and degrades the performance of conventional FFT-based algorithms. This, again, translates directly to the gapped band problem addressed in this thesis.

Apart from the overviews on JCS, both the sensing and communication communities have tried to add the other as an additional service, leading to communication-centric or radar-centric JCS approaches. For instance, [CME18] is a radar-centric approach to the problem, where the prototype of a 'Xampling' (compressive sampling) based cognitive radar is discussed. The radar works in narrow disjoint bands identified by a cognitive radio (CRo) comm receiver which senses the spectrum from sub-Nyquist samples and provides the radar with spectral occupancy information. In [BT23], a communication-centric design is discussed where a non-contiguous spectrum assignment of OFDM signals is used to cover more bandwidth to aid the sensing functionality. More communication-centric discussions are covered under the topic of 'Perceptive Mobile Networks' (PMNs), for example in [XSE+23], [ZRH+21].

It is evident that the concept of gaps in the spectrum keep appearing in literature in different forms, and many existing works try to leverage sparsity-aware methods such as CS to achieve improved sensing despite these gapped bands.

Chapter 6

Problem Formulation

6.1 Problem Statement

Based on the state of the art, the key takeaways and challenges can be outlined as follows:

- Continuous gaps in the frequency band occur as a result of hardware limitations, regulations for spectrum accessibility, spectrum congestion, joint communication and sensing, etc., resulting in a degradation of the radar range resolution.
- Traditionally, this problem was approached under the topic of spectral estimation but the computational load and fixed hyperparameters pose a practical challenge.
- Sparsity was used to improve the reconstruction results, recasting the gapped band problem into a CS problem. However, the incoherence requirements of existing CS methods are not satisfied in the presence of continuous gaps.
- Deep learning based methods use a data-driven approach to successfully address the issues with traditional spectral estimation. However, they pose challenges with reproducibility and in many cases require large amounts of high and low resolution image pairs.
- Recently, with the push towards 6G, more practical ways of dealing with these gaps, such as access schemes, CS based transceivers, etc., are proposed under the topic of 'Joint communication and Sensing'. However, from a signal processing perspective, the application of CS directly to the gapped-band problem still persists.

Supported by these arguments, the problem statement of this thesis is given as follows:

In order to overcome the degradation in radar range resolution caused by gaps in the frequency band, a scientific investigation of popular Compressed Sensing methods applied to gapped-band radars is necessary. An improved Compressed Sensing method that can provide better localization in the presence of such gaps in real radar data is needed.

6.2 The Gapped Band Problem

Mathematically, the aforementioned gap or gaps can be introduced into the CS formulation with the help of a projection matrix $\boldsymbol{P}$, such that

$$\begin{aligned}
\mathbf{y} &= \boldsymbol{A}\mathbf{x} + \mathbf{n} \\
&= \boldsymbol{P}\boldsymbol{\phi}\boldsymbol{\psi}x + \mathbf{n} \\
\implies \mathbf{y} &= \underbrace{\begin{bmatrix} I\ 0\ 0\ \cdots\ 0 \\ 0\ 0\ I\ \cdots\ 0 \\ & \ddots & \\ & & I \end{bmatrix}}_{\boldsymbol{P}} \underbrace{\begin{bmatrix} s^b_{\mathrm{Tx}}(f_1) & & \\ & \ddots & \\ & & s^b_{\mathrm{Tx}}(f_m) \end{bmatrix}}_{\boldsymbol{\phi}} \\
&\quad \times \underbrace{\begin{bmatrix} e^{-j2\pi(f_1+f_{\mathrm{Tx}})\tau_1} & \cdots & e^{-j2\pi(f_1+f_{\mathrm{Tx}})\tau_N} \\ e^{-j2\pi(f_2+f_{\mathrm{Tx}})\tau_1} & \cdots & e^{-j2\pi(f_2+f_{\mathrm{Tx}})\tau_N} \\ \vdots & \ddots & \vdots \\ e^{-j2\pi(f_m+f_{\mathrm{Tx}})\tau_1} & \cdots & e^{-j2\pi(f_m+f_{\mathrm{Tx}})\tau_N} \end{bmatrix}}_{\boldsymbol{\psi}} \underbrace{\begin{bmatrix} \rho(\tau_1) \\ \rho(\tau_2) \\ \vdots \\ \rho(\tau_N) \end{bmatrix}}_{\mathbf{x}} + \mathbf{n}\ .
\end{aligned} \tag{6.1}$$

$\boldsymbol{P}$ introduces the gap in $\boldsymbol{\phi}\boldsymbol{\psi}$, while the other terms remain as defined in (4.6). Now, following the structure of the CS models for different radar waveforms in 4.1, the gapped CS problem is defined for each case.

6.2.1 Gapped CS Model for a Pulsed Radar

Gapped Pulse

Considering the rectangular pulse discussed in (2.5), the corresponding gapped CS model is given by,

$$\begin{bmatrix} y(f_1) \\ y(f_2) \\ \vdots \\ y(f_m) \end{bmatrix} = \begin{bmatrix} I\ 0\ 0\ \cdots\ 0 \\ 0\ 0\ I\ \cdots\ 0 \\ & \ddots & \\ & & I \end{bmatrix} \begin{bmatrix} a(f_1,\tau_1) & \cdots & a(f_1,\tau_N) \\ a(f_2,\tau_1) & \cdots & a(f_2,\tau_N) \\ \vdots & \ddots & \vdots \\ a(f_m,\tau_1) & \cdots & a(f_m,\tau_N) \end{bmatrix} \begin{bmatrix} \rho(\tau_1) \\ \rho(\tau_2) \\ \vdots \\ \rho(\tau_N) \end{bmatrix} + \mathbf{n}\ , \tag{6.2}$$

where $a(f_i,\tau_j) = s^b_{\mathrm{Tx}}(f_i)e^{-j2\pi(f_i+f_{\mathrm{Tx}})\tau_j} = T_p\,\mathrm{sinc}(\pi f_i T_p)e^{-j2\pi(f_i+f_{\mathrm{Tx}})\tau_j}$.

6.2.2 Gapped CS Model for a Chirp Radar

Gapped chirp

In the case of a gapped chirp, the individual chirps are present in separate, non-adjacent frequency bands and exist in different time intervals. Therefore, the gap exists both in time and in frequency. The gapped chirp in time domain is given by

$$y^b_{\mathrm{Tx}}(t) = e^{j\pi\alpha t^2} \sum_{i=1}^{l} \mathrm{rect}\left(\frac{t-\tau_i}{T_i}\right)\ , \tag{6.3}$$

where the rect$(\cdot)$ function represents parts of the available signal, obtained at different time windows and l represents the total number of individual chirps.

The Fourier transform of the gapped chirp is given by

$$\begin{aligned}\mathcal{F}[y^b_{\text{Tx}}](f) &= \int_{-\infty}^{+\infty} e^{j\pi\alpha t^2}\left(\sum_{i=1}^{l}\frac{1}{\sqrt{T_i}}\text{rect}\left(\frac{t-\tau_i}{T_i}\right)\right)e^{-j2\pi ft}dt \\ &= \sum_{i=1}^{l}\frac{1}{\sqrt{T_i}}\int_{\frac{-T_i}{2}+\tau_i}^{\frac{T_i}{2}+\tau_i} e^{j\pi(\alpha t^2-2ft)}dt \\ &= \sum_{i=1}^{l}\frac{1}{\sqrt{T_i}}\int_{\frac{-T_i}{2}}^{\frac{T_i}{2}} e^{j\pi(\alpha(t_i+\tau_i)^2-2(f(t_i+\tau_i))}dt_i\ . \end{aligned} \tag{6.4}$$

The second equation of (6.4) involves a change of the integration variable from $\frac{-T_i}{2}+\tau_i$ to $\frac{-T_i}{2}$ in order to align the given integral with the standard Fourier Transform of a chirp signal as given by (2.17). This represents a re-centering of the sub-chirps around the zero of the time axis, which in turn yields the coefficient $e^{j2\pi\left(\frac{\alpha}{2}\tau_i^2-f\tau_i\right)}$. The final formulation of the Fourier Transform of the gapped chirp signal of (6.3) is

$$\begin{aligned}\mathcal{F}[y^b_{\text{Tx}}](f) = \sum_{i=1}^{l}\frac{1}{\sqrt{T_i}}\Bigg(&e^{j2\pi\left(\frac{\alpha}{2}\tau_i^2-f\tau_i\right)} \\ &\times\int_{\frac{-T_i}{2}}^{\frac{T_i}{2}} e^{j\pi\left(\alpha t^2-2(f-\alpha\tau_i)t\right)}dt\Bigg)\ . \end{aligned} \tag{6.5}$$

Comparing with (2.17), the term $2ft$ in the integral is replaced by the term $2(f-\alpha\tau_i)t$. This frequency-shift term represents the center frequency of each sub-chirp. Applying Fresnel integrals defined in (2.18) to (6.5) yields the final description of the gapped chirp in frequency domain as

$$\begin{aligned}\mathcal{F}[y^b_{\text{Tx}}](f) = \sum_{i=1}^{l}\frac{1}{\sqrt{T_i}}\Bigg(&e^{j2\pi\left(\frac{\alpha}{2}\tau_i^2-f\tau_i\right)} \\ &\times\sqrt{\frac{1}{2\alpha}}e^{-j\pi\frac{(f-\alpha\tau_i)^2}{\alpha}}\left[Z\left(u_2\right)-Z\left(u_1\right)\right]\Bigg)\ . \end{aligned} \tag{6.6}$$

Similarly, applying the PSP, as given in (2.19), to (6.5) gives (derivation in Appendix. A.1)

$$\begin{aligned}\mathcal{F}[y^b_{\text{Tx}}](f) = \sum_{i=1}^{l}\frac{1}{\sqrt{T_i}}\Bigg(&e^{j2\pi\left(\frac{\alpha}{2}\tau_i^2-f\tau_i\right)} \\ &\times\sqrt{\frac{-1}{\alpha}}e^{\frac{-j\pi}{4}}e^{j2\pi\left(\frac{-f^2}{2\alpha}+f\tau_i+\frac{-\alpha\tau_i^2}{2}\right)} \\ &\times\text{rect}\left(\frac{f-\alpha\tau_i}{\alpha T_i}\right)\Bigg)\ . \end{aligned} \tag{6.7}$$

In order to validate the frequency domain representation obtained using Fresnel integrals, it is compared to a direct FFT of the gapped-signal. Fig. 6.1 shows that both the methods give identical amplitude and phase spectra in the relevant frequency band.

Fig. 6.3 shows the spectra of 2 LFM signals. The first spectrum (in blue) is based on a signal that is gapped in both time and frequency, as described by (6.5). For the second spectrum (in red), the signal has a gap in frequency but the gap in time is

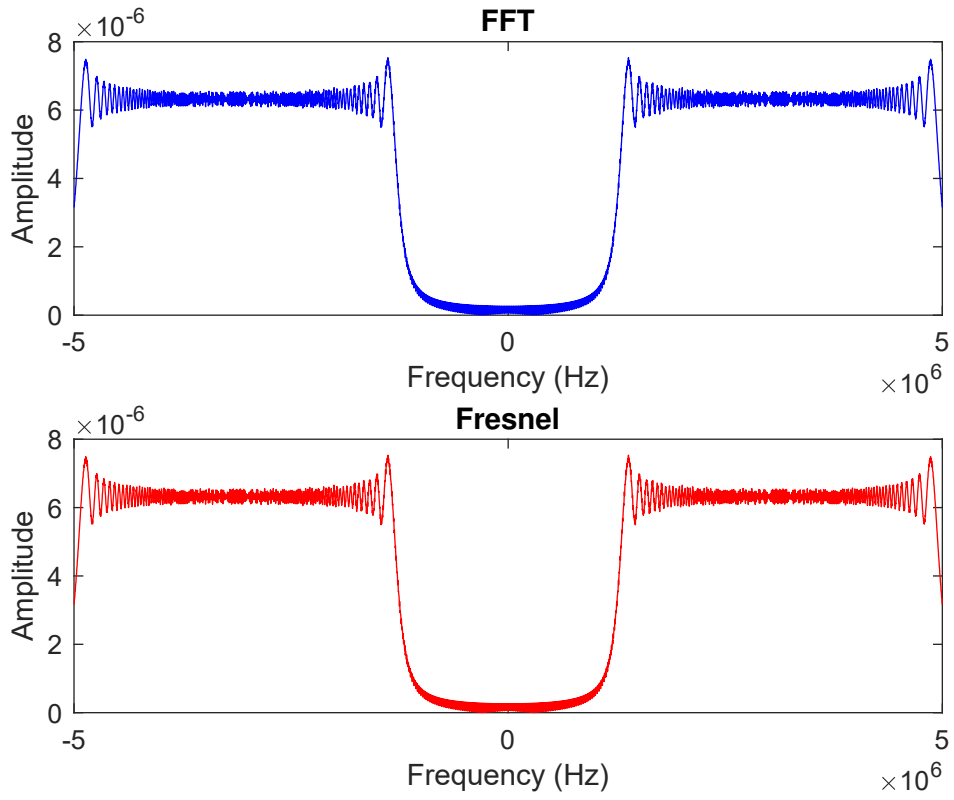

(A) Amplitude Spectra

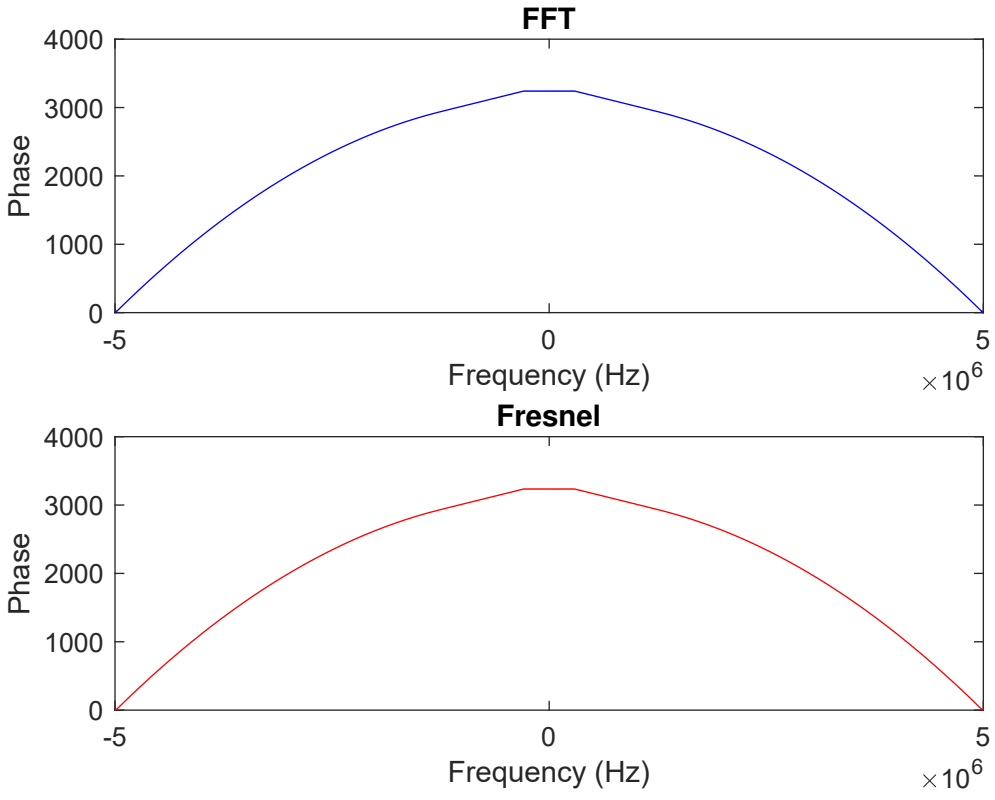

(B) Phase Spectra

FIGURE 6.1: Spectra of gapped chirp signals using FFT and Fresnel Integrals [GBH+22].

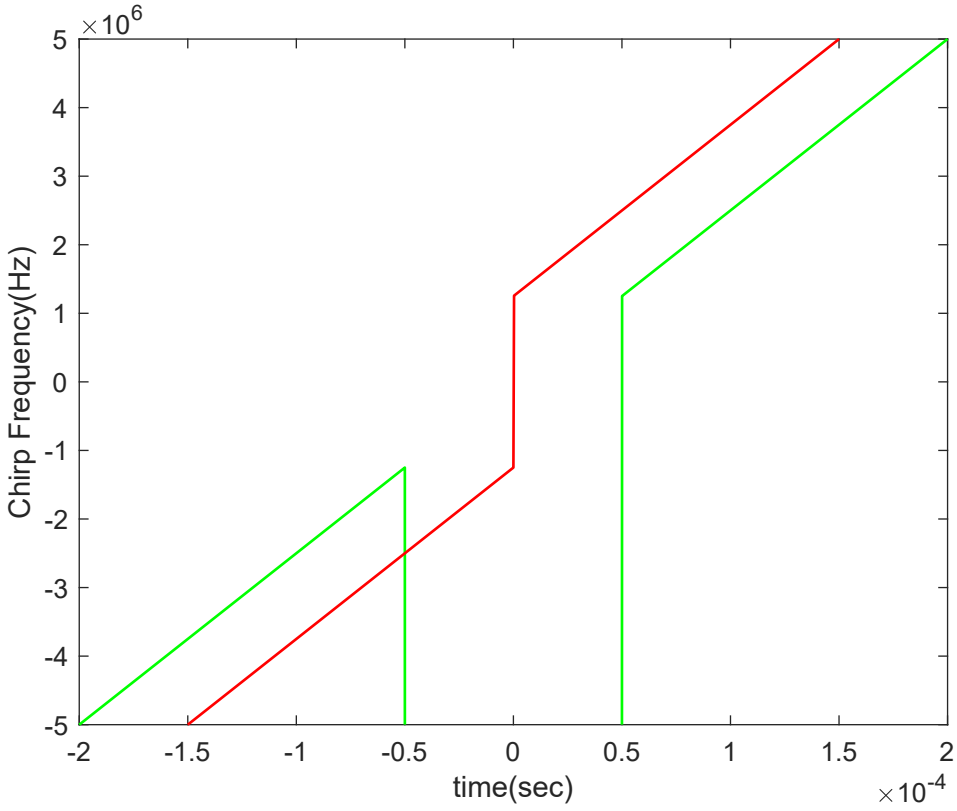

FIGURE 6.2: Time-Frequency Plot with gap in both time and frequency (green) and gap in frequency, jump in time (red) [GBH+22].

removed. This is done by time shifting each individual chirp from (6.3), such that they are continuous in time. As a result, the frequency jumps at the end of each sub-chirp to the initial frequency of the next sub-chirp. This time-continuous spectrum can be derived by incorporating the time-shifts into the leading coefficients of (6.6) such that

$$\begin{aligned}\mathcal{F}[y^b_{\text{Tx}}](f) = e^{-j2\pi t_c}\sum_{i=1}^{l}\Bigg(& e^{-j2\pi f\tau_i^d}e^{j2\pi\left(\frac{\alpha}{2}\tau_i^2 - f\tau_i\right)} \\ &\times\sqrt{\frac{T_i}{2\beta}}e^{-j\pi\frac{(f-\alpha\tau_i)^2}{\alpha}}\left[Z\left(u_2\right) - Z\left(u_1\right)\right]\Bigg)\end{aligned} \tag{6.8}$$

where $\tau_1^d = 0$, $\tau_2^d = \left(\tau_1 + \frac{T_1}{2}\right) + \left(\frac{T_2}{2} - \tau_2\right)$ and the remaining $\tau_i^d, i = 3, \cdots, l$ are given by

$$\tau_i^d = \left(\tau_1 + \frac{T_1}{2}\right) + \sum_{p=2}^{i-1} T_p + \left(\frac{T_i}{2} - \tau_i\right) .$$

The phase term $e^{-j2\pi t_c}$ represents a shift in time, t_c, that re-centers the whole time-continuous chirp around the zero of the time-axis. Note that the first sub-chirp is the reference for the time shifting of the other sub-chirps and the τ_i^ds are all negative since the shift is always to the left. The time periods (T_i) and the original

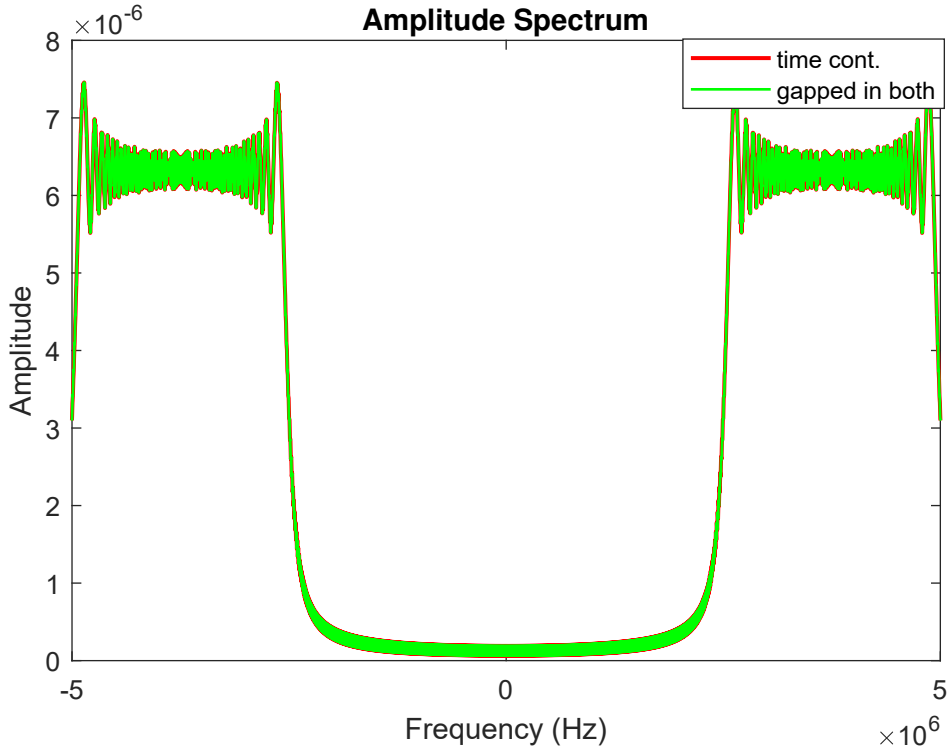

(A) Amplitude Spectrum

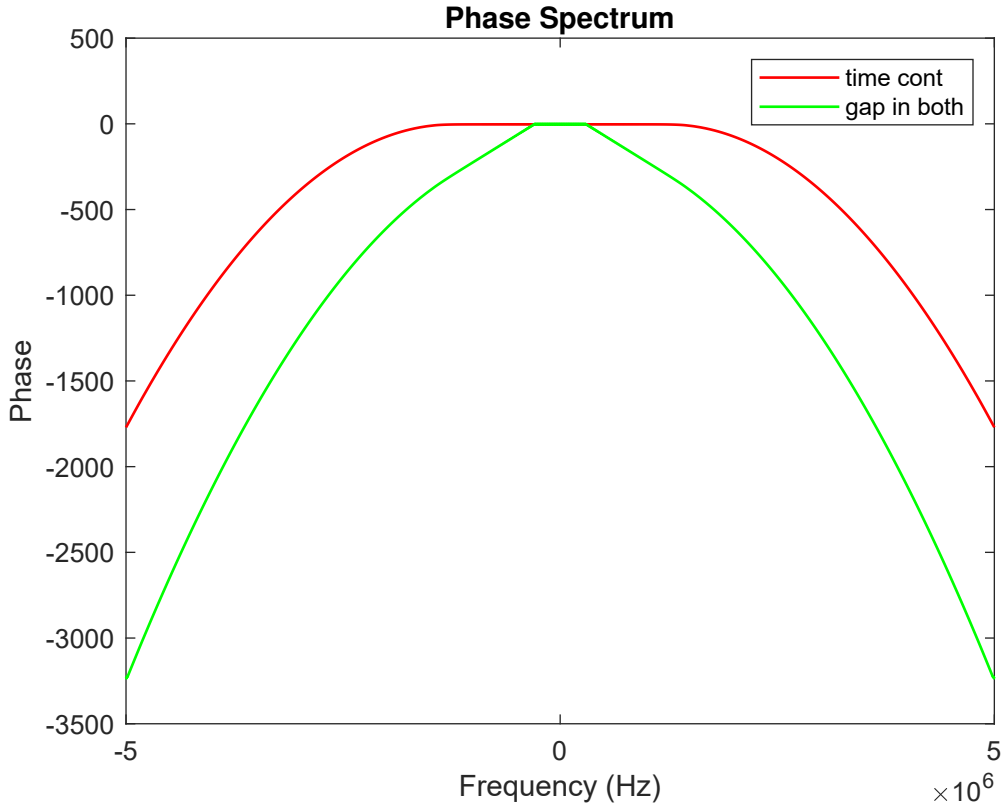

(B) Phase Spectrum

FIGURE 6.3: Spectra of gapped chirp signals with gap in time and frequency (green) and gap in frequency and jump in time (red), i.e., the first and second part of the signal are contiguous [GBH+22].

time shifts (τ_i) of the center of each chirp from zero allow us to determine the additional shifts needed to make the entire signal time-continuous. Finally, this time-continuous signal is re-centered around the zero of the time axis, as shown in Fig. 6.3. The top figure in Fig. 6.3 shows the change in frequency over time for both the time-continuous and gapped-time chirps. The middle figure shows the amplitude spectra for both chirps. Since they have the exact same energy at identical frequency sub-bands, there is a complete overlap of the spectra. The bottom figure shows the phase spectra from both chirps. The difference between the spectra is due to the extra phase term introduced by the time shift given in (6.8).

Gapped CS model

Following 4.14, the gapped CS model for a chirp radar is

$$\begin{bmatrix} y(f_1) \\ y(f_2) \\ \vdots \\ y(f_m) \end{bmatrix} = \begin{bmatrix} I & 0 & 0 & \cdots & 0 \\ 0 & 0 & I & \cdots & 0 \\ & & & \ddots & \\ & & & & I \end{bmatrix} \begin{bmatrix} a(f_1,\tau_1) & \cdots & a(f_1,\tau_N) \\ a(f_2,\tau_1) & \cdots & a(f_2,\tau_N) \\ \vdots & \ddots & \vdots \\ a(f_m,\tau_1) & \cdots & a(f_m,\tau_N) \end{bmatrix} \begin{bmatrix} \rho(\tau_1) \\ \rho(\tau_2) \\ \vdots \\ \rho(\tau_N) \end{bmatrix} + \mathbf{n}\,, \tag{6.9}$$

where $a(f_i,\tau_j) = s(f_i)e^{-j2\pi(f_i+f_{\text{Tx}})\tau_j}$.

Modeling gaps in a chirp radar with stretch processing : FMCW radar

The working principle of an FMCW Radar was described in Chapter 2. In this section, the gapped-signal structure for FMCW radars is explored and the corresponding sensing matrix construction is discussed.

The frequency-domain sensing matrix can be used directly in a CS problem, as seen in (4.14). However, there are certain disadvantages of using this version of the sensing matrix in practice. The conversion of the received chirp signals from the time domain to frequency domain causes a significant computational load, specially when there are a large number of samples. Additionally, the construction of the frequency-domain sensing matrix is based on a general radar signal and does not take into account the advantages of certain specific system designs.

FMCW radars are a special implementation of radar systems where the received LFM signals undergo 'stretch processing' or 'de-ramp processing' to give intermediate frequency signals or 'beat frequency' signals, as described in Chapter 2. If an FMCW radar based system design is considered, the sensing matrix becomes a dictionary of beat frequency signals, as demonstrated in (4.17). Here, this model is extended to a gapped model. Instead of using the projection matrix $\boldsymbol{P}$ to mathematically introduce a gap, a more practical approach is discussed.

The FMCW signal model allows an indirect definition of the band gap by attributing the sub-chirps to individual FMCW radar systems, creating a group of independent but spatially co-located systems in the process. This idea is shown in Fig. 6.4, and is closer to how a gap would occur in a practical system of radars. The conventional matched filter is replaced by a CS block, which performs the range processing using the beat frequency signals from each radar system. This gapped FMCW signal model is elaborated in the following sections.

FMCW signal model

Consider a reference LFM signal

$$y(t) = e^{j(2\pi f_{Tx}t+\pi\alpha t^2)}\text{rect}\left(\frac{t}{T_p}\right)\,, \tag{6.10}$$

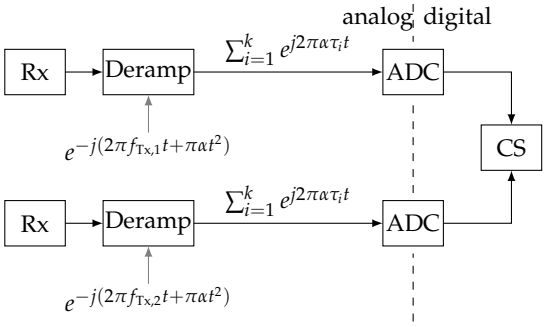

FIGURE 6.4: Schematic depiction of the system structure based on multiple LFM systems with a joint evaluation of the beat frequency signals.

where f_{Tx} is the transmit frequency (or center frequency) of the signal, α is the slope, and T_p is the pulse duration. Stretch processing of this reference LFM signal gives the reference beat frequency signal (derivation in A.2)

$$y_{\mathrm{IF}}^{\tau_j}(t) = e^{j\left(2\pi f_{\mathrm{Tx}}\left(t_0-\tau_j\right)+\pi\alpha\left(\tau_j^2-t_0^2\right)-2\pi\alpha t\left(\tau_j-t_0\right)\right)}\mathrm{rect}\left(\frac{t-\tau_j}{T_p}\right)\mathrm{rect}\left(\frac{t-t_0}{T_p}\right), \tag{6.11}$$

where τ_j is the time delay of the signal backscattered from a target at the j^{th} index of the delay grid.

In practice, multiple sub-LFM signals are received in the CS block, each corresponding to an FMCW radar. Theoretically, this can be expressed by windowing the reference LFM signal into multiple sub-LFM signals, similar to (6.3). Each sub-LFM signal is defined by

$$y(t) = e^{j(2\pi f_{Tx} t+\pi\alpha t^2)}\mathrm{rect}\left(\frac{t-\tau_i}{T_i}\right), \tag{6.12}$$

where $i = 1,\ldots,M$, and M corresponds to the total number of FMCW radar systems. Since each individual system operates within its own time basis, the sub-LFM signals in the global time basis t are to be transferred into the individual times bases, $\tilde{t}_i$, by defining time-shifts τ_i, i.e., $\tilde{t}_i = t-\tau_i$. Using this variable substitution in (6.12), the sub-LFM signals are described as

$$\begin{aligned}\tilde{y}_i\left(\tilde{t}_i\right) &= e^{j(2\pi f_{Tx}(\tilde{t}_i+\tau_i)+\pi\alpha(\tilde{t}_i+\tau_i)^2)}\mathrm{rect}\left(\frac{\tilde{t}_i}{T_i}\right)\\ &= e^{j\left(2\pi(f_{\mathrm{Tx}}-\alpha\tau_i)\tilde{t}_i+\pi\alpha\tilde{t}_i^2-2\pi f_{Tx}\tau_i+\pi\alpha\tau_i^2\right)}\mathrm{rect}\left(\frac{\tilde{t}_i}{T_i}\right).\end{aligned} \tag{6.13}$$

The beat frequency signals corresponding to a sub-LFM signal from the i^{th} FMCW radar for a target with a delay of τ_j can be expressed as

$$\tilde{y}_{\mathrm{IF,i}}^{\tau_j}\left(\tilde{t}_i\right) = e^{j\left(2\pi(f_{\mathrm{Tx}}-\alpha\tau_i)\left(t_0-\tau_j\right)+\pi\alpha\left(\tau_j^2-t_0^2\right)-2\pi\alpha\tilde{t}_i\left(\tau_j-t_0\right)\right)}\mathrm{rect}\left(\frac{\tilde{t}_i-\tau_j}{T_i}\right)\mathrm{rect}\left(\frac{\tilde{t}_i-t_0}{T_i}\right). \tag{6.14}$$

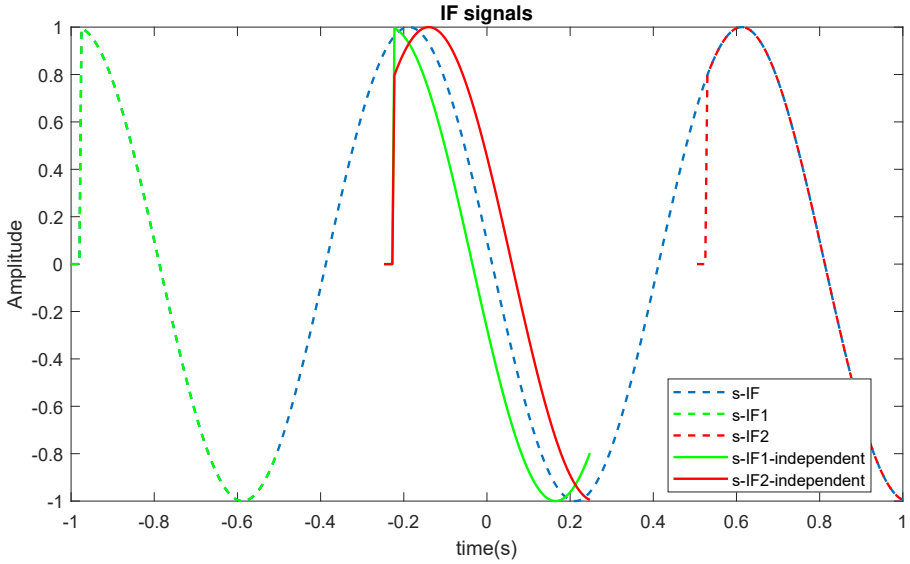

FIGURE 6.5: Phase alignment of the sub-LFM signals with the reference signal.

A comparison of the sub-LFM signal equations and the reference signal equations shows that there are additional terms in the sub-LFM signals, that dictate important time-frequency relationships in the signal model. This is elaborated as follows.

An examination of (6.10) and (6.13) shows that $-2\pi f_{\mathrm{Tx}}\tau_i + \pi\alpha\tau_i^2$ in (6.13) is an additional term, which serves the purpose of aligning the sub-LFM signals to the reference LFM signal in phase. This is demonstrated by the beat frequency (or IF) signals shown in Fig. 6.5. The beat frequency signal corresponding to the reference LFM signal (s-IF) is indicated by the blue line. The solid lines (s-IF1-independent, s-IF2-independent) indicate the beat frequency signals corresponding to 2 sub-LFM signals, centered at 0. The dotted lines (s-IF1, s-IF2) indicate the same sub-LFM beat frequency signals, but now with a certain phase shift. It is seen that this phase shift is different for the 2 signals, and it exactly aligns the sub-LFM beat frequency signals to the reference LFM beat frequency signal. This phase shift is determined by the term $-2\pi f_{\mathrm{Tx}}\tau_i + \pi\alpha\tau_i^2$. This term appears only in the sub-LFM expression. It does not influence the eventual sub-LFM beat frequency signal $\tilde{y}_{\mathrm{IF,i}}^{\tau_j}$.

A comparison of the structure of equations (6.11) and (6.14) shows that a frequency shift term $-\alpha\tau_i$ is added to the transmit frequency of the reference signal in (6.14). $(f_{\mathrm{Tx}} - \alpha\tau_i)$ defines the center frequencies $f_{\mathrm{Tx},i}$ of the sub-LFM signals. τ_i also happens to be the time shift applied during the windowing of the reference signal and transfer to the local time basis of each radar system. It is evident that this time shift directly affects the frequency shift applied to the reference center frequency, giving the sub-LFM center frequencies. Therefore, the temporal shift or temporal gap between the subchirps from the different FMCW systems corresponds to the gap in their frequency bands. It is sufficient to know the respective center frequencies of a series of LFM signals in order to establish the individual relationships between then using the temporal gap (for a given slope α).

In this context, the temporal relation between the reference beat signal and sub-LFM beat signals is directly related to the temporal/frequency relation between the reference LFM signal and the sub-LFM signals. That is, (6.14) can also be obtained

by applying the same sequence of rect(.) signals to $y_{\mathrm{IF}}^{\tau_j}(t)$ [1] and performing the substitution $\tilde{t}_i = t - \tau_i$ as before. The term $-\alpha\tau_i\left(t_0 - \tau_j\right)$ is the initial phase shift due to temporal shift of a sub-LFM signal with respect to the reference LFM signal, which encompasses the center-frequency shift for the sub-LFM signals. This re-establishes the fact that the gap in the frequency spectrum is reflected as a temporal gap.

Construction of sensing matrix in time domain

For the construction of the sensing matrix, it is necessary to consider the maximal delay, since this defines the rect window for all beat signals of the individual systems[2]. The sub-signals $\tilde{y}_{\mathrm{IF,i}}^{\tau_j}(\tilde{t}_i)$ of the multiple individual systems i and individual beat frequencies j can be arranged to yield

$$\begin{bmatrix} \tilde{y}_{\mathrm{IF},1} \\ \tilde{y}_{\mathrm{IF},2} \\ \vdots \\ \tilde{y}_{\mathrm{IF,M}} \end{bmatrix} = \begin{bmatrix} \tilde{y}_{\mathrm{IF},1}^{\tau_1} & \tilde{y}_{\mathrm{IF},1}^{\tau_2} & \cdots & \tilde{y}_{\mathrm{IF},1}^{\tau_N} \\ \tilde{y}_{\mathrm{IF},2}^{\tau_1} & \tilde{y}_{\mathrm{IF},2}^{\tau_2} & \cdots & \tilde{y}_{\mathrm{IF},2}^{\tau_N} \\ \vdots & \vdots & \ddots & \vdots \\ \tilde{y}_{\mathrm{IF,M}}^{\tau_1} & \tilde{y}_{\mathrm{IF,M}}^{\tau_2} & \cdots & \tilde{y}_{\mathrm{IF,M}}^{\tau_N} \end{bmatrix} \begin{bmatrix} x(\tau_1) \\ x(\tau_2) \\ \vdots \\ x(\tau_N) \end{bmatrix} + \mathbf{n}\,, \tag{6.15}$$

where the $\tau_1..\tau_N$ are assumed to be equidistantly separated, $\tau_N = \tau_{j,\max}$, and M is the number of sub-LFM signals or individual radar systems. (6.15) follows the same CS problem structure as described in 4.17. However, the matrix of (6.15) now follows a block (row) form. That is, each block row consists of rows of time-domain measurements from individual radar systems. The range grid spacing, i.e, the spacing between the τ_j, can be arbitrarily set so as to meet the required resolution. The subdivision along the block rows follows from the available frequency bands where the radars operate.

Synchronization : This section takes into account the effect of time and frequency synchronization errors [TLZ09] for the beat frequency signal defined in (6.13). For a system of FMCW radars as discussed in this Section, it is necessary that the individual systems are synchronized so that their center frequencies, or rather the band gaps, agree with the assumptions that the sensing matrix is based upon. Or vice-versa, the actual individual center frequencies are known and the sensing matrix is constructed accordingly. Three main synchronization error terms are considered—error in transmitter frequency (f_e^{Tx}), error in receiver frequency (f_e^{Rx}), and error in time, since the receiver does not know exactly when the pulse was sent by the transmitter ($\tilde{t_R}$). Based on these errors, the modified time and frequencies are expressed as

$$\tilde{f_{\mathrm{Tx}}} = f_{\mathrm{Tx}} + f_e^{\mathrm{Tx}}, \quad \tilde{f_{\mathrm{Rx}}} = f_{\mathrm{Tx}} + f_e^{\mathrm{Rx}}, \quad \tilde{t}_R = \tilde{t}_i - t_e\,,$$

where $\tilde{f_{\mathrm{Tx}}}$ and $\tilde{f_{\mathrm{Rx}}}$ are the modified transmitter and receiver frequencies, and $\tilde{t}_R$ is the modified time basis for the individual sub-LFM signals. If the system is co-located, $\tilde{f_{\mathrm{Tx}}} = \tilde{f_{\mathrm{Rx}}}$ or $f_e^{\mathrm{Tx}} = f_e^{\mathrm{Rx}}$.

[1] This has to be done while taking into account that the windowing rect $\left(\frac{t-\tau_j}{T_p}\right)$ rect $\left(\frac{t-t_0}{T_p}\right)$ needs to be done for each rect(.) of this sequence individually.

[2] Or the design of the respective systems, which might differ from this straight-forward mathematical description

The sub-LFM signal remains as defined by (6.12). However, the down-mixing is affected due to the synchronization errors and (6.13) is replaced by

$$\begin{aligned} \tilde{y}^{\tau_j}_{\mathrm{IF,i,sync}}\left(\tilde{t}_i\right) &= \left(\mathcal{U}^{t_e}[y_{\mathrm{Rx}}] * \overline{\mathcal{U}^{\tau_j}[y_{\mathrm{Tx}}]}\right)\left(\tilde{t}_i\right) \\ &= \tilde{y}^{\tau_j}_{\mathrm{IF,i}}\left(\tilde{t}_i\right) e^{2\pi j(a-b+c)} \,, \end{aligned} \tag{6.16}$$

where $\mathcal{U}^{\tau_i}$ is the time-shift operator, $a = (f_e^{\mathrm{Rx}} - f_e^{\mathrm{Tx}})(\tilde{t}_i - \tau_i)$, $b = (\tilde{f_{\mathrm{Rx}}}$ and $c = \frac{k}{2}(t_e^2 - 2\tilde{t}_i t_e)$. Therefore, the synchronization errors appear as errors in phase. The term $e^{2\pi j((f_e^{\mathrm{Rx}} - f_e^{\mathrm{Tx}})(\tilde{t}_i - \tau_i))}$ describes the error arising from the mismatch of the transmitter and receiver frequencies. This term will disappear if a co-located system is considered. $e^{-2\pi j(f_{\mathrm{Rx}} + k\tau_i)t_e}$ signifies an additional shift in the center frequency of the individual sub-LFM signals. The term $e^{2\pi\frac{k}{2}(t_e^2 - 2\tilde{t}_i t_e))}$ signifies an error in the delay from a target, which will lead to an error in the detected range. Since a synchronization in the order of nano-seconds is required for the problem at hand, the synchronization errors can be overcome by using the same oscillator for the individual, co-located radar systems.

Chapter 7

Compressed Sensing Methods to tackle the gapped-band problem

The previous chapter concentrated on the theoretical aspect of the formulation of a structured sensing matrix for a gapped-band scenario. This chapter introduces 2 algorithms based on CS for target detection in the presence of such a gap. The first algorithm is a subdivision-based CS approach which uses the previously discussed structured sensing matrices. The second algorithm is based on the idea of approximated observation, where the sensing matrix is replaced by a SAR processor block. For both algorithms, simulation results and results obtained on real radar data are discussed.

7.1 A CS based Subdivision-Fusion Algorithm

As discussed previously, a signal with a spectral gap can be cast into an underdetermined system of linear equations, making this a problem that may be solved using CS techniques. However, such a continuous gap limits the feasibility of the CS estimation. In this chapter, a 'Subdivision-Fusion' (SF) algorithm is explored to deal with this problem. The core idea is inspired by the work on fusion frames in [CKL08; ABL18]. A direct application of [CKL08; ABL18] to the current problem would result in a non-coherent estimation. Nevertheless, the concept of subdividing an ill-posed CS problem, followed by fusion of the results, can be utilized. The main idea of the algorithm is briefly outlined as follows. A finely-spaced range grid in the scene domain leads to a high coherence of the gapped sensing matrix and as result, the reconstruction of the sparse scene vector by CS algorithms becomes unstable. Greater robustness can be achieved if the overall problem is broken down into multiple sub-problems, each with a coarser range grid, spanning different portions of the fine range grid (subdivision). As a result, each sub-problem now corresponds to a sensing matrix with a smaller number of columns that are further apart in range, in comparison with the columns of the original sensing matrix. This leads to a reduction in the respective coherences. A now more robust CS reconstruction is applied to each sub-problem, whereby some of the contributions from positions that do not lie on the coarse grid are of course lost. But in the following step (fusion), the results are merged and lead to an improved reconstruction of the overall vector.

The algorithm is described in detail in 7.1.2. In 7.1.3, the differences between the proposed method and some of the existing research in the same area are pointed out. This is followed by the simulation results and results on real radar data.

TABLE 7.1: Band gap vs. coherence of corresponding sensing matrix (the aspect of multiple gaps will be considered in section 7.1.4)

	Band Gap as Fraction of Whole Band			
Whole Band (W)	$0.1W$	$0.5W$	$0.7W$	$0.9W$
1 MHz	0.14	0.65	0.85	0.98
10 MHz	0.16	0.62	0.86	0.98
100 MHz	0.15	0.65	0.85	0.98
1 GHz	0.15	0.67	0.87	0.98

7.1.1 Preliminaries

Effects of band bap on coherence of the CS sensing matrix

Be it in the frequency domain or time domain, a gap essentially subdivides the sensing matrix into blocks. In order to get a good sparse estimate from the CS formulation, the columns of the sensing matrix should be as dissimilar as possible. In other words, their inner product should be very small. Now, due to the band gap, there exists a gap along the rows, and a part of the frequency content responsible for making adjacent columns dissimilar is lost. As a result, the degree of similarity of adjacent columns—measured by their inner product, or more specifically, their mutual coherence—increases. The larger the width of the gap, the more is the information lost and the closer this inner product becomes to one (considering normalized columns). The resulting increased coherence of the sensing matrix leads to an ill-posed CS problem for which conventional CS reconstruction methods fail to provide a correct estimate. Table. 7.1 shows that given a frequency band of a certain width, the coherence of the sensing matrix increases with increase in the width of the gap. It also demonstrates that the coherence values are not affected by the width of the whole band. The coherence solely depends on the ratio of width of the gap to that of the whole band.

In order to tie this argument to the working of specific CS algorithms, consider the popular greedy l_1-minimization method known as Orthogonal Matching Pursuit (OMP) and a variation of the basis pursuit (BP) algorithm called Least Absolute Shrinkage and Selection Operator (LASSO). OMP consists of two main steps: support update and residual calculation [BZ21]. If the coherence of $\boldsymbol{A}$ is large, it implies that the columns are highly correlated and the neighboring elements of the sparse vector have very similar contributions to the measurement vector $\mathbf{y}$. Therefore, the indices added to the support by OMP may not correspond to the true sparse estimate. In case of LASSO or BP, high coherence means that the algorithm randomly selects one of the similar elements from the sparse estimate and shrinks the others. The selected position may be completely different from the true sparse estimate. Detailed explanation of the effects of coherence on LASSO can be found under the topic of 'neighbourhood stability condition' or the 'irreplacibility condition' [FFG22], [MY09].

Coherence and Range Resolution

Although the above outlined problem invalidates a straight-forward application of CS to this class of problems, there are two aspects from radar and CS which can be used to an advantage to get around this issue.

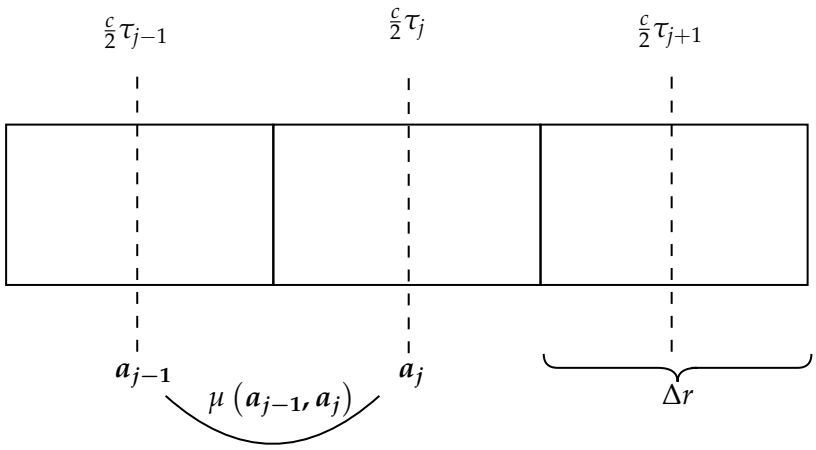

FIGURE 7.1: Illustration of the range grid defined by the columns of the CS sensing matrix.

Radar Range Cells: Theoretically, 'resolution' here refers to the Rayleigh resolution of a chirped waveform defined in Section 2.2.1. Here, the focus is placed on practical radar operation. In radar operation, the range is divided into discrete range cells. Each cell is centered around a range grid point, which corresponds to a range position $\frac{c}{2}\tau_j$. τ_j is defined by the entries of the sensing matrix as seen in previous chapters. Such a discretization of range is a natural consequence of the digital evaluation of the received signal. It is used to provide an approximation of the actual, possibly continuously-distributed positions of the targets in the scene.

The width of each cell in the range grid defines the desired range resolution Δr. Any object which lie in the range interval $\frac{c}{2}\left(\tau_j \pm \frac{\Delta\tau}{2}\right)$, is attributed to the same range cell by a CS algorithm, and has an estimated range of $\frac{c}{2}\tau_j$. This implies that if the width of the range cell is increased, i.e., a coarser grid is chosen, the CS algorithm will detect the multiple, off-grid targets in the range cell as one target at the corresponding range. The targets are of course indistinguishable in this case. If the width of the range cell is reduced, the CS algorithm provides an estimate on a fine grid. The multiple targets now lie in different range cells, and if the coherence of the CS matrix is low, the targets will be distinguishable.

The Coherence parameter from Compressed Sensing: The coherence of the derived sensing matrix, defined in Section 3.4, is given by the normalized maximum distance between the columns of the sensing matrix $\boldsymbol{A}$, i.e., the inner product of the normalized columns, where each column corresponds to a delay τ_j on the delay grid.

Matching both aspects Against this interpretation of coherence, it is clear that coherence and range cell width, or range resolution, points to the same concept from different perspectives. That is, the increase of the range cell width increases the spacing between consecutive grid points. Intuitively, this pushes the adjacent columns to be more 'dissimilar'. In other words, the mutual coherence between the columns of the sensing matrix is reduced, resulting in a better-conditioned matrix. Thus, lower the range resolution, coarser the range grid, lower the coherence value, and better is the CS estimation. The challenge is to obtain a higher resolution, i.e., an estimate on a fine range grid, despite this bottleneck.

Considering the worst-case scenario of targets present in adjacent range cells, the mutual coherence of two adjacent columns of the sensing matrix, as shown in

Fig. 7.1, is examined. Substituting the expression for the elements of the structured sensing matrix described in 4.14 into 3.4,

$$\begin{aligned}\mu\left(\mathbf{a_i}, \mathbf{a_{i+1}}\right) &= \max_{1\leq i\leq N} \frac{\left|\langle \mathbf{a_i}, \mathbf{a_{i+1}}\rangle\right|}{\|\mathbf{a_i}\|\|\mathbf{a_{i+1}}\|} \\ &= \max_{1\leq i\leq N} \frac{\left|\sum_{p=1}^{m}\left(\mathbf{a_{p,i}}^{*}\mathbf{a_{p,i+1}}\right)\right|}{\|\mathbf{a_i}\|\|\mathbf{a_{i+1}}\|} \\ &= \max_{1\leq i\leq N} \frac{\left|\sum_{p=1}^{m} s\left(f_p\right)^2\ e^{j2\pi\left(f_p+f_{\mathrm{Tx}}\right)\left(\tau_i-\tau_{i+1}\right)}\right|}{\left|\sum_{p=1}^{m} s\left(f_p\right)^2\right|} \\ &= \max_{1\leq i\leq N} \frac{\left|\sum_{p=1}^{m} s\left(f_p\right)^2\ e^{j2\pi\left(f_p+f_{\mathrm{Tx}}\right)\Delta\tau}\right|}{\left|\sum_{p=1}^{m} s\left(f_p\right)^2\right|}\,.\end{aligned}$$

From 3.18, it can be observed that

$$\mu\left(\mathbf{a_i}, \mathbf{a_{i+1}}\right) = \max_{1\leq i\leq N} \frac{\left|\sum_{p=1}^{m} s\left(f_p\right)^2\ e^{j2\pi\left(f_p+f_{\mathrm{Tx}}\right)\Delta\tau}\right|}{\left|\sum_{p=1}^{m} s\left(f_p\right)^2\right|} < \frac{1}{2s-1}\,. \tag{7.1}$$

(7.1) consolidates the relationship between the coherence μ, the sparsity s, and the grid width $\Delta\tau$, and is used later for an analytical bound on the subdivision step of the SF algorithm.

7.1.2 Algorithm Description

Based on the discussion in section 7.1.1, this section presents details of the 'Subdivision-Fusion Algorithm' [GBH+22]. Algorithm 4 denotes the subdivision step by S and the fusion step by B.

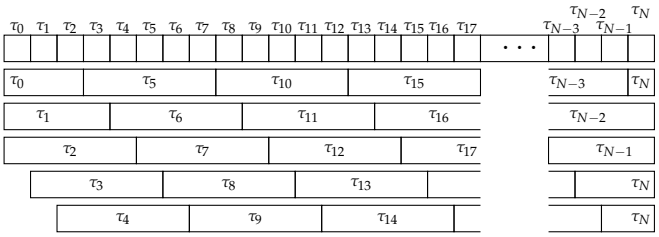

FIGURE 7.2: Illustration of sub-division of sensing matrix into coarse grid for pre-estimation: every k_{sub}-th (here: 5) fine-grid range cell becomes the center of a k_{sub} times larger coarse range cell or 'supercell'.

Subdivision: In order to reduce the coherence for better performance of CS problems, the specific structure of the sensing matrix due to the radar framework is used to an advantage. Every element of the sensing matrix $\boldsymbol{A}$ corresponds to a specific point in the frequency and delay grid, $A(f_i, \tau_j)$. Based on the discussion in 7.1.1, if sub-matrices are constructed by taking columns at a specific distance from each other in range, the coherence is lowered. Thus, $\boldsymbol{A}$ is divided into k_{sub} sub-matrices,

$$A_n(f_i, \tau_{j_n})\,, \tag{7.2}$$

where $i = 1, \ldots, m$, $j_n = n, n + k_{\text{sub}}, n + 2k_{\text{sub}}, \ldots, \frac{N}{k_{\text{sub}}}$, s.t, $\frac{N}{k_{\text{sub}}} \gg m$. The value of k_{sub} is chosen such that the sub-matrices are horizontal matrices, i.e., $2 \leq k_{\text{sub}} \leq \frac{N}{m}$. Now, the original measurement vector $\mathbf{y}$ is represented as $\mathbf{y} = \boldsymbol{A}_n \mathbf{x}_n$, $n = 1, ..., k_{\text{sub}}$.

These k_{sub} sub-problems are then directly solved using greedy methods or basis pursuit minimization, i.e.,

$$\mathbf{x}_n = \text{CS}(\boldsymbol{A}_n, \mathbf{y}) \ . \tag{7.3}$$

Fusion (Support Estimation) Let each element of these sub-matrices be known as a 'supercell'. Every supercell has k_{sub} fine-grid positions and is centered at a particular fine-grid position τ_{j_c}, as shown in Fig. 7.2. In the original problem, every element of the measurement vector $\mathbf{y}$ was represented by

$$y(i) = \sum_{j=1}^{N} A(f_i, \tau_j) x(j) \ .$$

Since the same measurement vector y is represented using coarse-grid sub-matrices, different estimates

$$y_n(j) = \sum_{j_n} A_n(f_i, \tau_{j_n})) x(j_n) \ , \tag{7.4}$$

are obtained, where $n = 1, \ldots, k_{\text{sub}}$, $i = 1, \ldots, m$, and $j_n = n, n + k_{\text{sub}}, n + 2k_{\text{sub}}, \ldots, \frac{N}{k_{\text{sub}}}$, s.t., $\frac{N}{k_{\text{sub}}} \gg M$.

If a target lies exactly on τ_{j_c}, the energy is maximum at the corresponding $x(j_n)$. On the other hand, if a target lies at the border of two coarse grid-cells, the energy is distributed almost equally between them, for eg., $x(j_n)$ and $x(j_{n+1})$. The value of $x(j_n)$ is the highest when the target is exactly on-grid and lower if the target is off-grid. In order to transfer the coarse-grid estimates from each sub-problem to a common fine-grid, a k-element Correction Factor (CF) array is constructed as follows.

First, an arbitrary on-grid target is considered on the fine-grid and the subdivision step is performed. This gives k_{sub} coarse-grid estimates for the said on-grid target. Since we know the on-grid target and corresponding the coarse-grid targets, the elements of the correction factor array CF can be obtained as the ratios of the fine and coarse grid estimates. The CF element at the supercell where the target lies exactly on τ_{j_c} will have a value of one and will be the central element of the CF array. CF values from the $\pm\frac{k_{\text{sub}}-1}{2}$ neighbouring cells fill the corresponding elements of the array. Multiplication of the results from each sub-problem with this CF array mimics an auto-correlation operation.

The individual fine-grid estimates from each sub-problem are then added and the whole target estimate becomes

$$x(j) = \sum \text{CF}(1 : \text{k}_{\text{sub}}) \ x(j_n) \ , \tag{7.5}$$

where $n = 1, \ldots, k_{\text{sub}}$. CS algorithms, such as BP or LASSO, do not give a binary estimate of the sparse vector, but a set of values representing the strength of each element $x(j)$ of the vector. Therefore, once the target estimate in the fine grid is obtained, a variance-based thresholding algorithm such as Otsu's method [O79] is used to filter the estimate before obtaining the final support. After thresholding, the corresponding support positions are stored in a support set S. For a simpler

implementation, a CF array of ones of length k_{sub} may also be used. Even in this case, the value of the summation in (7.1.2) will be highest for the correct position in the fine grid, and a stricter thresholding may be used.

Fusion (Target Estimation) The final estimate is given by solving a normal CS problem over the support set S which was obtained in the previous step, such that

$$\mathbf{x}_{\text{final}} = \text{CS}(\boldsymbol{A}_S, \mathbf{y}) \ . \tag{7.6}$$

Due to the use of CS again in the final estimation step, the 'subdivision-fusion' algorithm can be viewed as a nested-CS algorithm.

Algorithm 4: Subdivision-Fusion Algorithm-1

Data: sensing matrix $\boldsymbol{A}$, measurement vector $\mathbf{y}$
Result: $\mathbf{x}_{\text{final}}$
while $n <= k_{\text{sub}}$ **do**
  $I = 1$;
  for $J = 1$ **to** $\frac{N}{k_{\text{sub}}}$ **do**
    $A_n(I) := A(:, J)$;
    $I := I + 1$;
    $J := J + k_{\text{sub}}$;
  end
  $\mathbf{x}_n := S(\boldsymbol{A}_n, \mathbf{y})$;
end
$\mathbf{x}_{\text{final}} = B(\boldsymbol{A}, \mathbf{y}, \mathbf{x}_n)$;

7.1.3 Discussion

Comparison against Group sparsity: In many cases, CS can be viewed as a regression problem, where the aim is to find important explanatory elements that predict the response variables in $\mathbf{y}$. As opposed to individual elements, group sparsity based CS methods focus on selecting groups of input variables x_i that best represent the response variables. The strength of each group then depends on the basis $\boldsymbol{A}_i$. The extension of the popular LASSO problem to group sparsity gives [YL06]:

$$\left\| \mathbf{y} - \sum_{i=1}^{N} \boldsymbol{A}_i x_i \right\|^2 + \lambda \sum_{i=1}^{N} \|x_i\|_{K_i} \ , \tag{7.7}$$

where $\|x_i\|_{K_i} = (x_i' K_i x)^{\frac{1}{2}}$, K_i denotes the positive definite matrices that define the penalty term, and N refers to the number of groups. More details about group LASSO can be found in [MGB08].

The above equation represents $\mathbf{y}$ as the direct sum of $\boldsymbol{A}_i x_i$. In the Subdivision-Fusion algorithm, the individual CS problems may be viewed as different groups. However, $\mathbf{y}$ is not the direct sum of these groups. Due to the radar-based structure of the sensing matrix, it is important to perform the summation at the correct positions based on the correction factor described in Section 7.1.2.

Comparison against Fusion frames: A method to reconstruct a distributed sparse signal from unavailable or noisy measurements is discussed in [ABL18]. In this paper, a mathematical model of fusion frames is used in combination with modified CS concepts to divide the problem into smaller sub-problems. The individual CS results are then fused to obtain the final sparse estimate

$$\hat{\mathbf{x}} = {S_{\text{frame}}}^{-1} \left(\sum_{i=1}^{N} \hat{x}_i \right) , \tag{7.8}$$

where N is the number of groups, S_{frame} denotes the fusion frame operator defined in [ABL18, Theorem 2.3], and $\hat{x}_i$ denotes the individual CS estimates from local recovery problems.

[ABL18] assumes that the scene has distributed sparsity. Therefore, each subspace of the fusion frame system deals with a different part of the scene and captures a different portion of the sparse estimate. However in this paper, the same scene is detected using different parts of the frequency spectrum. The work presented in this paper involves the subdivision of the sensing matrix corresponding to different parts of the frequency spectrum—it does not involve subdivision of the scene.

Limitations based on sparsity: The design of a radar system limits the number of measurements, m. Additionally, the requirement for low coherence of the sensing matrix $\boldsymbol{A}$ limits the super-resolution factor, i.e., the number of fine grid points N that can be supported. Therefore, given a specific m and N, an upper-bound on the sparsity s of the scene can be determined from the relation [FR13, p.271],

$$m \geq 2s \ln(N/s) \tag{7.9}$$

Since $N \gg s$, (7.9) can be approximated to

$$m \geq 2s \ln(N) , \tag{7.10}$$

which makes $\frac{m}{2\ln(N)}$ the upper bound of sparsity, in the case of a given N and limited number of measurements m.

Another limitation of this approach, which is also given by the above inequalities, relates to the maximal factor for the coarse grid. If it is assumed that for a sparsity s all objects fall into different coarse cells and all k_{sub} fine grid positions of these coarse cells are selected as possible support positions, a total of sk_{sub} possible support positions are defined for the calculation of the second stage of the algorithm. Since this stage performs a CS estimation based on a selection of sk_{sub} columns of A, sk_{sub} should not surpass m, i.e, $m \geq sk_{\text{sub}}$, which is however the exact same inequality as in (7.9), (7.10). That means

$$\frac{m}{s} \geq k_{\text{sub}} = 2\ln(N/s) ,$$

if the tighter bound based on (7.9) is used.

Furthermore, k_{sub} may be determined analytically from the relation between the cell width, the coherence and the sparsity defined in (7.1). Expanding (7.1) for the coarse-grid case,

$$\mu\left(\mathbf{a_i}, \mathbf{a_{i+1}}\right) = \max_{1 \leq i \leq N} \frac{\left| \sum_{p=1}^{m} s\left(f_p\right)^2 \; e^{j2\pi\left(f_p + f_{\text{Tx}}\right)\left(k_{\text{sub}-1}\right)\Delta\tau} \right|}{\left| \sum_{p=1}^{m} s\left(f_p\right)^2 \right|} < \frac{1}{2s-1} . \tag{7.11}$$

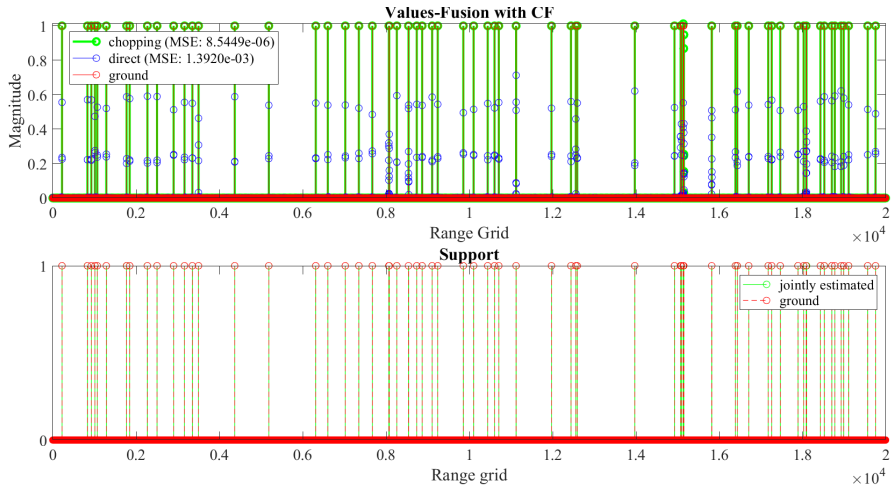

FIGURE 7.3: Top figure shows the reconstruction results from the Subdivision-Fusion Algorithm (in green) and the direct BLASSO (in blue). The ground truth is denoted in red. The bottom figure shows the support estimated by the Subdivision-Fusion Algorithm (in green) and the support of the ground truth (in red) [GBH+22].

.

Therefore, the coherence acts as a bridge between the sparsity s and the number of submatrices, k_{sub}, needed for a unique reconstruction.

Relation to chirp sensing matrices A similar concept using a structured sensing matrix is explored in [AHS+09]. Here, chirps define columns of the sensing matrix, with each chirp having a different base frequency and chirp rate. The measured signal is thus a weighted combination of a number of different chirps. However, in this work, a single gapped-chirp is considered as the measured signal, in accordance to the radar framework. [AHS+09] does not mention any links to radar application.

Relation to sequential estimation methods [DTD+12] defines the problem of missing measurements as a case of having a well-determined but noisy system. This work uses the stOMP algorithm to sequentially generate sparse estimates and perform stage-wise fusion. Although the problem addressed is similar, the method is significantly different from the current work, since here the sparse estimates are independently generated and combined in a single fusion step.

7.1.4 Results

This section presents results demonstrating the performance of the proposed algorithm. First, simulation results from the SF algorithm are compared to a direct CS method for a particular scene. In all the following simulations, BLASSO is used as the CS method [dG12].The SF and direct BLASSO algorithms are tested for different levels of noise and further analysed using phase transition diagrams. The algorithm is also tested on real measurement data.

Simulation Results

As demonstrated in section 7.1.1, the mutual coherence problem depends only on the ratio of the missing data to the available data, and not on the bandwidth itself. Therefore, in the interest of computational load for the simulations, a frequency band of 5 kHz has been used for the simulations. The gap is half of the whole bandwidth, i.e., 2.5 kHz. Based on the sensing matrix derivation discussed in Section 6.2.2, a matrix $\boldsymbol{A}$ is constructed using the frequency domain representation of measurement vector $\mathbf{y}$. Considering the width of the missing band to be half the total bandwidth and a pulse duration of 0.5 seconds, $\mathbf{y}$ consists of 2500 measurement samples. The range grid is constructed with 10000 grid points, with the grid-spacing depending on the range resolution corresponding to the bandwidth.

Fig. 7.3 shows the estimated support and the reconstruction result from the Subdivision-Fusion algorithm and the BLASSO. The target scene consists of 70 point targets (in red) with magnitudes of 1, placed at randomly selected range grids, i.e., with a random support. The circles represent the peaks of these targets. The number of targets is within the theoretical bounds on sparsity given by (7.9) and (7.10),. The frequency domain sensing matrix described in (6.9) is used and f_{Tx} is set to zero for convenience. The mean-squared error from the Subivision-Fusion algorithm is found to be 8.5449e^{-6}, while that from the BLASSO method is 1.3920e^{-3}. This proves that the proposed method is much more effective that direct CS in the gapped-band scenario. It is evident from Fig. 7.3 that BLASSO (in blue) gives a large number of false positives near the actual target. For particular target (in red), there appears to be a single sharp estimate from the Subdivision-Fusion algorithm (in green), while there are a number of smaller peaks from BLASSO (in blue). This means that the Subdivision-Fusion algorithm provides sharper peaks at the correct locations, while BLASSO results in multiple lower peaks due to the coherence issues described in the previous section. This observation is in agreement with the mean-squared error values. However, it is interesting to note that the performance of the Subdivision-Fusion algorithm also degrades when 2 targets are very close to each other. This is seen, for instance, between the range grid points 1.4 and 1.6. In this case, even the Subdivision-Fusion algorithm does not provide a single sharp peak, and multiple lower peaks are observed around the correct range location. However, the performance is still better compared to direct CS and in general, Subdivision-Fusion algorithm gives a better reconstruction, with fewer false positives.

Next, both the algorithms are tested for gaps of different widths in the presence of noise. Gaussian white noise is added to the received signal $\mathbf{y}_{\text{Rx}}^{b}$ in the time domain. Fig. 7.4 demonstrates the performances of both algorithms for gaps of widths corresponding to 0.2, 0.3, 0.4 and 0.5 of the total bandwidth. In each case, the Signal-to-Noise ratio (SNR) is varied from 0 to 20 dB. It is observed that the Subdivision-Fusion algorithm performs better than direct BLASSO for lower values of SNR, specially in the range of 0-10 dB.

Phase Transition Diagrams In order to analyze the performance of the proposed algorithm for different levels of sparsity and different dimensions of A, phase transition diagrams are constructed. These diagrams represent the probability of a successful reconstruction over different levels of sparsity and different numbers of measurements. In the following plots, $\frac{m}{N}$ denotes the ratio of the number of available measurements to the number of range grids, and $\frac{s}{m}$ denotes the ratio of sparsity to the number of measurements. The simulations are structured as follows. The ratios $\frac{m}{N}$ and $\frac{s}{m}$ are varied from 0.05 to 1 in steps of 0.05 and for every point $(\frac{m}{N}, \frac{s}{m})$, 50

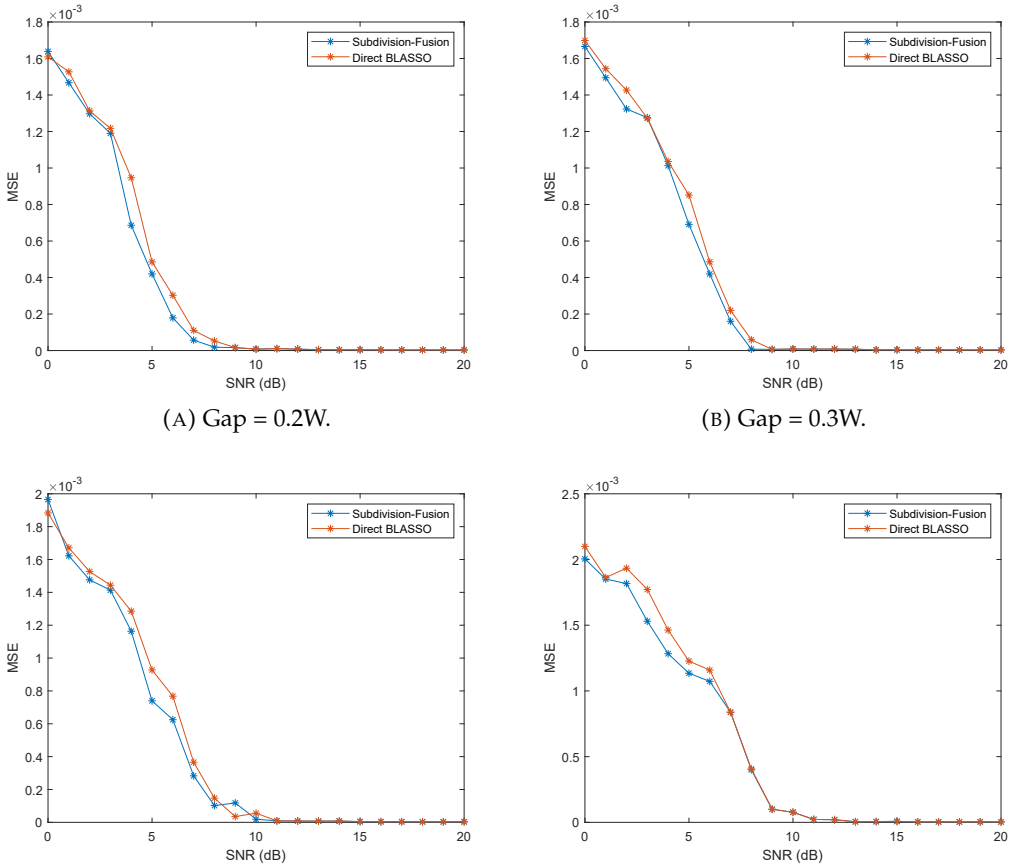

(A) Gap = 0.2W.

(B) Gap = 0.3W.

(C) Gap = 0.4W.

(D) Gap = 0.5W.

FIGURE 7.4: SNR vs MSE plots for gaps of different widths [GBH+22].

iterations of the proposed method are executed. The success or failure of each iteration is determined by calculating the mean-squared error between the ground truth and the reconstruction result. An error of 0.01 or less is considered a success. The averaged rate of success over 50 iterations is then shown in the corresponding position in the phase transition diagram. Since the sensing matrix is always horizontal $(N \gg m)$, the number of columns (N) considered for the phase transition diagrams must correspond to the maximum number of available measurements (m).

Fig. 7.5 shows the phase transition diagrams for the direct CS and Subdivision-Fusion algorithm applied to the gapped-band problem. When the number of measurements (m) are lower, the Subdivision-Fusion algorithm shows a higher success probability compared to direct CS. In particular, when the ratio $\frac{m}{N}$ goes above 0.2, the success probability shows a larger increase for the Fusion method as compared to the direct CS method. Due to the use of only 50 iterations per point and random selection of target positions in each iteration, a variance is noticeable and the rise in success probability is not very smooth. However, a clear distinction in performance is obtained, specially when the number of measurements m are lower. Fig. 7.6 gives the phase transition diagrams for the Subdivision-Fusion algorithm using the traditional Fresnel integrals and the PSP approximation [KPD+60; R14; LM04]. 5 iterations have been used per point. The probability of success is similar for same values of s/m and m/N, thereby demonstrating that PSP provides a good approximation to the Fresnel Integral method discussed in Section 2.2.2. Fig 7.7 shows the phase transition diagrams in the case of two gaps having widths of 0.5 and 0.2 of the

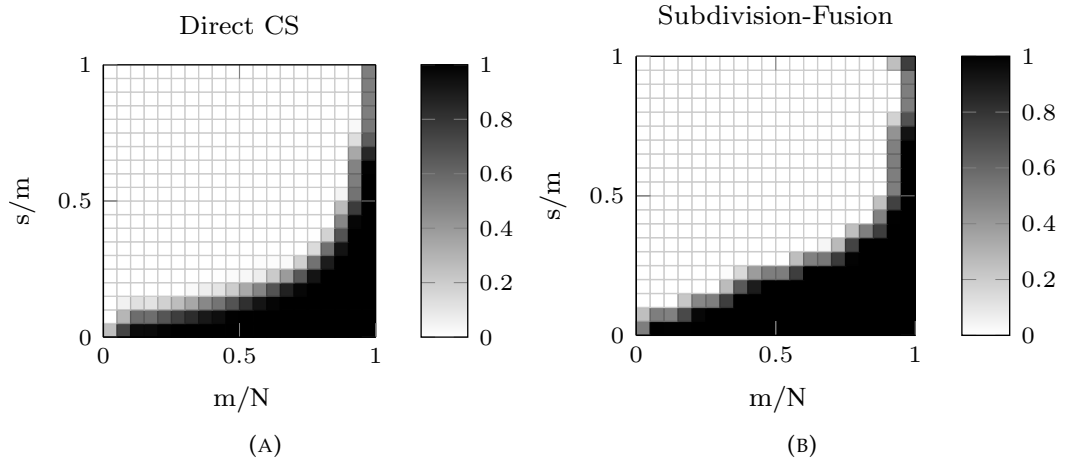

FIGURE 7.5: Phase Transition diagrams for (A) Direct CS and (B) Subdivision-Fusion Algorithm. Black corresponds to 100% empirical success probability. White corresponds to 0% success probability [GBH+22].

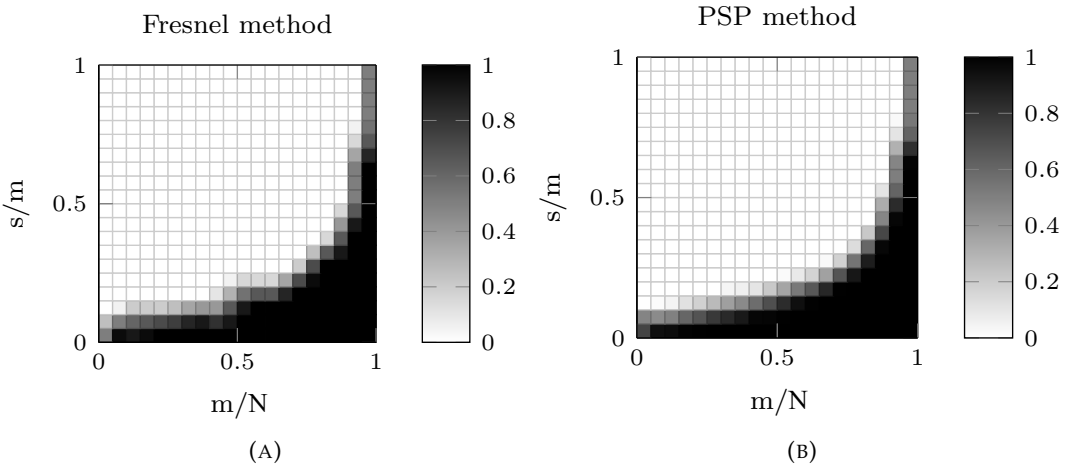

FIGURE 7.6: Phase Transition diagrams for (A) the exact chirp model (Fresnel) and (B) the approximation (PSP) [GBH+22].

whole frequency band. 5 iterations have been used per point for both algorithms. As expected, for both methods, the probability of success reduces in comparison to the single gap scenario. The figure shows better performance of the Subdivision-Fusion algorithm, specially in the 0.6 to 0.8 range for m/N.

Application to Real Measurement Data : Proof of Concept

In order to present an initial proof of concept using real world data, an FMCW radar of bandwidth 24 GHz has been used to detect a point on metal plate at a distance of 0.32 m from the radar. The FMCW radar operates using a transceiver unit, i.e., the same unit is used to transmit and receive the signal. A focusing horn lens antenna with a 5 degree opening angle has been used for this experiment. Fig. 8.4 shows the measurement setup. It must be noted that since only a point target is being detected, this experiment does not aim to prove the resolution capabilities of the

1

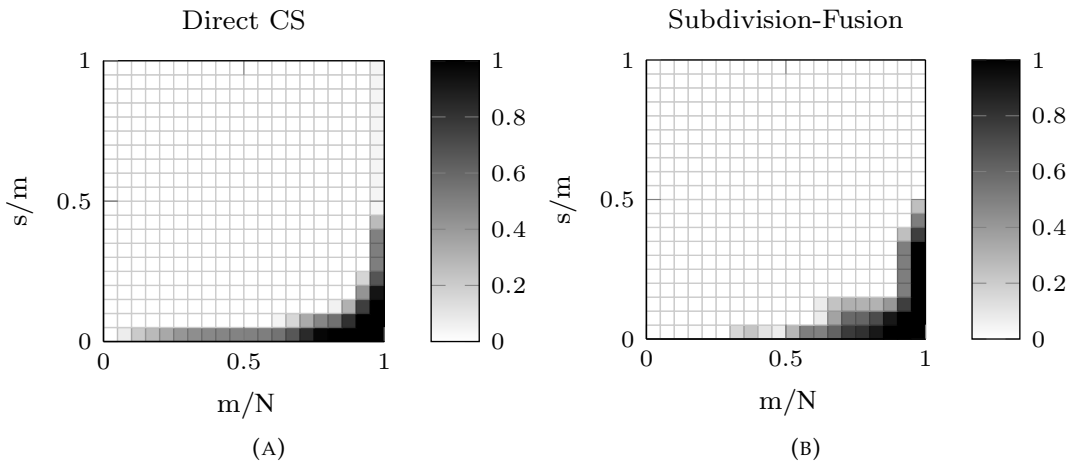

FIGURE 7.7: Phase Transition diagrams for (A) direct CS and (B) Subdivision-Fusion Algorithm with multiple gaps. The Subdivision-Fusion algorithm performs better than direct CS for $m/N > 0.5$ [GBH+22].

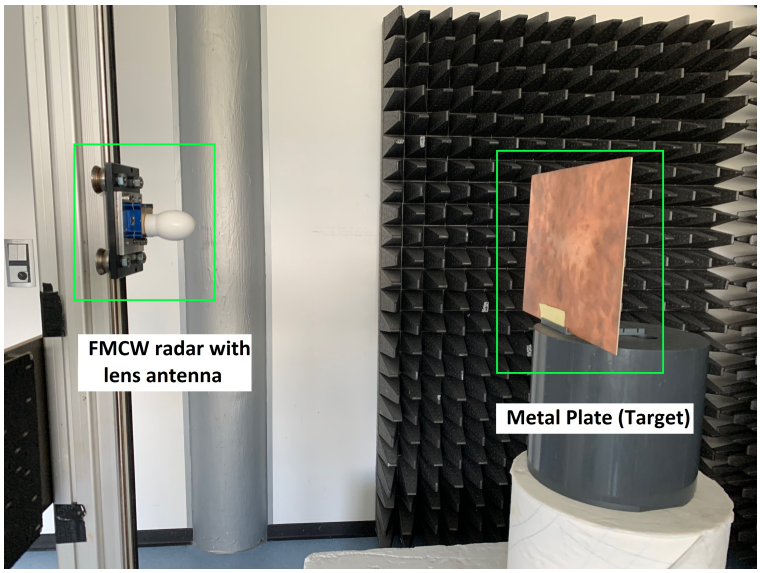

FIGURE 7.8: Experimental Setup.

proposed algorithm. The goal is to introduce a continuous band gap and verify that the performance on real measurement data aligns with the simulation results. First, an FFT is performed on the measurements from the entire frequency band. It is seen that, apart from the main peak corresponding to the location of the point target, there exists several smaller peaks due to internal reflections in the experimental setup. These may be considered to be additional targets. This does not affect the validity of the results, since the goal is to identify the location of each target as they appear.

To test the performance of the Subdivision-Fusion Algorithm, gaps having a width of 0.1, 0.3, 0.5, and 0.7 of the total bandwidth are introduced, which correspond to a gap in time as described in Section 6.2.2 and the dedicated FMCW-based sensing matrix from (6.15) is used. Fig. 7.9 shows the corresponding results. The ground truth is shown in red, the direct BLASSO results are shown in blue, while the Subdivision-Fusion results are shown in green. For all cases, a prominent peak

1

is observed at the correct range positions. It is observed that the results from the Subdivision-Fusion algorithm have a lower mean-squared error compared to those from the direct BLASSO for wider gaps in the frequency band. Since the aim is to recover the ground truth resolution in the presence of a band gap, the difference in error is not as large as it would be for super-resolution. Nevertheless, the error values show that the proposed algorithm performs better when the coherence is high.

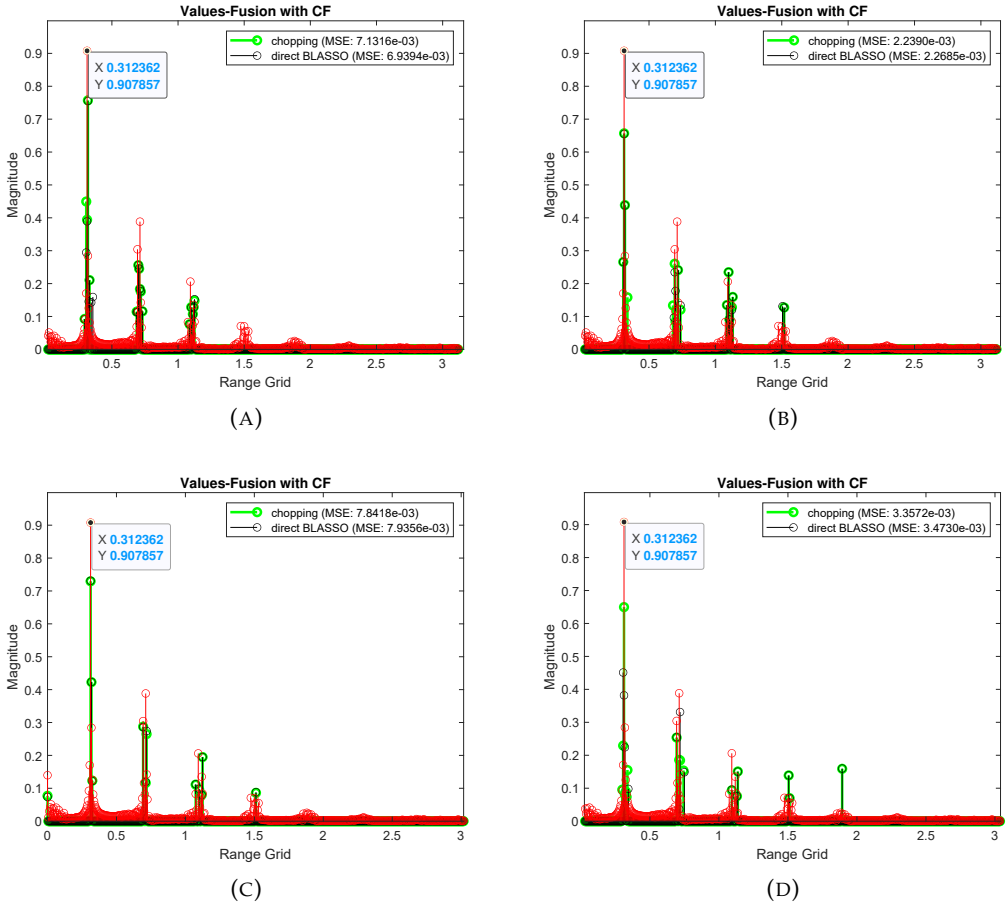

FIGURE 7.9: Reconstruction results from the Subdivision-Fusion Algorithm (in green) and the direct BLASSO (in black) for gaps of (A) 0.1, (B) 0.3, (C) 0.5, and (D) 0.7 of the total bandwidth. The ground truth is denoted in red [GBH+22].

Application to FMCW

In this section, a slightly different version of the fusion step is first proposed, followed by results on real FMCW data [GBE23]. Algorithm 5 denotes the subdivision step by S and the fusion step by B. The algorithm consists of the following steps:

1. Subdivision: Identical to 4, the sensing matrix is divided into k_{sub} coarse-grid, low-coherence sub-matrices, by taking every k_{sub}-th column from the original sensing matrix. This results in k_{sub} CS problems giving coarse-grid estimates of $\mathbf{x}$,

$$\mathbf{x}^i_{\text{sub}} = CS(\boldsymbol{A}^i_{\text{sub}}, \mathbf{y}) \ ,$$

where $i = 1, \ldots, k_{\text{sub}}$.

2. Fusion (Support Estimation): The main modification from 4 lies in the coarse to fine grid transfer of the k_{sub} estimates. In 4, a correction factor array was first constructed from an assumed on-grid target and then multiplied to the coarse-grid estimates of $\mathbf{x}$, giving the fine-grid estimates needed for fusion. Here, first the coarse-grid estimate $\mathbf{y}_{\text{coarse}}$ of the original measurement vector is determined from each $\mathbf{x}$ estimate by

$$\mathbf{y}^i_{\text{coarse}} = \boldsymbol{A}^i_{\text{sub}} \mathbf{x}^i_{\text{sub}} \, .$$

Based on the sensing matrix construction, each coarse-grid position corresponds to k_{sub} fine grid positions given by

$$S_{\text{fine}} = C_{\text{fine}} - ((k_{\text{sub}} - 1)/2) : C_{\text{fine}} + ((k_{\text{sub}} - 1)/2) \, ,$$

where $C_{\text{fine}} = k_{\text{sub}} S_{\text{coarse}} + (i - k_{\text{sub}})$, S_{coarse} denotes the support on the coarse grid, C_{fine} denotes the fine grid position corresponding to the center of the coarse grid, and S_{fine} represents the support in the fine grid.

3. Fusion (Target Estimation): Each coarse grid estimate is then projected to get k_{sub} fine grid estimates given by

$$\mathbf{x}_{\text{fine}}(S_{\text{fine}})^i = \boldsymbol{A}^T(S_{\text{fine}}, :) \mathbf{y}^i_{\text{coarse}} \, .$$

The final estimate is then obtained by adding the k_{sub} fine grid estimates and re-using CS to give

$$\mathbf{x}_{\text{final}} = \text{CS}(\boldsymbol{A}_{S_{\text{fine}}}, \mathbf{y}, \mathbf{x}_{\text{fine}}) \, . \tag{7.12}$$

$\mathbf{x}_{\text{fine}}$ can be directly used as the final estimate. However, the final CS step provides a sparser estimate at a low computational cost, since only the relevant S_{fine} positions need to be considered. This final step may be replaced by a thresholding step for a faster implementation. In addition, this method may be applied using the FFT by implicitly considering the FFT at indices determined by the subdivision-fusion algorithm at every step. Such an approach would completely bypass the sensing matrix formulation and storage, and would further generalize the algorithm.

Algorithm 5: Subdivision-Fusion Algorithm-2

```
Data: sensing matrix A, measurement vector y
Result: x_final
while n <= k_sub do
    I = 1;
    for J = 1 to N/k_sub do
        A_n(I) := (A(:, J));
        I := I + 1;
        J := J + k;
    end
    x_n := S(A_n, y);
end
x_final = B(A, y, x_n);
```

The range resolution performance of the proposed SF algorithm is analyzed based on 2 popular CS algorithms - the spectral projection gradient method for

solving the Basis Pursuit De-noising (SPG-BPDN) problem [CDS98] and the Iterative Soft Thresholding Algorithm (ISTA) [DDD04]. The COBRA radar at Fraunhofer FHR is used to determine the simulation parameters (bandwidth, pulse width, time samples) for the synthetic test data and also to obtain the final 'ground truth' measurements, i.e., measurements with no band gap. It is an FMCW radar with a 4 GHz bandwidth operating in X band. A gap is then artificially introduced in the frequency band and the sensing matrix is designed as detailed in 6.2.2, to mimic 2 narrow-band FMCW radars operating in disjoint bands, separated by the specified gap.

Simulation Results: In practice, the range resolution depends not only on the bandwidth, but also on the number of time samples considered during measurement. For 1535 time samples, the COBRA system was found to resolve 2 targets at a minimum distance of 20 cm apart. Simulations are carried out based on these parameters from the real measurement setup. Therefore, 2 targets are initially considered at a distance of 20 cm, and are then brought increasingly closer by incrementing the super-resolution (SR) factor, i.e., the number of range cells separating the targets are kept constant while the width of the range cells are reduced, i.e., the range resolution is increased. In addition, the band-gap is also increased, making the problem quite ill-posed. The performance of the algorithm is tested for different values of band-gap and SR factor. It is observed in Fig. 7.10, 7.11 that although the direct CS algorithm does not completely fail, the SF algorithm is able to achieve much sharper peaks with better isolation of the targets and lower side-lobes, specially in case of a larger band-gap having a width of 0.7 times the total bandwidth. Fig. 7.12 shows the mean-squared error (MSE) and root-mean-squared (RMS) contrast values for this two target scene, for different band gaps upto an SR factor of 4. The RMS contrast refers to the standard deviation of intensities of the targets in the scene. For the same SR factor, the RMS contrast values are much higher for the SF results as compared to the direct CS results. The MSE plots show a reverse trend as expected, with the MSE values of the SF results being much lower compared to that of the direct CS results. Additionally, it is found that for this particular scene, the direct ISTA fails above an SR factor of 4 with a gap of 0.7BW, while the SF ISTA fails for an SR factor of 12 with a gap of 0.7BW. The direct BPDN fails for an SR factor of 4 while the SF BPDN fails for an SR factor of 10 with a gap of 0.5BW. Therefore, the SF algorithm is able to support higher SR factors as compared to the direct CS methods.

Results on real measurements—Car on a turntable: To test the algorithm on real data, a car was placed on a turntable and ISAR measurements were obtained using the COBRA radar. The standard Polar Format algorithm was used for image formation. The gap was introduced in the frequency domain before conversion into the polar coordinates.

Fig. 7.13 shows the gaps in frequency as it appears in the polar coordinates $k_x - k_y$. Fig. 7.14 shows the performances of the matched filter, direct CS and SF algorithms for band gaps of 0.3 and 0.5 of the total bandwidth. Here, the SF algorithm uses ISTA as the reconstruction method. A super-resolution (SR) factor of 2 is also tested. The RMS contrast, denoted by 'Cont', is used as the metric for performance comparison. As previously mentioned, it represents the standard deviation of the intensities of the targets in the scene. It is observed that for gapped cases, both CS methods have a higher contrast in comparison to the matched filter. The results from the SF algorithm have a higher contrast than those from the direct CS

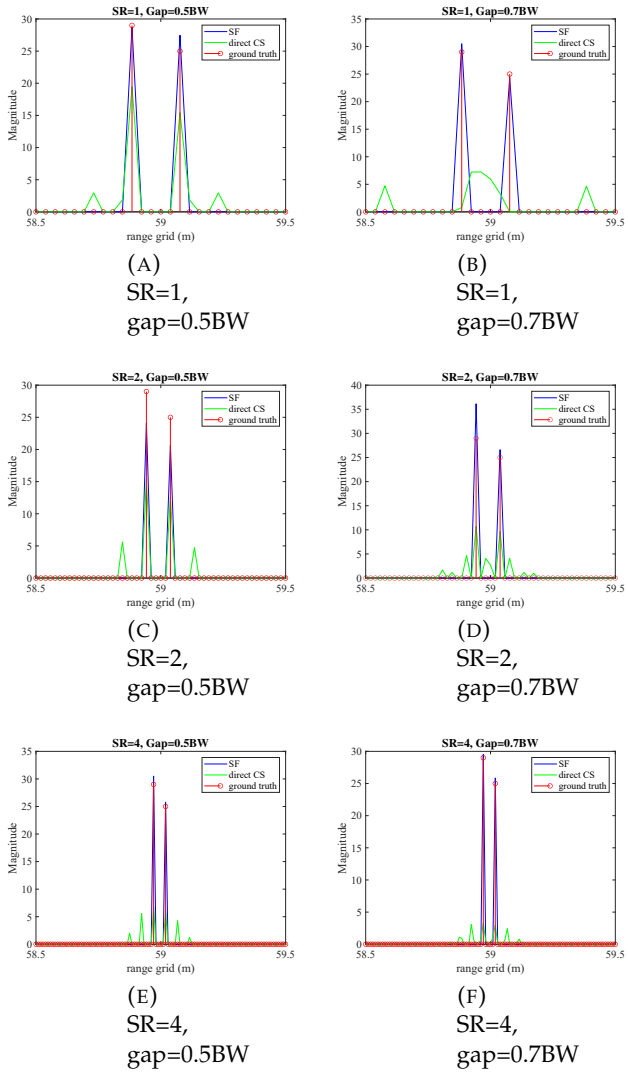

(A) SR=1, gap=0.5BW

(B) SR=1, gap=0.7BW

(C) SR=2, gap=0.5BW

(D) SR=2, gap=0.7BW

(E) SR=4, gap=0.5BW

(F) SR=4, gap=0.7BW

FIGURE 7.10: Performance of ISTA based SF v/s direct ISTA [GBE23].

algorithm. This is expected since the subdivision step promotes sparser results, and the final thresholding step in the fine grid further promotes the sparsity. Table. 7.2 consolidates the RMS contrast values for MF, ISTA, and ISTA-based SF (SF-ISTA) methods.

Application to Real Measurement Data: SAR

This section discusses the application of the Subdivision-Fusion Algorithm to SAR data. Here, the data used is the new Delhi scene from Terrasar-X, shown in Fig. 7.15. First the Hamming window effect is removed from the data, and then a band gap is introduced along the range frequencies. Since the scene is very large, smaller parts of the scene are used to visualize the effects of the applied algorithms. Figs. 7.16, 7.17, 7.18 focus on a part of the scene for a gap of 0.2W. Figs. 7.16, 7.17, 7.18 correspond to a different part of the scene for a gap of same width. Similarly, Figs. 7.22, 7.23, 7.24, and 7.22, 7.23, 7.24 show different parts of the scene for a gap of 0.5W. Table. 7.3 summarizes the RMS contrast values of the figures for gaps of different widths.

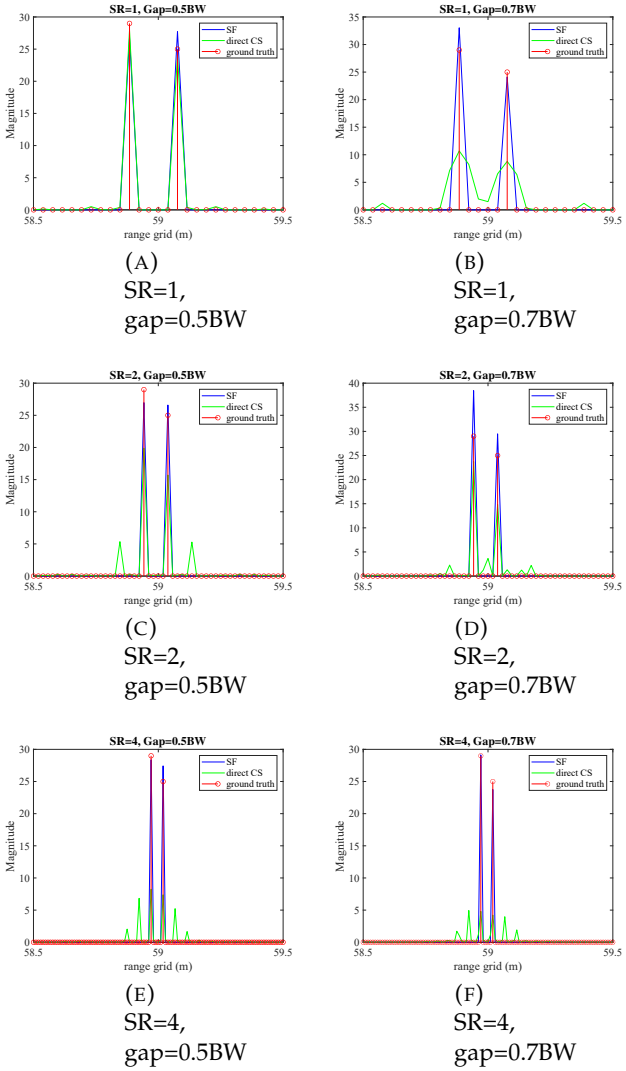

(A) SR=1, gap=0.5BW

(B) SR=1, gap=0.7BW

(C) SR=2, gap=0.5BW

(D) SR=2, gap=0.7BW

(E) SR=4, gap=0.5BW

(F) SR=4, gap=0.7BW

FIGURE 7.11: Performance of SPG-BPDN based SF v/s direct SPG-BPDN [GBE23].

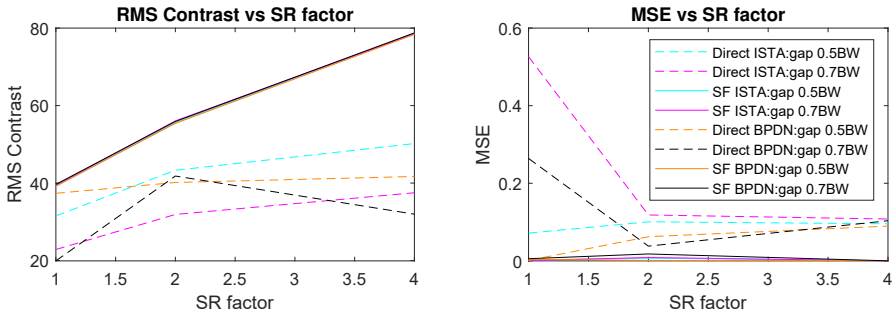

FIGURE 7.12: Comparison based on MSE and RMS contrast [GBE23].

7.2 A CS based Approximated Observation algorithm

Direct compressed sensing methods that use model-based structured sensing matrices pose a large computational load, specially for SAR systems, since they typically generate a large volume of data. The previous section discussed a subdivision-based

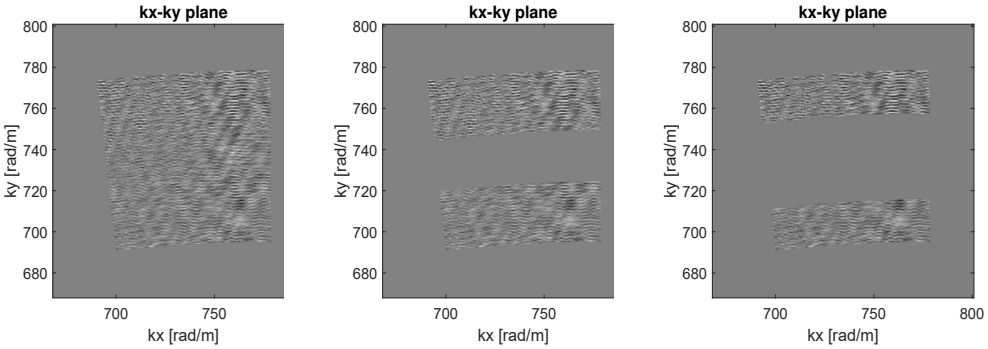

(A) (B) (C)

FIGURE 7.13: Gapped Bands in Polar Coordinates.

TABLE 7.2: RMS Contrast values for MF, ISTA and SF- FMCW.

Gap (W)	Method	Contrast
0	MF	1.4569
0	ISTA	2.5901
0.3 W	MF	1.4069
0.3 W	ISTA	2.3656
0.3 W	SF	5.2858
0.3 W	SF, SR=2	7.4788
0.5 W	MF	1.3749
0.5 W	ISTA	2.2499
0.5 W	SF	5.2858
0.5 W	SF, SR=2	7.0878

TABLE 7.3: RMS Contrast values for MF, ISTA and SF- SAR.

Gap (W)	Method	Contrast
0.2 W	MF	2.2969
0.5 W	MF	1.9303
0.2 W	ISTA	5.7510
0.5 W	ISTA	6.2690
0.2 W	SF	9.3551
0.5 W	SF	7.8838

approach to tackle this problem, where the structed sensing matris was subdivided, leading to smaller CS problems and lower computational load. In this section, another approach known as the 'Approximated Observation' is discussed. The preliminaries behind approximated observation are first explained, followed by the algorithm, and simulation results. Results based on SAR data from TerraSAR-X are also presented.

7.2.1 Preliminaries

As detailed in [FXZ+14], CS methods can be used to achieve an improvement in resolution of SAR systems. However, the use of an 'exact observation function', i.e., a sensing matrix $\boldsymbol{A}$ based on the exact signal model poses a large computation

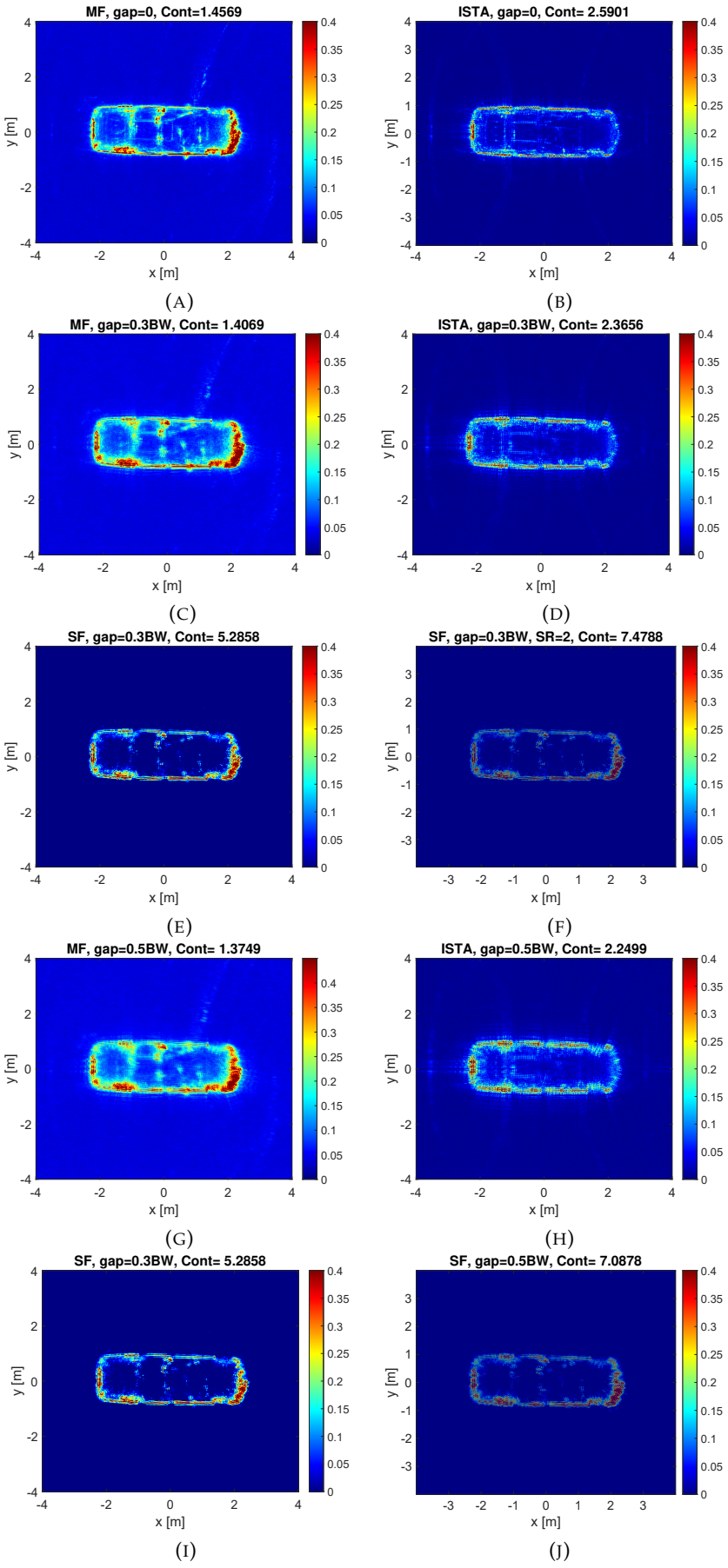

FIGURE 7.14: Results from Matched filter (MF), direct CS and Subdivision-Fusion (SF) algorithm for different band-gaps and super-resolution (SR) factors. The colorbars represent the root-mean-square (RMS) contrast values [GBE23].

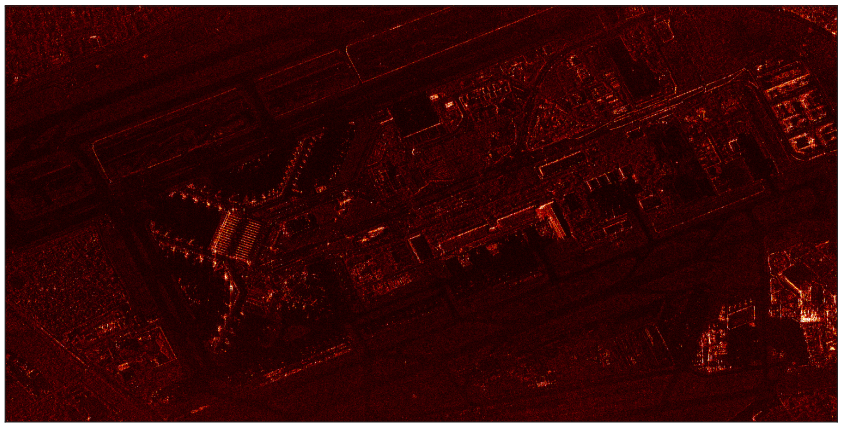

FIGURE 7.15: New Delhi scene from TerraSAR-X.

complexity and memory cost. The main idea of the Approximated Observation approach, is to replace this exact observation model by approximated observations obtained via the inverse of traditional Matched Filter (MF) based procedures.

Mathematically, this may be expressed as follows. Let, $\boldsymbol{M}$ denote an MF-based SAR image formation algorithm such as the Range-Doppler algorithm or Range-Migration algorithm, discussed in Chapter 2. The relation between the SAR raw data $\mathbf{y}$ and the image $\hat{\mathbf{x}}$ is given by

$$\hat{\mathbf{x}} = \boldsymbol{M}\mathbf{y}, \tag{7.13}$$

where $\hat{\mathbf{x}}$ is an approximation of the scene. If there exists an inverse of the SAR image formation algorithm, the raw data $\mathbf{y}$ may be expressed as

$$\mathbf{y} = \boldsymbol{M}^{-1}\hat{\mathbf{x}}. \tag{7.14}$$

Comparing (7.14) with the CS formulation $\mathbf{y} = \boldsymbol{A}\mathbf{x}$, it is evident that $\boldsymbol{M}^{-1}$ can be used to approximate the operation represented by the sensing matrix $\boldsymbol{A}$. Therefore, in a CS algorithm, whenever there is an operation involving the sensing matrix, it can be replaced by the inverse steps of a conventional SAR image formation algorithm. $\boldsymbol{A} \approx \boldsymbol{M}^{-1}$ converts the SAR image $\hat{\mathbf{x}}$ to SAR measurements $\mathbf{y}$, and is known as the 'Measurement Simulator'. $\boldsymbol{A}^H \approx \boldsymbol{M}$ is referred to as the 'SAR Processor'. Based on this discussion, an ISTA-based Approximated Observation algorithm for gapped-band SAR is described in the following section.

7.2.2 Algorithm Description

The proposed ISTA based Approximated Observation algorithm is illustrated in Fig. 7.29 and described as follows [GBE22]. Consider $\mathbf{y}$ to be the original measurements in the gapped frequency band. A conventional SAR Processor, $\boldsymbol{A}^H$, is used to get the corresponding (low resolution) image $\hat{\mathbf{x}}$. Normally, this would be the final image. Here, this serves as the starting point of the ISTA loop. The image $\hat{\mathbf{x}}$ goes through the soft thresholding-step of the ISTA algorithm and is then sent to the 'Measurement Simulator', $\boldsymbol{A}$. The Measurement Simulator takes the thresholded $\hat{\mathbf{x}}$ as the input image and gives back the corresponding measurements $\hat{\mathbf{y}}$. Thus, $\hat{\mathbf{y}}$ represents the approximated measurements corresponding to a sharper image obtained after

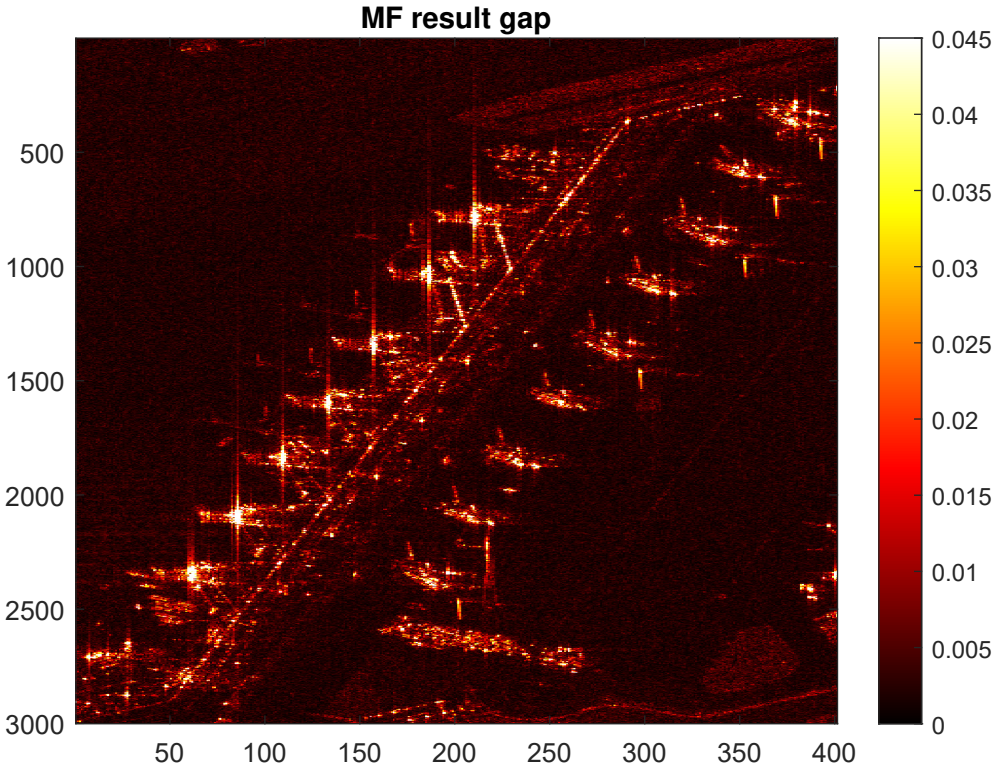

FIGURE 7.16: MF result for a gap of 0.2BW.

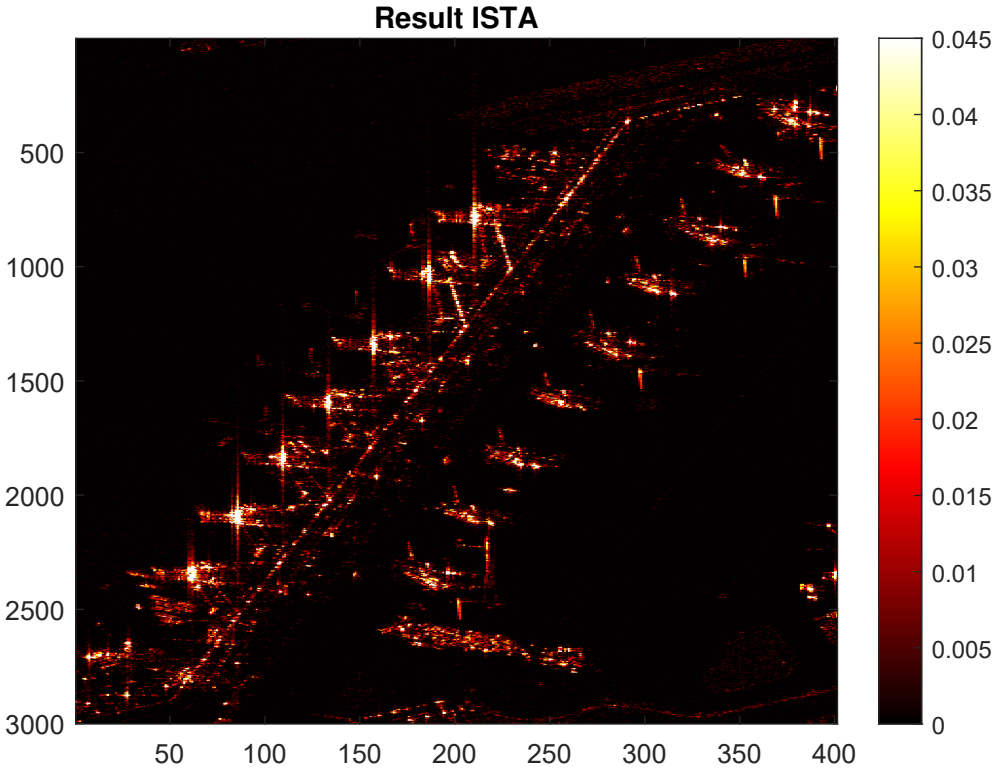

FIGURE 7.17: ISTA result for a gap of 0.2BW.

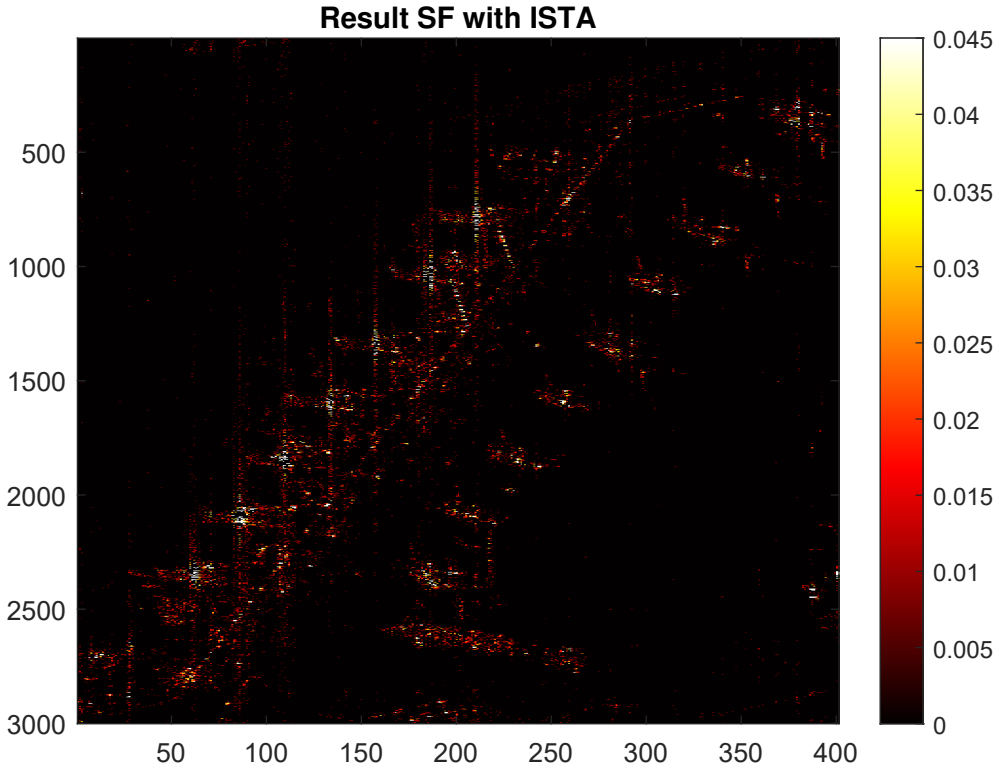

FIGURE 7.18: SF result for a gap of 0.2BW.

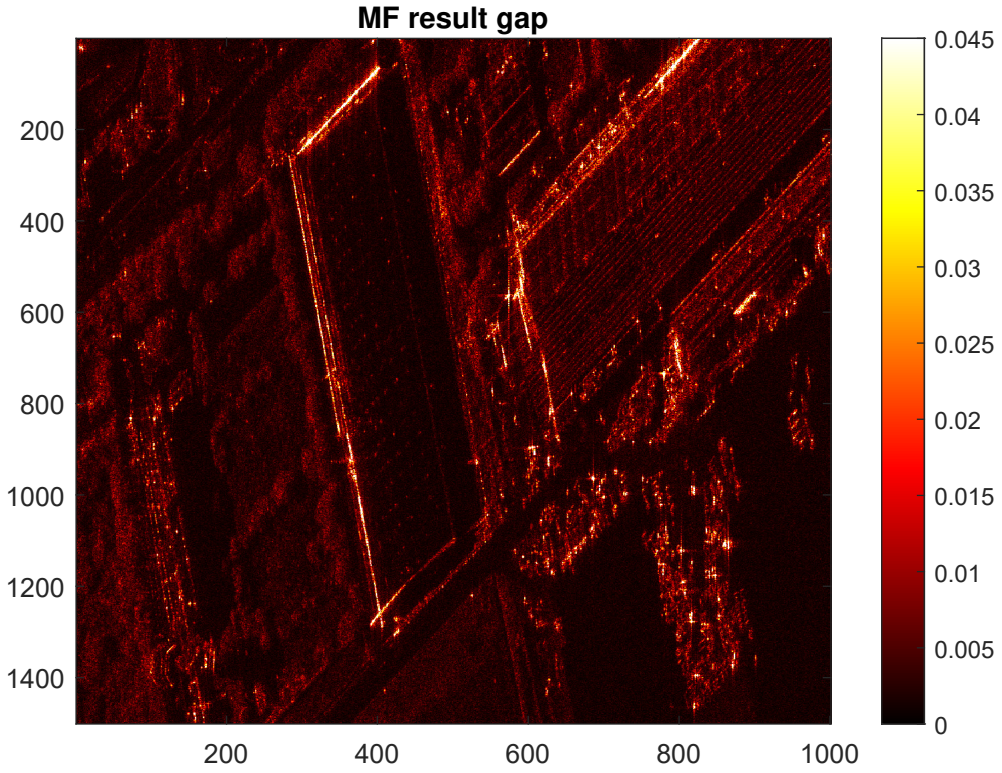

FIGURE 7.19: MF result for a gap of 0.2BW.

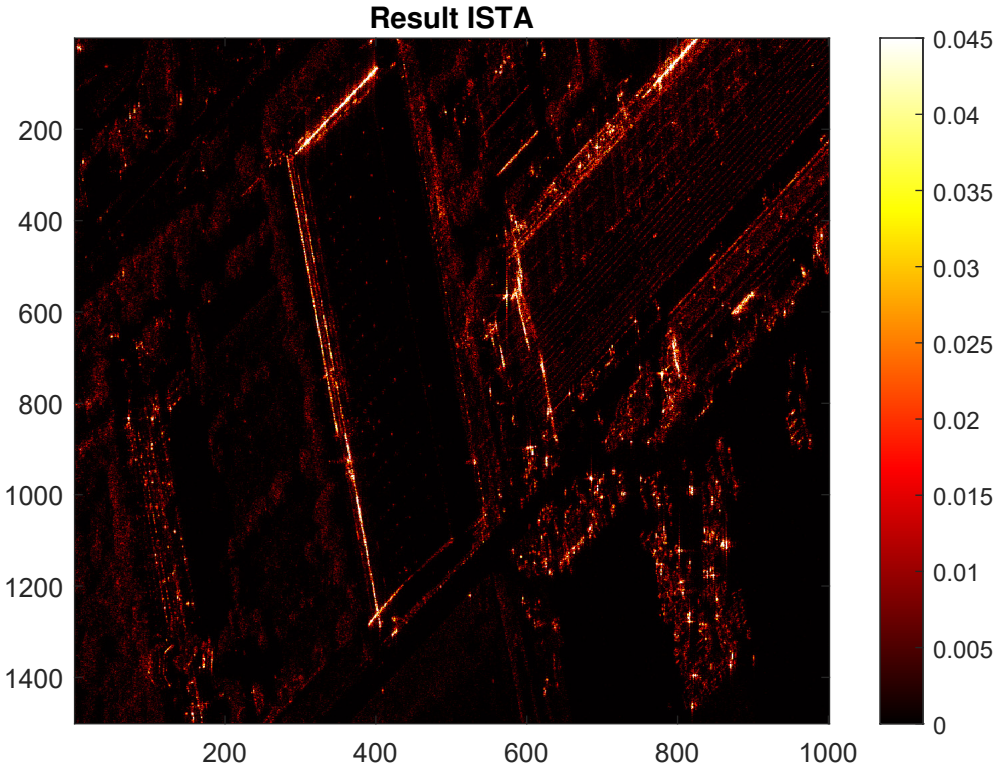

FIGURE 7.20: ISTA result for a gap of 0.2BW.

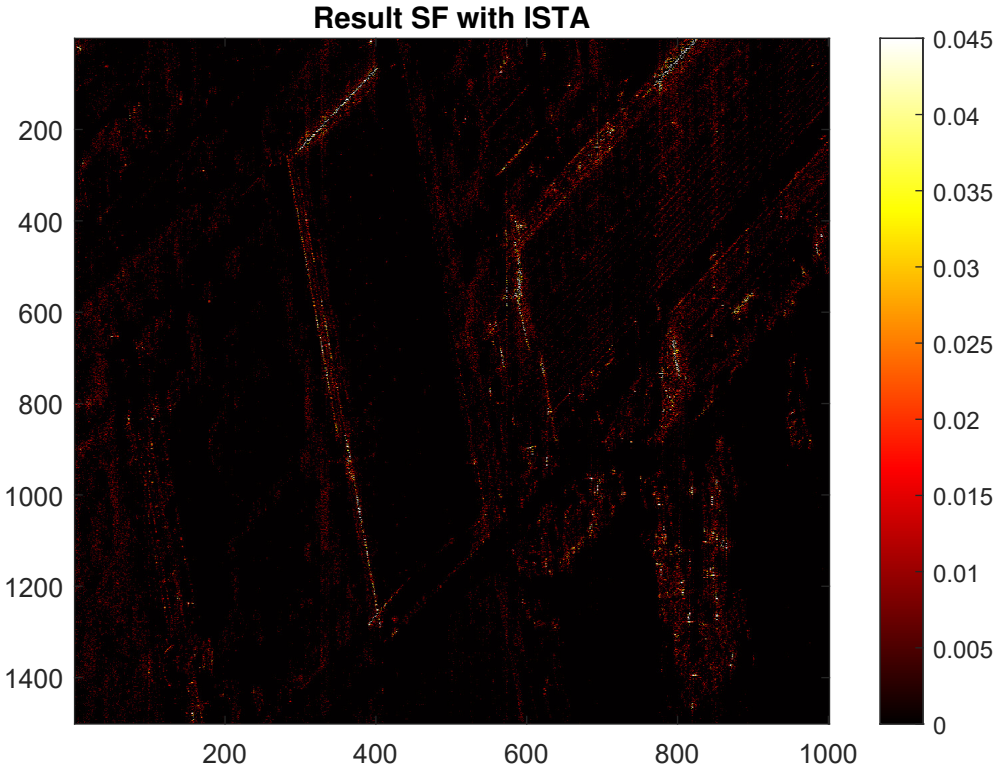

FIGURE 7.21: SF result for a gap of 0.2BW.

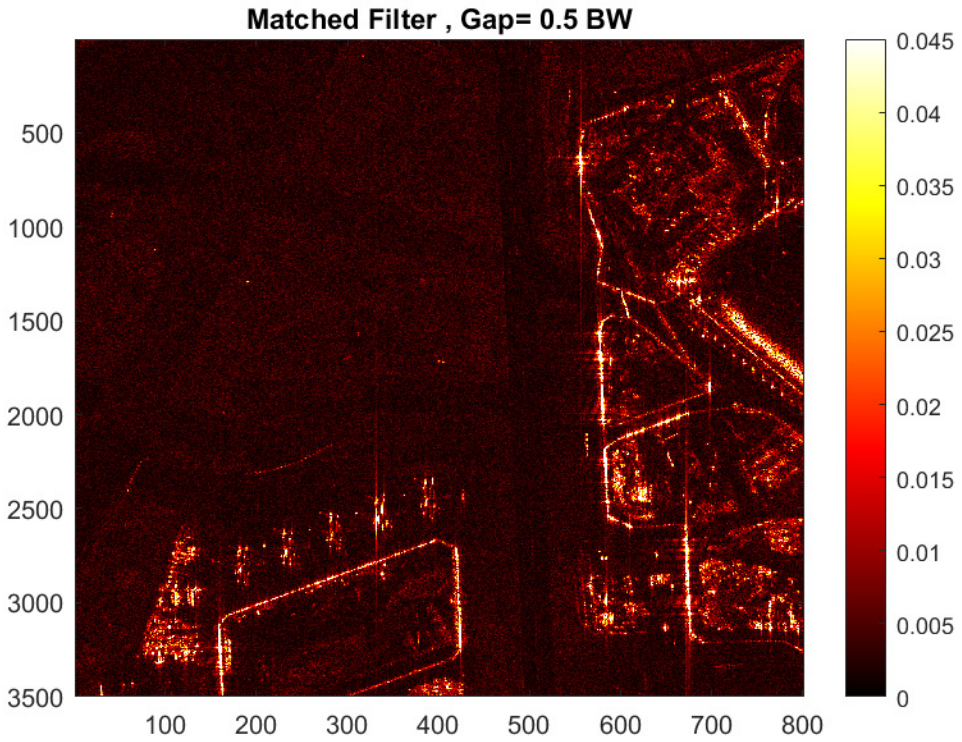

FIGURE 7.22: MF result for a gap of 0.5BW.

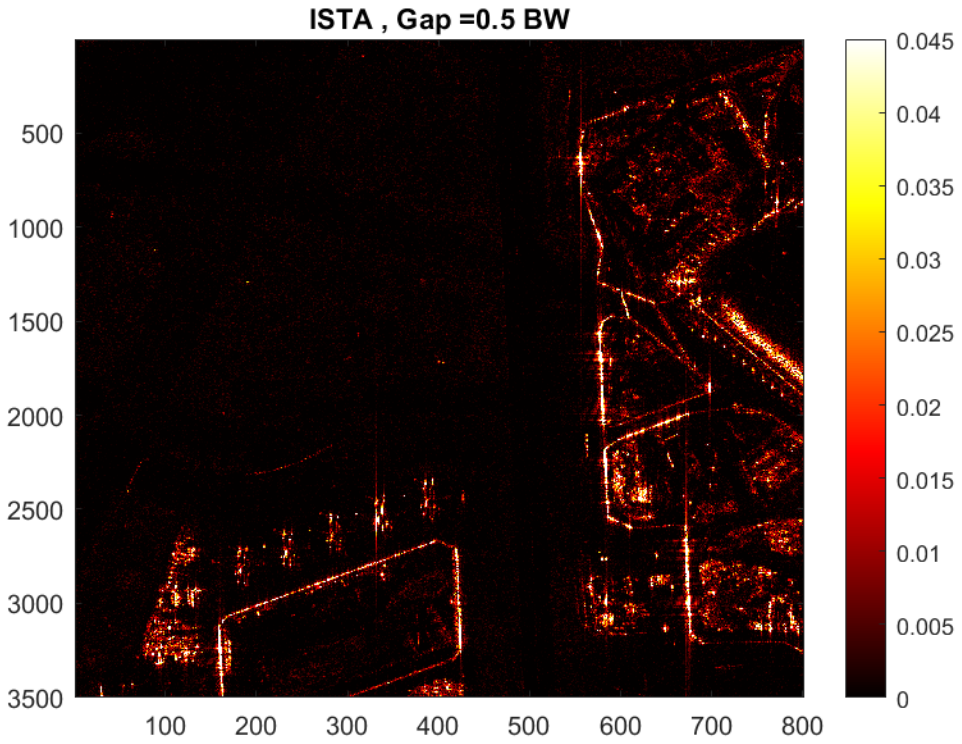

FIGURE 7.23: ISTA result for a gap of 0.5BW.

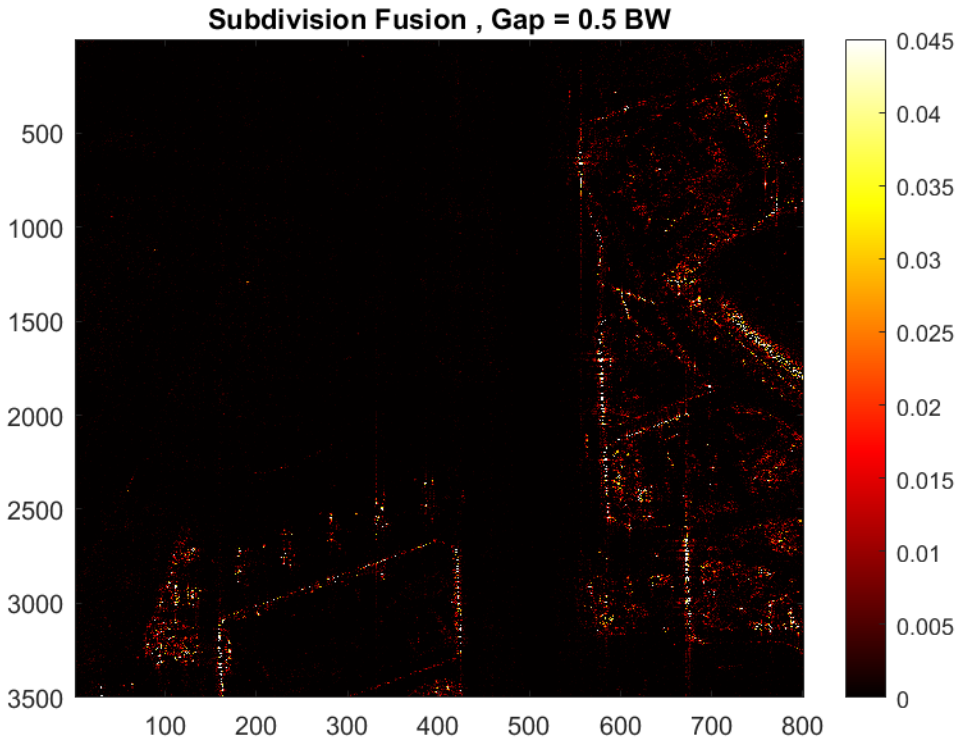

FIGURE 7.24: SF result for a gap of 0.5BW.

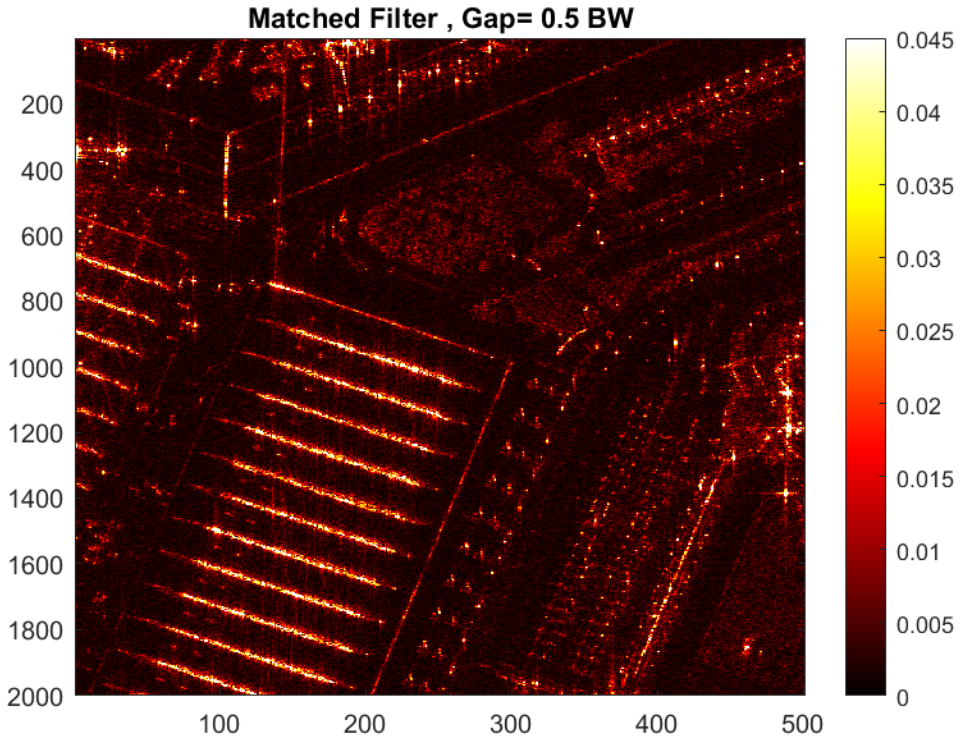

FIGURE 7.25: MF result for a gap of 0.5BW.

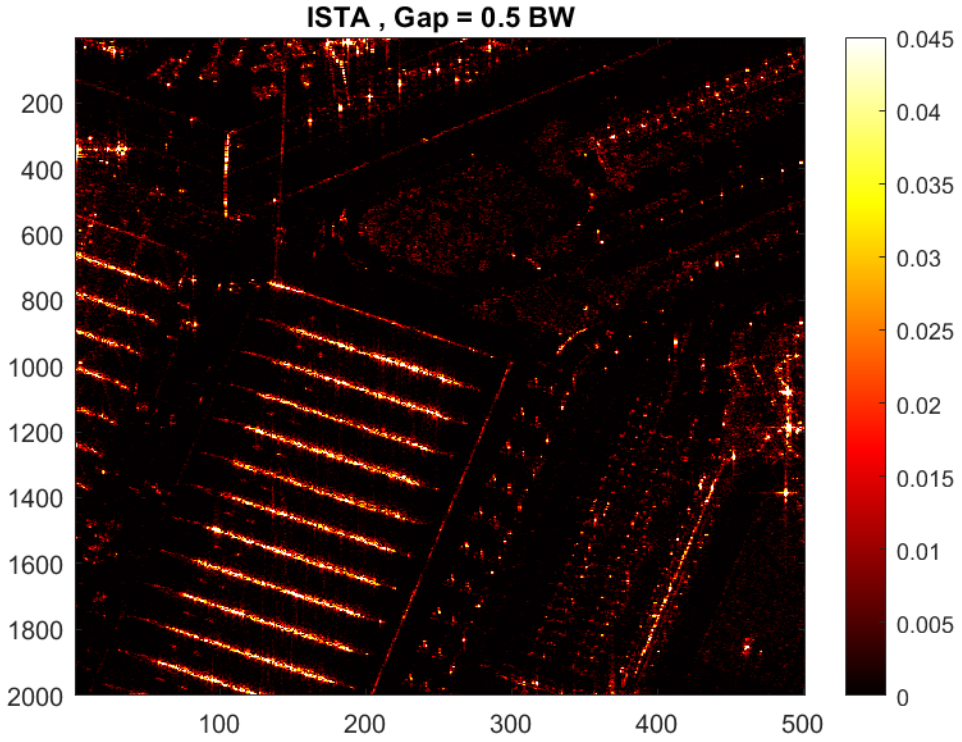

FIGURE 7.26: ISTA result for a gap of 0.5BW.

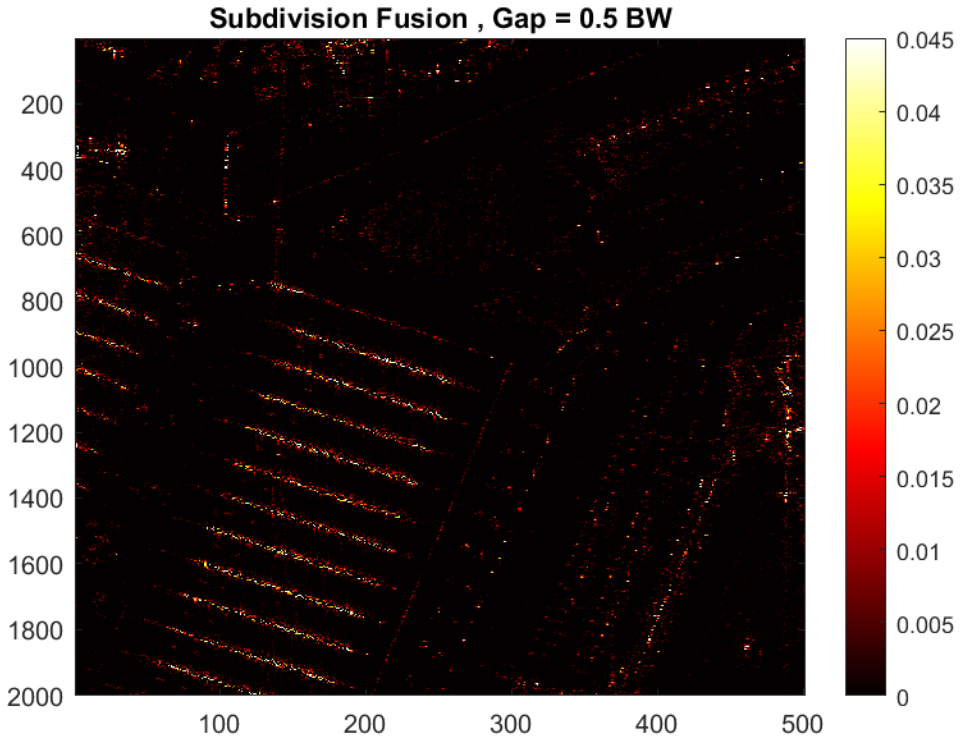

FIGURE 7.27: SF result for a gap of 0.5BW.

thresholding. In other words, $\hat{\mathbf{y}}$ approximates the measurements corresponding to an image having a higher resolution. Then, the difference between the original and approximated measurements, $\mathbf{y} - \hat{\mathbf{y}}$, goes to the SAR processor, and the loop repeats. Following Fig. 7.29, it is evident that the Approximated observation exactly follows the steps of the ISTA algorithm. The only difference is that $\boldsymbol{A}$ now represents a processor instead of a sensing matrix.

In [FXZ+14], the SAR Processor and the Measurement Simulator were described based on the Range-Doppler Algorithm. Here, the processors are described based on Range-Migration (Omega-K) Algorithm, as shown in Fig. 7.28. The key steps are the Fourier transform blocks and the Stolt Interpolation step. The 2D FFT and 2D IFFT blocks represent a domain change and are replaced by the 2D IFFT and 2D FFT respectively. The Stolt interpolation, also known as Stolt Migration, is an important step that causes a transfer in the frequency grid, and is briefly discussed next.

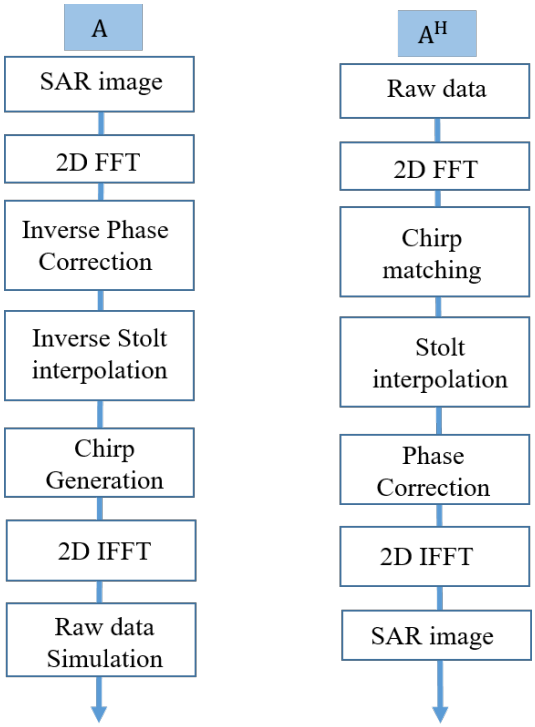

FIGURE 7.28: Approximated Observation Algorithm

Stolt Interpolation and its Inverse Consider the SAR Processor $\boldsymbol{A}^H$. The 2D FFT of the raw data gives a uniformly sampled grid of data in the k_x, k_r domain, where k_x represents the azimuth wavenumber, and k_r represents the slant range wavenumber. The Stolt interpolation is used to transfer the data from the slant range to the ground range wavenumber, k_ρ using

$$k_\rho = \sqrt{4{k_r}^2 - {k_x}^2}, \tag{7.15}$$

as described in Chapter 2. Practically, the interpolation (or grid migration) proceeds as follows. Let the grid corresponding to k_r be known as the original raster, and that corresponding to k_ρ be known as the back-projection raster. The goal is to transfer the values from this original raster to the back-projection raster. For each grid point in the back projection raster, P, a set of nearest neighboring grid points in the original

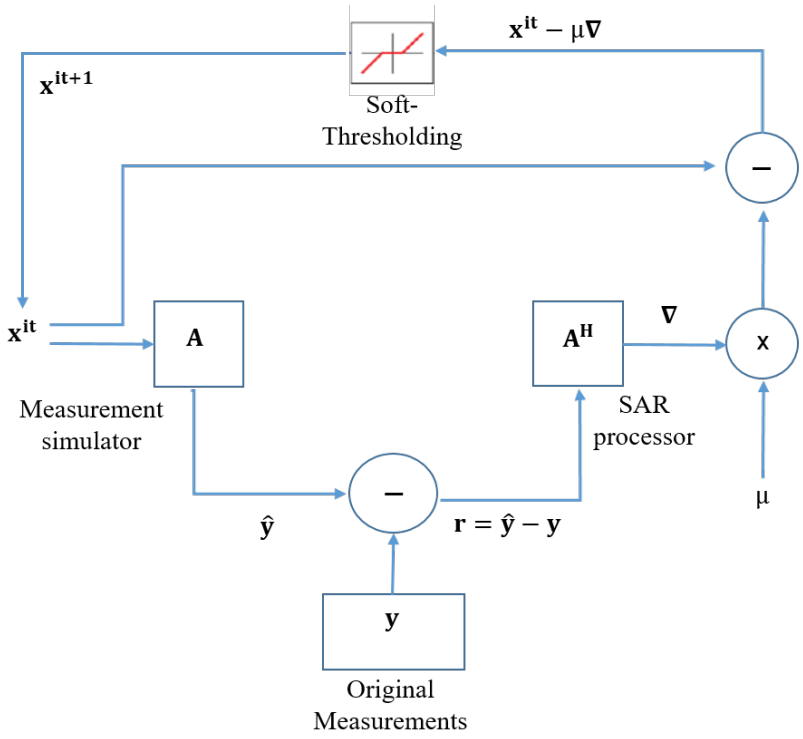

FIGURE 7.29: Approximated Observation with ISTA loop

raster are identified. Sinc coefficients between these points and P are multiplied with the signal values in the original raster and added to get the signal value at P in the new raster.

In the Measurement Simulator $\boldsymbol{A}$, the 2D IFFT gives a uniformly sampled grid of data in the (k_x, k_ρ) domain. The inverse Stolt interpolation is implemented using the exact same steps. Only the original raster and the back projection raster are interchanged, i.e, k_ρ corresponds to the original raster and k_r corresponds to the back-projection raster.

The advantage of this algorithm is that computationally expensive matrix multiplications using the original sensing matrix are avoided. The FFT blocks in the SAR processor and its inverse implementation speed up the algorithm, thereby combining the efficiency of MF based algorithms with the resolution improvement capabilities of CS.

7.2.3 Results

Simulation Results

TABLE 7.4: RMS Contrast values different iterations of AO.

		AO iteration number				
	Gaps	0	1	2	3	4
Scene1	0.3 W	1.9612	2.8728	4.0782	5.1716	6.0547
	0.5 W	1.7173	2.5889	3.8217	5.0056	5.9719
Scene2	0.3 W	1.0393	2.7903	6.2472	10.741	15.8431
	0.5 W	0.9758	2.5896	6.0143	10.5996	15.8307

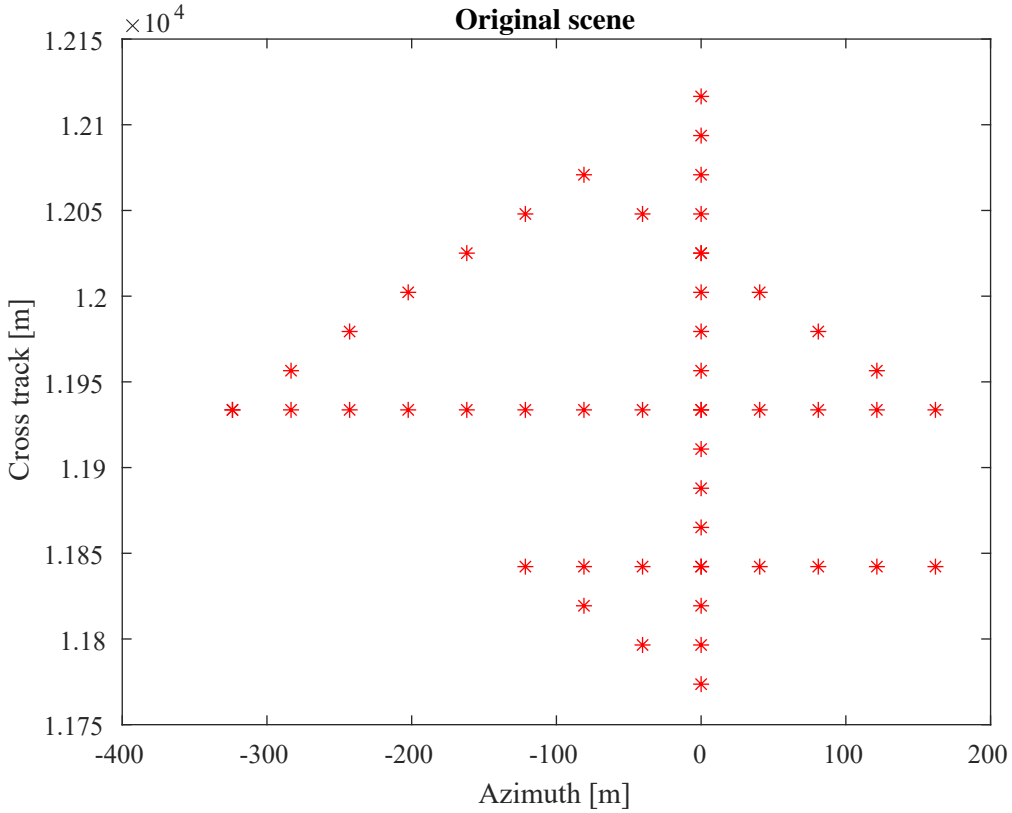

FIGURE 7.30: Synthetic Scene to test AO algorithm.

Fig. 7.30 shows the synthetic scene used to test the algorithm. As before, a continuous gap is introduced along the range frequencies, by removing a fraction of the total number of samples. This 2D gapped-frequency raw data is then given to the SAR processor block, following by the ISTA thresholding and the Inverse SAR processor block. At every iteration, the image $\mathbf{x}^{it}$ is stored. Fig. 7.31 shows the images at successive iterations and their respective RMS contrast values, when a gap having a width of 0.3 of the bandwidth is introduced along the range frequencies. Similarly, Fig. 7.32 shows the resulting images when a gap with a width of 0.5 of the bandwidth is introduced. As expected, the contrast values are better for the smaller gap. The contrast values keep improving with every iteration of the approximated observation algorithm.

Results on SAR Data

As before, 2 parts of a scene from the TerraSAR-X are considered. For each scene, 0.3 and 0.5 of the total number of frequency samples are considered missing along the range frequencies, and results from 4 iterations of the Approximated Observation algorithm are presented. Table. 7.4 shows the RMS contrast values for different iterations of AO for both the scenes. It is observed that with each iteration, the RMS contrast of the result increases, i.e., a sparser SAR image is obtained. The RMS contrast values of the SAR images corresponding to the larger gap are lower than that of the images corresponding to the smaller gap. The AO algorithm performs quite well in both cases, and gives a much sparser SAR image after 4 iterations.

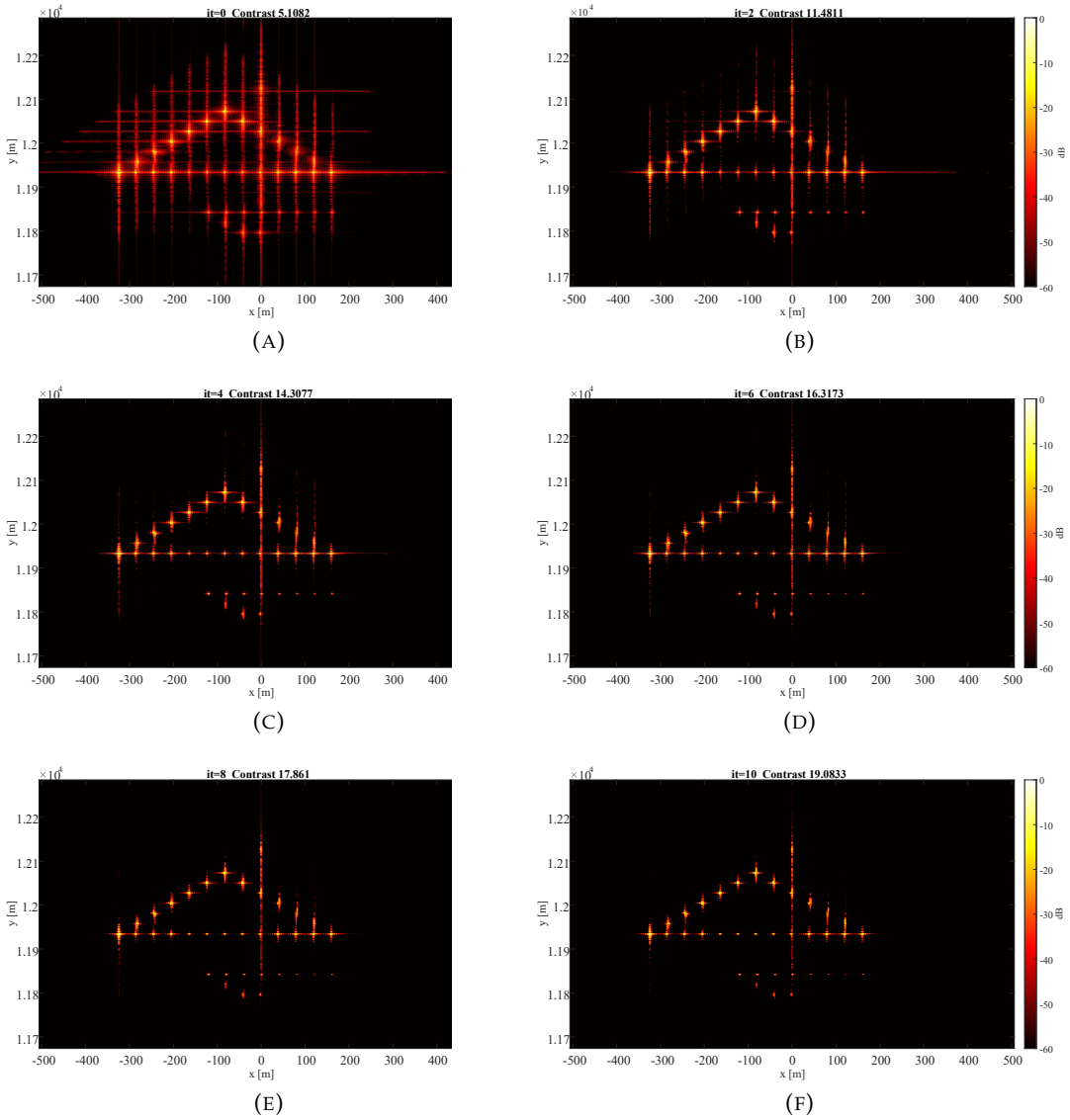

(A) (B) (C) (D) (E) (F)

FIGURE 7.31: Simulation Results from ISTA-AO algorithm for a gap of 0.3BW.

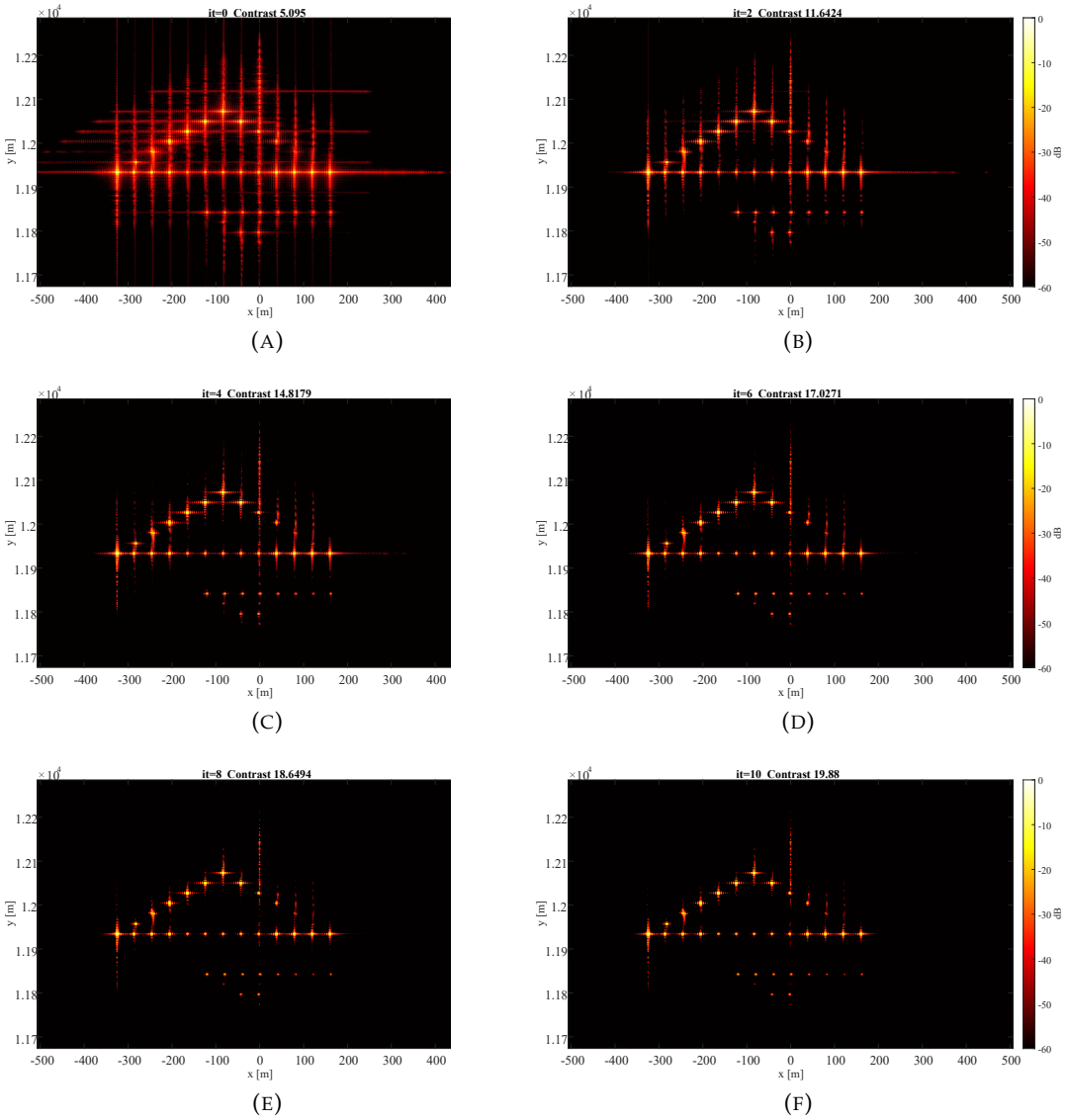

FIGURE 7.32: Simulation Results from ISTA-AO algorithm for a gap of 0.5BW.

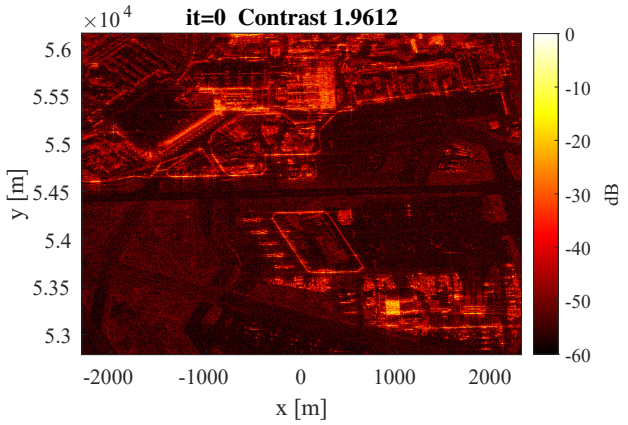

(A)

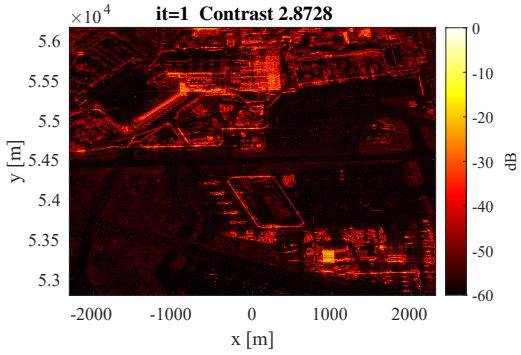

(B)

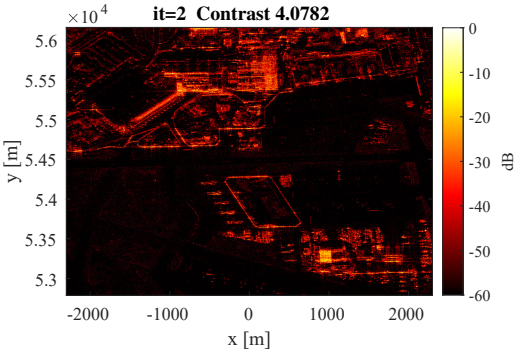

(C)

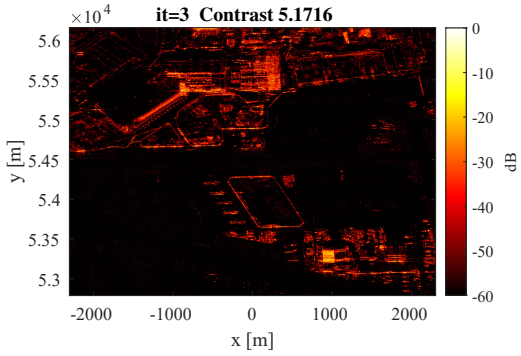

(D)

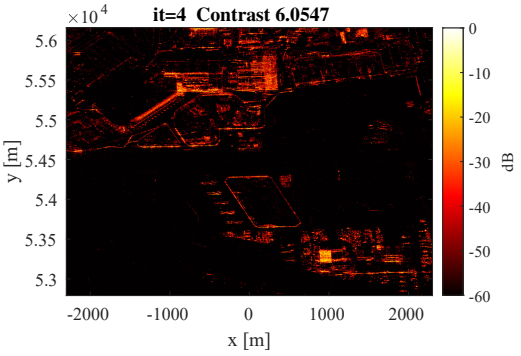

(E)

FIGURE 7.33: SAR Images for iterations of AO algorithm for a gap of 0.3BW-Scene1.

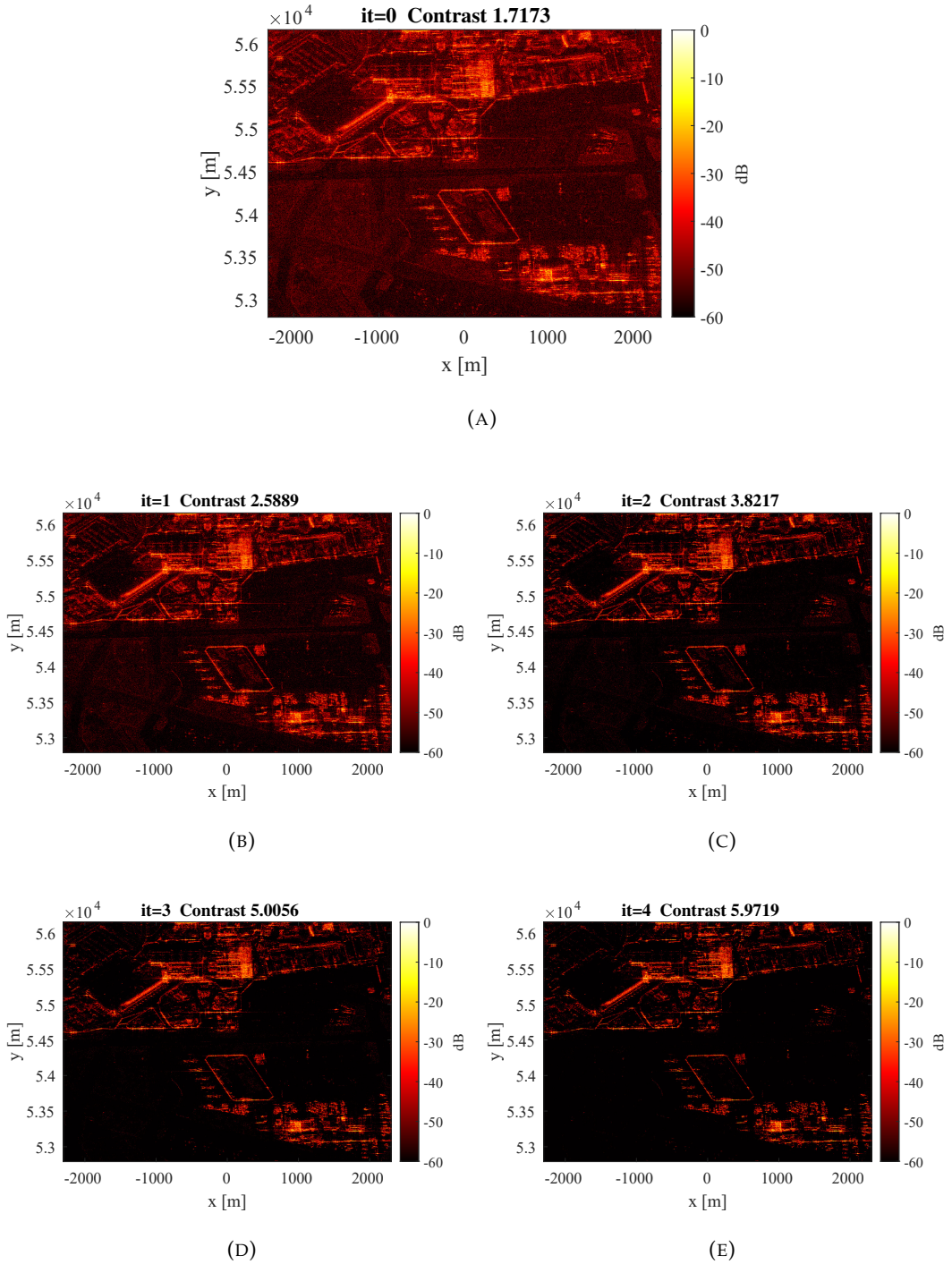

(A)

(B)

(C)

(D)

(E)

FIGURE 7.34: SAR Images for iterations of AO algorithm for a gap of 0.5BW-Scene1.

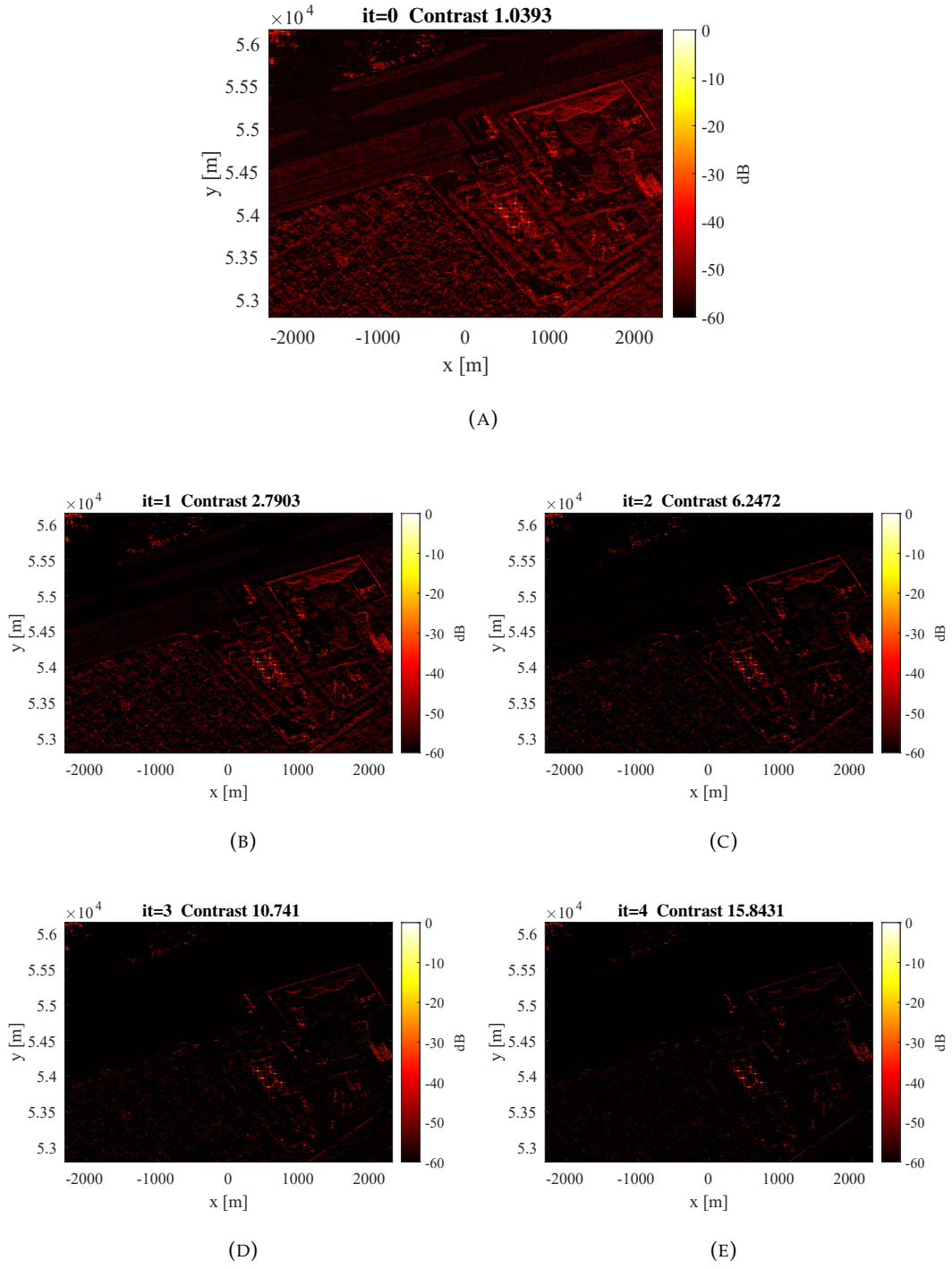

(A)

(B)

(C)

(D)

(E)

FIGURE 7.35: SAR Images for iterations of AO algorithm for a gap of 0.3BW -Scene2.

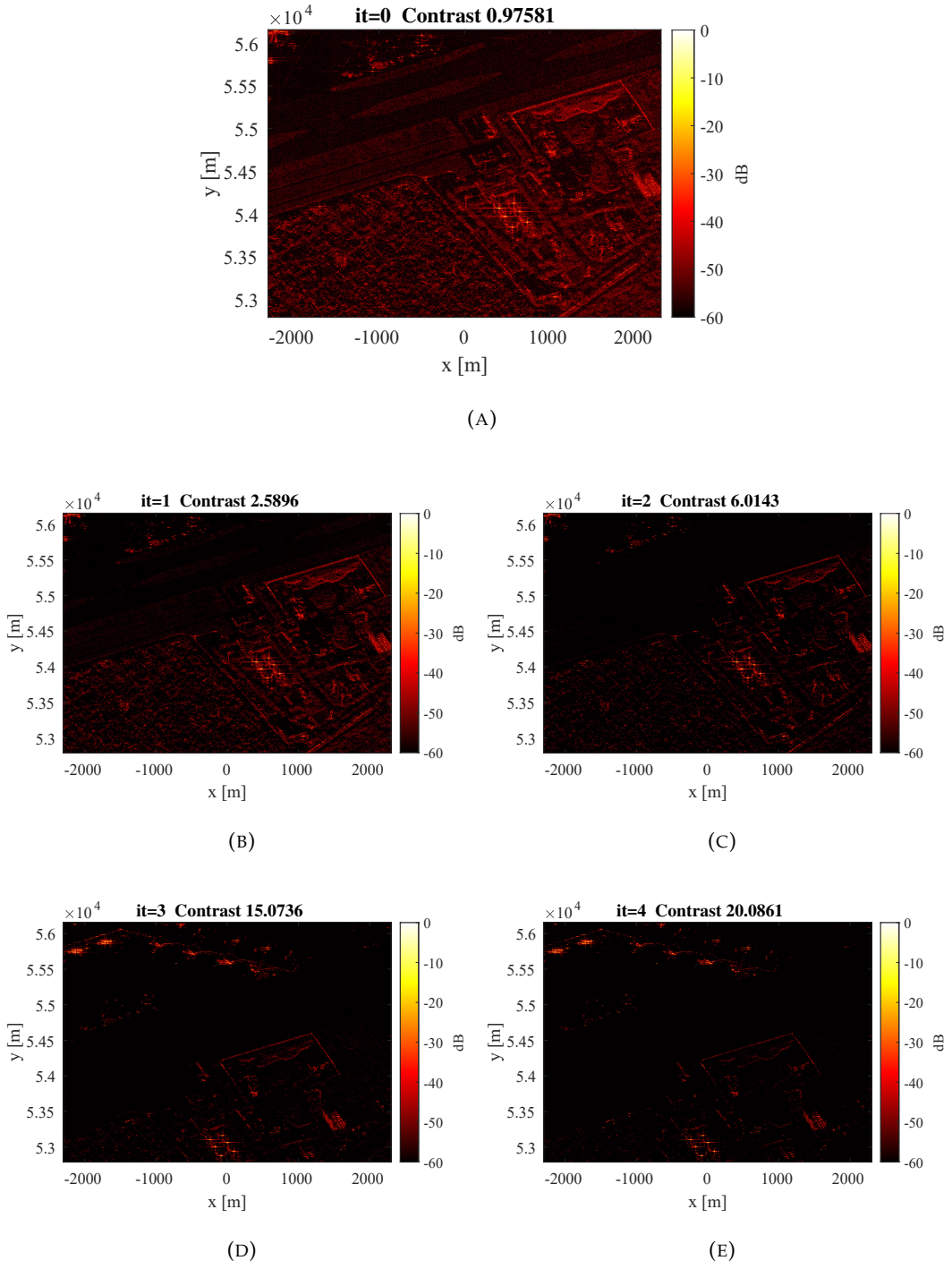

(A)

(B)

(C)

(D)

(E)

FIGURE 7.36: SAR Images for iterations of AO algorithm for a gap of 0.5BW-Scene2.

Chapter 8

Extensions to Time of Flight

8.1 Introduction

The increasing demand for high-resolution remote sensing systems across different parts of the wavelength spectrum was discussed in 1. This chapter provides an extension of the SF idea for multi-target imaging using ToF cameras. The ToF camera [LSH23] is a remote sensing system for 3D scene reconstruction that has gained popularity in the recent years and is being used in a wide range of applications such as vehicle monitoring and obstacle detection in the automotive industry, safe patient monitoring for healthcare, 3D scanning, and human-machine interactions [NKR+15], [KBC13], [IHJ16]. Specifically, the amplitude-modulated continuous wave (AMCW) ToF cameras have had a wide commercial impact due to their small size and high signal-to-noise (SNR) ratio [PBI20].

In AMCW ToF cameras, the intensity of the emitted sinusoidal signal is modulated at one or several frequencies of the order of 10-100 MHz. In an ideal case, this signal is reflected by a sparse number of objects in the scene along the observation direction of each pixel, causing specific time-shifts or phase-shifts in the signal, corresponding to the object depths. The pixels of the ToF camera capture measurements that depend on these shifts in phase, which can then be scaled by the modulation frequency to obtain the object depths.

Typically, ToF systems work on the assumption that each pixel receives a signal reflected by a single object. However, in practice, the signal received by each pixel corresponds to the superposition of signals from multiple scatterers, leading to multipath interference (MPI). As a result, the detected phase shift is distorted, which ultimately leads to an inaccurate depth estimation. Therefore, in ToF systems, depth resolution improvement equates to better multipath interference mitigation. A flurry of research work has appeared on different ways of tackling this MPI problem. Some of these research directions include sensor modification [SLB+21], [HKK+20], [ZWZ+22], [NKR+15], spectral estimation [KBC13], [IHJ16] and deep-learning based approaches [PI21]. Under the umbrella of spectral estimation, research on CS based optimization has shown promising results [BKW+14], [HKB+18], [PBI20]. However, the main challenges have been the computational load due to the size of the sensing matrix, and its high coherence, leading to a failure in the l_1 norm minimization.

The goal is to tackle the MPI problem using a modified subdivision-based nested CS approach. Similar to the radar application discussed earlier in the thesis, the aim is to use multiple submatrices constructed from a single structured sensing matrix. This serves to reduce the coherence as well as the computational load of the optimizations. The depth-regions of interest can then be identified based on the variance of the sub-estimates. Re-applying CS on the combination of these interest areas can

provide better estimates with a much lower computational cost. The performance of the algorithm is tested on a simulated multi-target scene, as well as on real ToF data.

This chapter is structured as follows. Section 8.2 discusses the ToF operation and generation of the measurements at different modulation frequencies. Section 8.3 describes the CS formulation in detail. Section 8.4 discusses the CS specific challenges encountered in ToF MPI mitigation and introduces the subdivision-based CS algorithm to overcome these problems. Section 8.5 provides results based on simulations as well as real data, demonstrating the effectiveness of the proposed method.

8.2 Problem Statement

The focus is placed on a multi-frequency AMCW ToF system and the corresponding mathematical formulation of the frequency-domain sensing model is described as follows. The scene response function in the phase domain, corresponding to the base frequency, is given by

$$e(\phi) = \sum_{k=1}^{P} a_k \delta(\phi - \phi_k) \,, \tag{8.1}$$

where $\delta(\phi - \phi_k)$ is a Dirac delta function centered at ϕ_k, which is the phase shift that the transmitted signal undergoes when following the path $k \in [1, P]$. P represents the number of paths which is assumed to be low or 'sparse'. a_k is the attenuation factor due to non-unit reflectance of target. The received signal at each pixel can then be expressed as a convolution of the transmitted periodic illumination signal $s(\phi)$, and the scene response $e(\phi)$, i.e.,

$$r(\phi) = s(\phi) * e(\phi) \,. \tag{8.2}$$

As described in [HKB+18], the final measurement at each pixel at the end of the exposure time can be modeled as a cross-correlation of $r(\phi)$ with the effective PMD control signal $p_{\mathrm{A-B}}$, which is obtained by subtracting the accumulated charge in the pixel channels A and B, yielding

$$\begin{aligned} m(\phi) &= p_{\mathrm{A-B}} \otimes r(\phi) \\ &= p_{\mathrm{A-B}} \otimes (s * e)\,(\phi) \\ &= \sum_{k=1}^{P} a_k (p_{\mathrm{A-B}} \otimes s)(\phi - \phi_k) \,. \end{aligned} \tag{8.3}$$

The per-path amplitude and the phase terms in (8.3) are the only two parameters of interest and can be determined by $2P + 1$ measurements [HKB+18]. Considering f_0 as the base operating frequency, the data acquisition is carried out for different frequencies given by $f_j = j f_0, j = 1, ..., M$, where j represents the index specifying the frequency in the multi-frequency acquisition mode. If, at every f_j, two measurements are acquired at programmable relative phase shift of $\pi/2$, they can be used to construct the Fourier coefficients of the scene response function. Based on the notation used in the original work [HKB+18], the measurements at phases 0 and $\pi/2$ are represented by $m_j(0)$ and $m_j(\pi/2)$ respectively. The frequency domain signal model

can then be given by

$$\begin{aligned} y(j) &= m_j(0) + i m_j(\pi/2) \\ &= \sum_{k=1}^{P} a_k(\cos(-j\phi_k) - i\sin(-j\phi_k)) \\ &= \sum_{k=1}^{P} a_k e^{(ij\phi_k)} , \end{aligned} \tag{8.4}$$

Expanding the phase term in (8.4) gives

$$\begin{aligned} y(j) &= \sum_{k=1}^{P} a_k e^{(ij(2\pi f_0 t_k))} \\ &= \sum_{k=1}^{P} a_k e^{(i2\pi f_j t_k))} . \end{aligned} \tag{8.5}$$

Thus, (8.5) provides a simplified expression of the measurements at every pixel in terms of discrete time and frequency samples. The aim is to retrieve the terms a_k and t_k, $\forall k \leq P$, that can correctly explain y. The matrix pencil method, a robust variant of Prony's method, provides a way to achieve this goal parametrically, in a closed-form fashion [HS90]. CS based approaches may improve the depth resolution by promoting sparse solutions in a finer grid. However, existing CS algorithms pose certain challenges that are discussed next.

8.3 Compressed Sensing Approach

In practice, the number of objects of interest that reflect the illumination signal is low in comparison to the ambient dimension in time/depth domain, which yields a sparse profile of reflectivity when discretizing along this dimension. Therefore, it is logical to follow a CS-based approach for ToF depth resolution improvement.

A general CS problem is expressed as

$$y = \boldsymbol{A}x + n ,$$

where $y \in \mathbb{C}^m$ contains the measurements in the frequency domain, $\boldsymbol{A} \in \mathbb{C}^{m \times N}$, $m \ll N$, is the sensing matrix, and $x \in \mathbb{C}^N$ is an s-sparse reflectivity vector constructed from the sparse reflectivities of the objects in the scene. n is white Gaussian noise in the measurement y. (8.5) can be expanded into this general CS formulation, giving

$$\underbrace{\begin{bmatrix} y(1) \\ y(2) \\ \vdots \\ y(m) \end{bmatrix}}_{y} = \underbrace{\begin{bmatrix} e^{j2\pi(f_1,t_1)} & \dots & e^{j2\pi(f_1,t_N)} \\ e^{j2\pi(f_2,t_1)} & \dots & e^{j2\pi(f_2,t_N)} \\ \vdots & \ddots & \vdots \\ e^{j2\pi(f_m,t_1)} & \dots & e^{j2\pi(f_m,t_N)} \end{bmatrix}}_{\boldsymbol{A}} \underbrace{\begin{bmatrix} a(1) \\ a(2) \\ \vdots \\ a(N) \end{bmatrix}}_{x} + n . \tag{8.6}$$

The sensing matrix $\boldsymbol{A}$ resembles a horizontal discrete fourier transform (DFT) matrix, oversampled in time. Such a sensing matrix construction aligns with the structured CS approach discussed previously, and is different from the random sensing matrices often assumed to derive recoverability and uniqueness guarantees in CS. The sparse reflectivity vector x consists of the real-valued reflectivities from each

object in the scene. Based on this framework, the solution for x is given by

$$\min \|x\|_1 \;\; s.t. \;\; \|\boldsymbol{A}x - y\|_2 \leq \eta \;, \tag{8.7}$$

where η is the upper bound on the norm of the measurement error, i.e., $\|e\|_2 \leq \eta$. For the ToF application, if the location of the non-zero reflectivities can be determined accurately, the corresponding columns of $\boldsymbol{A}$ can be identified as the active columns, thereby identifying the correct 'times of flight', t_k. These time instances then directly provide the depth information for each object, since $d_k = \frac{ct_k}{2}$. In order to get an improved depth resolution using this CS formulation, the ToF camera must acquire a sufficient number of measurements, m at different modulation frequencies. Theoretically, given a sparsity s and a finely-resolved depth grid of length N, the relation [FR13]

$$m \geq 2s \ln(N)$$

gives the number of multi-frequency measurements required.

8.4 Subdivision-Based Iterative Soft Thresholding Algorithm

The use of popular CS algorithms for the depth resolution improvement in ToF systems poses certain challenges. In the CS formulation described in (8.6), a depth resolution improvement is possible only when CS algorithms support a finely-spaced time (or depth) grid. However, this is challenging due to the following reasons:

1. Given a depth range to be covered, a finely-spaced time grid increases the size of the sensing matrix, leading to a large computational load.

2. With a finely-spaced time grid, the degree of similarity between adjacent columns, which is measured by their normalized inner product, increases, and, as a result, the coherence of the sensing matrix increases, leading to an ill-posed CS problem. In such a scenario, conventional CS methods fail to provide an exact reconstruction of x.

The challenges faced in applying CS algorithms to ToF systems resemble the problems faced in the case of radar imaging. For instance, given a fixed (limited) number of measurements, super-resolution in depth poses a challenge due to the increased coherence of the CS sensing matrix, arising from a finely-spaced depth grid. This is identical to the range super-resolution issue faced in the case of radars. The problem of gapped frequency bands which was explored for radar systems in the previous chapters, might also occur for ToF systems. For example, similar to the FMCW case, multiple multi-frequency ToF systems may be operating in disjoint frequency bands. Ideas from the SF algorithm can be used to exploit the full available bandwidth and fuse the multiple low resolution depth estimates for a better depth resolution.

Both band-gaps and super-resolution may lead to a severely under-determined system of equations that may be solved by a CS-based approach, similar to SF. Here, the focus is placed on improving the depth resolution for ToF systems, given a fixed number of frequency measurements. The band gap problem for ToF has not been examined in this thesis and leaves scope for future work. Based on the similarities discussed, the SF idea from 7 is extended to the ToF case and a modified subdivision-based nested CS algorithm for ToF systems is introduced next.

8.4.1 Subdivision-based Nested CS for ToF Imaging

For obtaining real-valued reflectivities, it suffices to have the frequency domain centered at zero, with measurements obtained at negative frequencies being the complex conjugate of the ones obtained at positive frequencies. Based on this sensing matrix structure, the subdivision-based nested CS algorithm [GAC23] is outlined in Algorithm 6 and is described as follows:

1. Determine the factor $k_{\text{sub}} \leq \frac{N}{m}$ that dictates the ratio between the number of rows and columns of $\boldsymbol{A}$.

2. Divide $\boldsymbol{A}$ into k_{sub} sensing matrices that cover different parts of the time or depth grid, while maintaining a symmetric structure. Let $\boldsymbol{A}_{\text{sub}}$ be a cell array of length k_{sub}, where each cell stores the I^{th} (sub) sensing matrix. The construction of the submatrices can be defined by

$$\begin{aligned} \boldsymbol{A}_{\text{sub}}\{I\}\,(:, J_{\text{sub}} + J - 1) &= \boldsymbol{A}\,(:, (J_{\text{main}} + I - 1) + (J-1)k_{\text{sub}}) \\ \boldsymbol{A}_{\text{sub}}\{I\}\,(:, J_{\text{sub}} - J - 1) &= \boldsymbol{A}\,(:, (J_{\text{main}} - I - 1) - (J-1)k_{\text{sub}})\ , \end{aligned} \tag{8.8}$$

   where, $I = 1, ...k_{\text{sub}}$ and $J = 1, ..., \frac{N}{2k_{\text{sub}}}$. J_{sub} and J_{main} represent the column index for time 0 for the submatrices and the original sensing matrix respectively, i.e., $J_{\text{sub}} = \frac{N}{2k_{\text{sub}}} + 1$, and $J_{\text{sub}} = \frac{N}{2} + 1$. Due to this subdivision, each submatrix $\boldsymbol{A}_{\text{sub}}\{I\}$ has a lower coherence and a k_{sub}-times smaller column dimension compared to $\boldsymbol{A}$, thereby addressing both the challenges previously described.

3. The measurement vector may now be represented as $\mathbf{y} = \boldsymbol{A}_{\text{sub}}\{I\}\mathbf{x}_{\text{sub}}\{I\}$, $I = 1, ..., k_{\text{sub}}$, where $\mathbf{x}_{\text{sub}}$ is a cell array where each cell stores a vector $\mathbf{x}_{\text{sub}}\{I\}$, which is the CS result corresponding to the sub-problem I . These k_{sub} sub-problems can be directly solved using a greedy CS method or basis-pursuit minimization. The standard deviation values of each of the k_{sub} CS results are stored in the vector σ.

4. The columns of each sub-matrix $\boldsymbol{A}_{\text{sub}}\{I\}$ capture a different part of the depth grid. Since the detected scene is sparse, only a few of the vectors in the cell array $\mathbf{x}_{\text{sub}}$ will have sharp peaks representing the on-grid targets for the specific sub-matrices. $\frac{k_{\text{sub}}}{2}$ of these CS results having the highest standard deviation values are selected, since high standard deviation (or variance) corresponds to the CS results with the sharpest peaks. This is represented by the function maxk $\left(\sigma, \frac{k_{\text{sub}}}{2}\right)$ which returns $\frac{k_{\text{sub}}}{2}$ of the highest value elements of σ in the vector σ_1, along with their indices in the vector $\mathbf{idx}$.

5. The fine-grid locations I_{main} corresponding to these peaks are used to construct the final support S. In Algorithm 6, the symbol $\Cup$ represents the union of the fine-grid locations I_{main} that give the support S.

6. The final estimate is given by solving a normal CS problem, as expressed in (8.7), such that

$$\mathbf{x}_{\text{final}} = \text{CS}(\boldsymbol{A}_S, \mathbf{y})\ , \tag{8.9}$$

   where $\boldsymbol{A}_S$ consists of the columns of $\boldsymbol{A}$ identified by the support set S.

Algorithm 6: Subdivision-based Nested CS-3

Data: sensing matrix $\boldsymbol{A}$, measurement vector $\mathbf{y}$
Result: $\mathbf{x}_{\text{final}}$
for $I = 1$ **to** k_{sub} **do**
  for $J = 1$ **to** $\frac{N}{2k_{\text{sub}}}$ **do**
    $\boldsymbol{A}_{\text{sub}}\{I\}(:, J_{\text{sub}} + J - 1) = \boldsymbol{A}(:, (J_{\text{main}} + I - 1) + (J-1)k_{\text{sub}})$;
    $\boldsymbol{A}_{\text{sub}}\{I\}(:, J_{\text{sub}} - J - 1)) = \boldsymbol{A}(:, (J_{\text{main}} - I - 1) - (J-1)k_{\text{sub}})$;
  end
  $\mathbf{x}_{\text{sub}}\{I\} = \text{CS}(\boldsymbol{A}_{\text{sub}}\{I\}, \mathbf{y})$;
  $\sigma(I) = \text{std}(\mathbf{x}_{\text{sub}}\{I\})$;
end
$[\sigma_1, \mathbf{idx}] = \text{maxk}\left(\sigma, \frac{k_{\text{sub}}}{2}\right)$;
for $I = 1$ **to** $\frac{k_{\text{sub}}}{2}$ **do**
  $I_{\text{sub}} = \text{findpeaks}(\mathbf{x}_{\text{sub}}\{\text{idx(I)}\})$;
  $I_{\text{main}} = (J_{\text{main}} + \text{idx(I)} - 1) + k_{\text{sub}}(I_{\text{sub}} - J_{\text{sub}})$;
  $S = \cup I_{\text{main}}$;
end
$\mathbf{x}_{\text{final}} = CS(\boldsymbol{A}_S, \mathbf{y})$;

8.5 Experiments and Results

This section presents the results obtained using the SF algorithm on multi-target ToF data. First the simulation results are discussed and the performance of the SF algorithm is analysed via phase transition diagrams. This is followed by results obtained from a real ToF measurement setup consisting of three targets.

8.5.1 Simulation Results

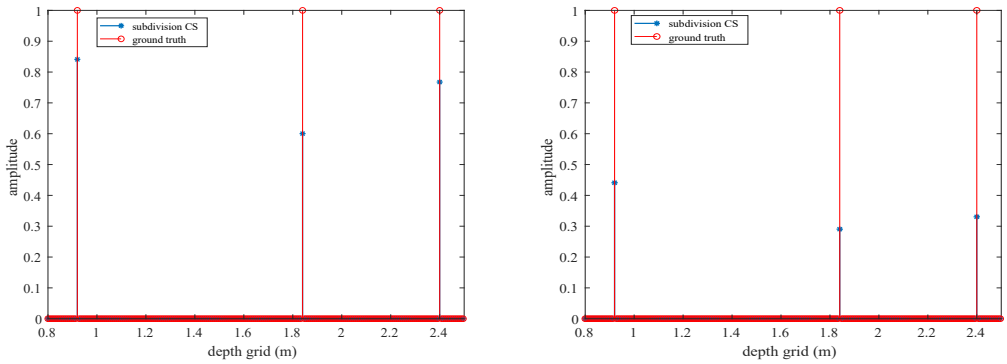

(A) SNR = ∞ (B) SNR = 30

FIGURE 8.1: Synthetic Scene with SNR=∞ and SNR=30 [GAC23].

The performance of the algorithm was tested on synthetic measurements from 3 point targets at depths of 0.92, 1.84 and 2.4 m respectively. Following the parameters of the real measurement setup, 53 frequency samples were considered ranging from 0 to 179.214 MHz, with steps of 3.514 MHz. Since a centered measurement vector is considered, as described in Section 8.4.1, the frequency grid ranges from

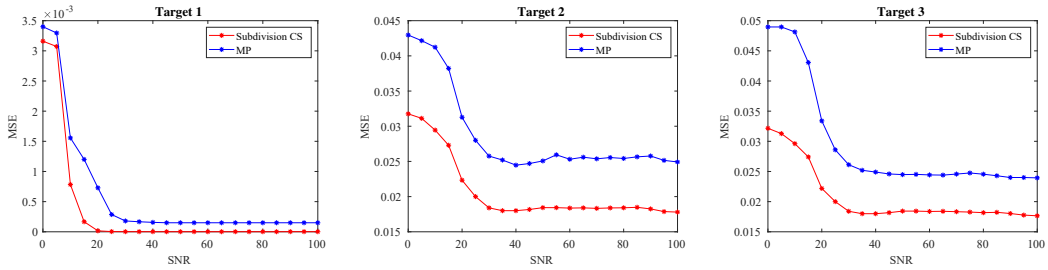

(A) (B) (C)

FIGURE 8.2: SNR vs MSE plots for the 3 synthetic targets [GAC23].

-179.214 MHz to 179.214 MHz. The measurements corresponding to the negative frequencies are complex conjugates of the ones at the positive frequencies. Therefore, the centered measurement vector y consists of 103 measurements. For all simulations, a depth of 3m was considered with a grid resolution of 8mm.

Fig. 8.1 shows the 3 peaks on the depth grid and the reconstruction results from subdivision-based nested CS for SNR= ∞ and SNR=30. As expected, the amplitudes of the detected peaks reduce for the noisy case, however, the positions are detected accurately. Using the Iterative Soft-Thresholding Algorithm (ISTA) as the CS reconstruction method, every instance of the subdivision algorithm has a computation time of 0.004 sec, while the standard ISTA requires 0.13 sec. This improvement greatly affects the computation time, specially when the a large number of ToF pixels are considered.

8.5.2 Performance Analysis

The matrix-pencil method [HS90] has been used as the basis for performance comparison. It was observed that the matrix-pencil method performed better for lower values of the pencil parameter L, $\frac{N}{2} \leq L \leq N$. This agrees with the conditions for a noise-robust pencil method in [HS90]. Fig. 8.2 shows the MSE vs SNR plots for the depth images of the three targets obtained using the subdivision-based nested CS method (in red) and the matrix-pencil method (in blue), for an average of 5 noisy measurements. The error reduces with increase in SNR for both methods and becomes constant at around 20 dB. For all 3 cases, the results from the CS method has a lower error as compared to the matrix-pencil method. This is expected, since the synthetic scene is quite sparse. The small irregularities in the low SNR region arise due to a small number of measurements used for the average.

To analyze the performance of the proposed algorithm for different levels of sparsity and different numbers of measurements in the presence of noise, phase transition diagrams are constructed. In Fig 8.3, $\frac{m}{N}$ denotes the ratio of the number of available measurements to the number of range cells, and $\frac{s}{m}$ denotes the ratio of sparsity to the number of measurements. For each plot, the ratios $\frac{m}{N}$ and $\frac{s}{m}$ are varied from 0.05 to 1 in steps of 0.05 and for every point $\left(\frac{m}{N}, \frac{s}{m}\right)$, 20 iterations of the proposed method are executed. The success or failure of each iteration is determined by calculating the averaged mean-squared error between the ground truth and the reconstruction results. An error of 0.001 or less is considered a success. The averaged rate of success is then shown in the corresponding position in the phase transition diagram. Since the sensing matrix is always wide $(N \gg m)$, the number of columns (N) considered for the phase transition diagrams is kept fixed and the number of

TABLE 8.1: Target position estimates from the Subdivision-based CS method and the matrix pencil method.

	Targets		
Methods	T1 (m)	T2 (m)	T3 (m)
Ground Truth	0.87	1.87	2.408
Matrix Pencil	0.38	1	3.1-3.18
Subdivision-based CS	0.86	1.937	2.35-2.4

available measurements (m) is increased till $m = N$ or $\frac{m}{N} = 1$. Fig 8.3 shows the phase transition plots for the nested CS method for SNR = ∞, 80, 40, and 20 dB.

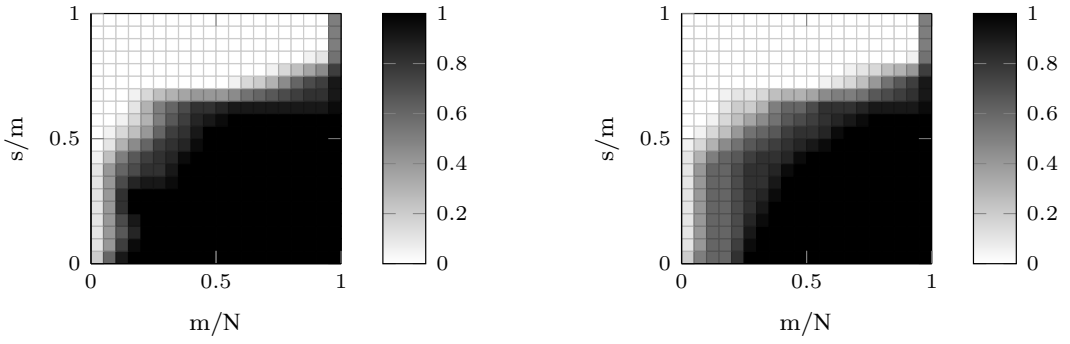

(A) SNR = ∞ (B) SNR = 80

(C) SNR = 40 (D) SNR = 20

FIGURE 8.3: Phase transition diagrams. Black corresponds to 100% empirical success probability. White corresponds to 0% success probability [GAC23].

8.5.3 Results on Multi-Target Real ToF Data

This section discusses the results obtained using real ToF data. The measurements were carried out at the Center for Sensor Systems (ZESS). The muti-frequency ToF data was acquired using the ToF camera of PMD Module 167-C39. The experimental setup, shown in Fig. 8.4, consists of 3 targets—a glossy translucent target (T1) at 0.87 m, a diffusive translucent target (T2) at 1.87 m, and an opaque white placard target (T3) at 2.408 m depth. All these targets are plane sheets placed orthogonal to the direction of observation of the camera, by means of custom frames on optical rail conveyors. Identical to the simulation parameters, 53 frequency samples were

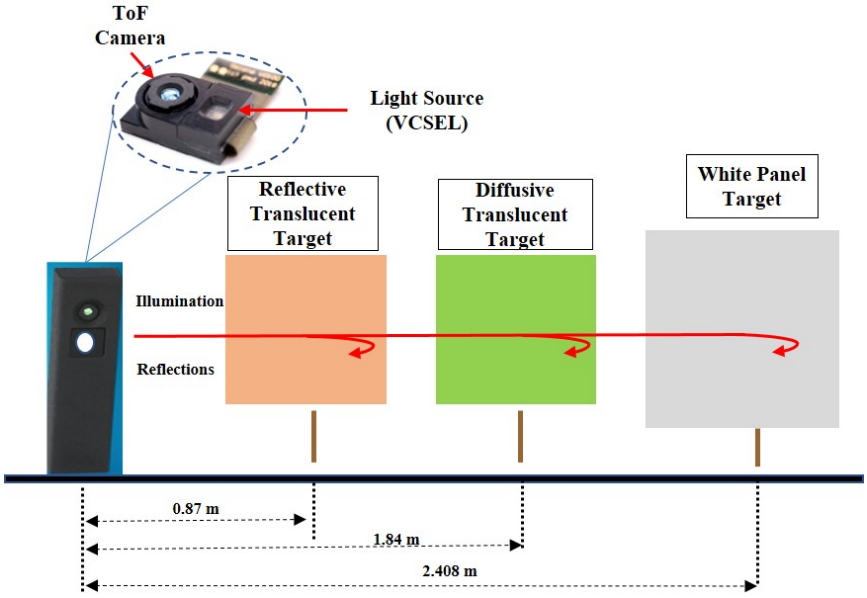

FIGURE 8.4: Experimental Setup

considered ranging from 0 to 179.214 MHz, with steps of 3.514 MHz, and the final estimation was obtained for a depth resolution of 8mm.

Fig. 8.5(a) shows the depth images obtained using the subdivision-based CS (top) and the matrix pencil method (bottom) on real measurements. Fig. 8.5(b) presents the 3D plots of the depth images obtained using subdivision-based CS. Table. 8.1 shows the estimated depths of each target from both methods. Since the position in depth is decided by the location of the amplitude peaks, the sparsity-inducing methods perform better as they are capable of robustly identifying the location of the prominent data peaks in noisy environments. The matrix pencil method shows much higher sensitivity to noise and fails with real data. Specially in the case of T3, the same amplitude was detected for a large number of inaccurate points in the depth grid, leading to an incorrect estimate. Overall, the estimation error of the CS based method is approximately an order of magnitude lower than that of the matrix pencil method adopted in prior works to solve the MPI problem.

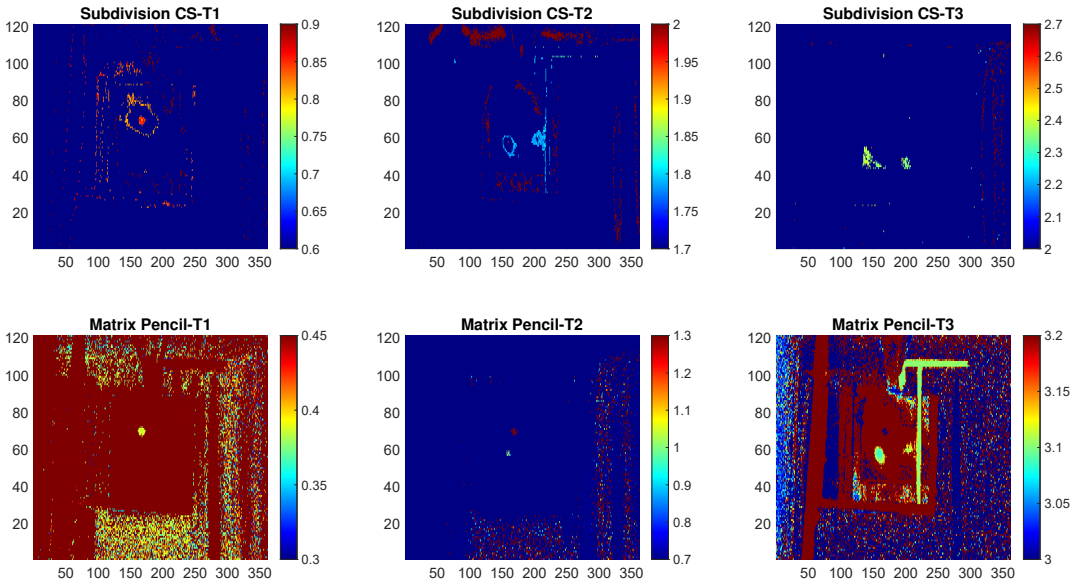

(A) Depth images from Subdivsion-based CS (top) and Matrix Pencil (bottom). The colorbars represent the depth in m.

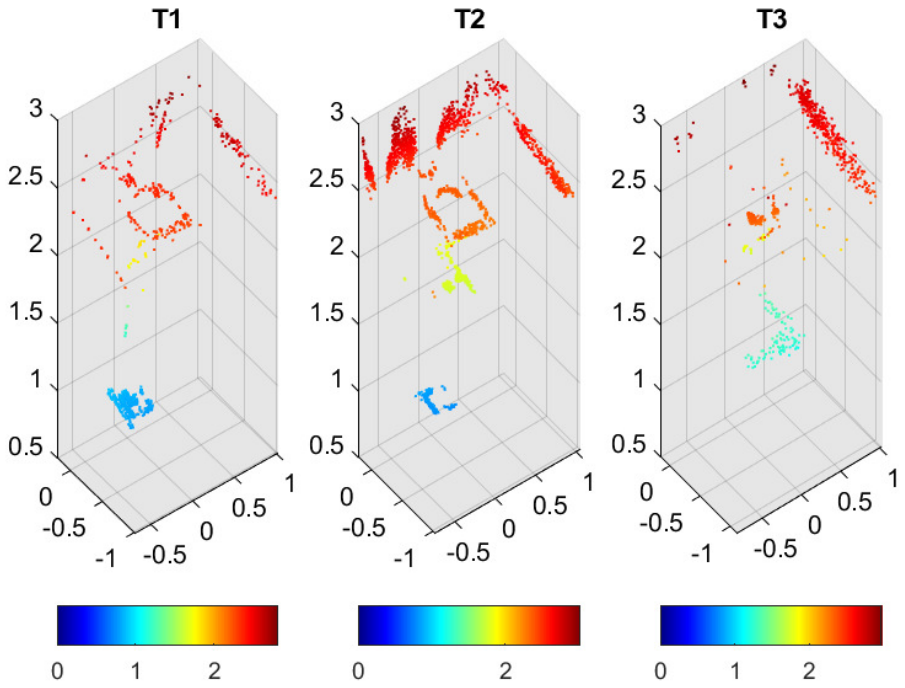

(B) 3D point clouds from Subdivsion-based CS. All axes are in m.

FIGURE 8.5: Depth Image results from Subdivision-based CS and Matrix Pencil methods [GAC23].

Chapter 9

Conclusion and Future Work

9.1 Summary and Conclusions

This thesis explores different techniques for applying CS methods to the gapped-band problem. It aims to adapt the CS sensing model to the imaging modality (radar systems, ToF cameras) under consideration, and addresses the most common challenges faced while applying CS to such modalities. While the thesis mainly focuses on CS applied to gapped-band radar data, an extension to ToF cameras is also discussed, proving the adaptability of the proposed ideas.

Chapters 2 and 3 review the fundamentals from radar and CS. In the former, the working principle of a general radar system is discussed followed by the most commonly used radar waveforms. The chirp waveform and the concept of stretch processing are introduced, and they reappear as important components of the signal models described in later chapters. The basic concepts of SAR and ISAR imaging are also discussed.

The latter reviews the important aspects of Compressed Sensing Theory. It motivates the need for CS, and discusses the key aspects that make up a CS problem, namely, the signal and the sensing matrix. It presents the metrics that determine the quality of a CS sensing matrix and introduces the idea of coherence, which becomes a significant component for one of the proposed algorithms in Chapter 7. It also highlights the main classes of existing CS algorithms.

Chapter 4 acts as an important link between Chapters 2 and 3. The radar waveforms introduced in 2 are used in the CS framework discussed in 3, giving the general CS models for radar systems based on different waveforms.

Chapter 5 highlights the existing literature in missing data recovery. It identifies the research done by 3 different communities to solve different versions of the missing data problem, and discusses the common challenges and pitfalls of the existing works.

Chapter 6 consolidates the findings of Chapter 5 into a compact problem statement that the thesis addresses. The need for adaptive CS algorithms to tackle the gapped-band problem is motivated. The second half of this chapter mathematically defines the gapped band problem based on the CS models described in Chapter 4.

Chapter 7 consists of the main contributions of the thesis. It discusses the two proposed algorithms, namely the Subdivision-Fusion algorithm, and the Approximated Observation algorithm. The subdivision method divides the structured CS sensing matrix into smaller sub-matrices, in order to reduce the coherence value as well as the computational load. From the results it can be concluded that, while the traditional CS methods do not completely fail, the subdivision-based CS provides much sharper peaks, specially for wider band gaps. The results from FMCW radar and SAR data are found to be consistent with the simulation results. The Approximated Observation method tackles the same issues by replacing the sensing

matrix with matched-filter based processors. The goal is to replace the sensing matrix multiplications that present a high computational load with fast FFTs. It can be concluded from the results that the resolution improves with each iteration of the Approximated Observation algorithm and the method works quite well even in the presence of a continuous gap.

Chapter 8 discusses an extension of the Subdivision-Fusion algorithm for multi-path detection using ToF cameras. From the results, it can be concluded that CS based methods provide much better target estimation in noisy environments compared to the Matrix Pencil method, which has been proposed in the literature to solve the multi-path interference problem parametrically.

9.2 Future work

Different column selection scheme in the SF algorithm :

The Subdivision-Fusion algorithm in Chapter 2 discussed the construction of submatrices by selecting every k_{sub} column from the original structured sensing matrix. This makes sense since the columns correspond to the range cells and such a selection reduces the coherence. The concept of subdivision maybe extended to a random CS matrix. In this case, subdivision based on every k_{sub} column no longer makes sense. For a submatrix, the first column selected can be the first available column in the original sensing matrix. Then, the next best column may be chosen from the next group of k_{sub} columns, such that it leads to a submatrix with a lower coherence value. It is to be noted that such a process involves no optimization, and thus is free of the computational load posed by an optimization algorithm that scans all columns of the original sensing matrix. Since all columns of the original sensing matrix at not being considered for every column selection, the time taken should be managable. The drawback of such an approach would be that the last submatrix has to be constructed with the remaining columns and therefore, the coherence might be arbitrarily bad. Further research in this direction is needed to overcome such a disadvantage.

Hybrid CS methods:

The concept of Algorithm Unrolling was briefly discussed in Chapter 5, and has become quite popular in recent years. Many papers exist on algorithm unrolling for optical images. However, the work done for SAR or radar systems is quite limited. [GDE22] explored a hybrid algorithm combining unrolled ISTA and Approximated Observation, in an effort to leverage the benefits from both approaches. However, a detailed comparison of performance needs to be made to conclude any significant benefits of such a combination. In particular, the progression of the weights learned in the deep network and its effects on the ISTA regularization parameter may be explored. The idea of combining domain knowledge with advantages of deep learning has become increasingly popular in the recent years and it is an interesting direction to explore in the future.

CS on Hardware:

CS based hardware design for signal acquisition has gained popularity in the past few years [CME18], [ME11]. [YHK+19] provides an interesting discussion on CS at the hardware level. Recently, there has been a push towards ultra-wideband (UWB)

enabled chips that can be embedded in smartphones and smartwatches, to provide very precise localization. This is another step towards achieving multi-appliance connectivity and Internet-of-Things. With the exponential increase in appliances and a crowded spectrum, the electronics behind UWB need to be adapted to work with limited samples, reaffirming the relevance of CS based hardware design. Focusing on UWB receiver design, [YLP+09] provides an electronics framework that uses CS. Implementation of the CS ideas proposed in this thesis within such a framework might be an important future direction. For instance in [YLP+09], the tap delays correspond to the delays in fast time, and the distributed amplifiers (DA) and analog-to-digital converters (ADCs) are used to construct the CS problem. This resembles the proposed subdivision scheme in many ways. The gain coefficients of the DA may be modelled using the elements of the structured CS matrices proposed in this thesis. The links between the DAs and ADCs may also be modified, leading to a number of smaller CS problems instead of a single CS problem. Such hardware implementations of CS bridge the gap between the theoretical algorithms and practical System(s)-on-Chip (SoCs) technology, and is an important research area to explore.

Appendix A

A.1 PSP derivation for Gapped Chirp

The integral part from (6.5) is $\phi(t,f) = \int_{\frac{-T_i}{2}}^{\frac{T_i}{2}} e^{j\pi\left(\alpha t^2 - 2(f-\alpha\tau_i)t\right)} dt$. Writing only the real part of the exponential and its first and second derivative, we get

$$\begin{aligned}
\phi(t,f) &= \pi\left(\alpha t^2 - 2\left(f-\alpha\tau_i\right)t\right) \ , \\
\phi'(t,f) &= \pi(2\alpha t - 2(f-\alpha\tau_i)) \ , \\
\phi''(t,f) &= \pi(2\alpha) \ .
\end{aligned}$$

Equating first derivative to 0, we get

$$t_0 = \frac{f}{\alpha} - \tau_i \ .$$

Then,

$$\phi(t_0,f) = \pi\left(-\frac{f^2}{\alpha} + 2f\tau_i - \alpha\tau_i^2\right) \ .$$

So, the PSP solution to the integral is,

$$\begin{aligned}
X(f) &= \sqrt{-\frac{2\pi}{\phi''(t,f)}} e^{-j\pi/4} e^{j\phi(t_0,f)} \\
&= \sqrt{-\frac{1}{\alpha}} e^{-j\pi/4} e^{j2\pi\left(-\frac{f^2}{2\alpha} + f\tau_i - \frac{\alpha\tau_i^2}{2}\right)} \ .
\end{aligned}$$

A.2 Derivation of the beat frequency signal for FMCW signal model

The transmitted LFM signal is given by

$$y(t) = e^{j(2\pi f_{Tx}t + \pi\alpha t^2)} \text{rect}\left(\frac{t}{T_p}\right) \ ,$$

where f_{Tx} is the transmit frequency (or center frequency) of the signal, α is the slope, and T_p is the pulse duration.

The received signal is a time delayed version of the transmitted signal, given by

$$y(t-\tau_j) = e^{j(2\pi f_{\text{Tx}}(t-\tau_j) + \pi\alpha(t-\tau_j)^2)} \text{rect}\left(\frac{t-\tau_j}{T_p}\right) \ ,$$

where τ_j is the time delay of the signal backscattered from a target at the j^{th} index of the delay grid.

The ramp signal is given by

$$r\left(t\right) = e^{j\left(2\pi f_{\mathrm{Tx}}(t-t_0)+\pi\alpha(t-t_0)^2\right)}\mathrm{rect}\left(\frac{t-t_0}{T_p}\right) ,$$

where, t_0 is the time delay corresponding to the Central Reference Point (CRP) [R14, p.277].

Stretch processing of the received LFM signal gives the beat frequency signal,

$$\begin{aligned} y_{\mathrm{IF}}^{\tau_j}(t) &= \mathrm{r}^*\left(t\right)\ y\left(t-\tau_j\right) \\ &= e^{j\left(2\pi f_{\mathrm{Tx}}\left(t-\tau_j\right)+\pi\alpha\left(t-\tau_j\right)^2-2\pi f_{\mathrm{Tx}}(t-t_0)-\pi\alpha(t-t_0)^2\right)}\mathrm{rect})\left(\frac{t-\tau_j}{T_p}\right)\mathrm{rect}\left(\frac{t-t_0}{T_p}\right) . \end{aligned}$$

Simplifying this equation gives the final expression for the beat frequency signal,

$$y_{\mathrm{IF}}^{\tau_j}(t) = e^{j\left(2\pi f_{\mathrm{Tx}}\left(t_0-\tau_j\right)+\pi\alpha\left(\tau_j^2-t_0^2\right)-2\pi\alpha t\left(\tau_j-t_0\right)\right)}\mathrm{rect}\left(\frac{t-\tau_j}{T_p}\right)\mathrm{rect}\left(\frac{t-t_0}{T_p}\right) .$$

Bibliography

[A94] Hugh G. J. Aitken. "Allocating the Spectrum: The Origins of Radio Regulation". In: *Technology and Culture* 35.4 (1994), pp. 686–716. ISSN: 0040165X, 10973729. URL: http://www.jstor.org/stable/3106503 (visited on 08/28/2023).

[ABB+23] Pia Addabbo, Mario Luca Bernardi, Filippo Biondi, Marta Cimitile, Carmine Clemente, Nicomino Fiscante, Gaetano Giunta, Danilo Orlando, and Linjie Yan. "Super-Resolution of Synthetic Aperture Radar Complex Data by Deep-Learning". In: *IEEE Access* 11 (2023), pp. 23647–23658. DOI: 10.1109/ACCESS.2023.3251565.

[ABL18] Roza. Aceska, Jean-Luc Bouchot, and Shidong Li. "Fusion frames and distributed sparsity". In: *Frames and Harmonic Analysis*. Ed. by Yeonhyang Kim, Sivaram K. Narayan, and Gabriel Picioroaga. Vol. 706. Contemporary Mathematics Ser. Providence: American Mathematical Society, 2018, pp. 47–61. ISBN: 978-1-4704-3619-3. DOI: 10.1090/conm/706/14220.

[AHS+09] Lorne Applebaum, Stephen D. Howard, Stephen Searle, and Robert Calderbank. "Chirp sensing codes: Deterministic compressed sensing measurements for fast recovery". In: *Applied and Computational Harmonic Analysis* 26.2 (2009), pp. 283–290. ISSN: 10635203. DOI: 10.1016/j.acha.2008.08.002.

[ASE23] Tushar Agarwal, Nithin Sugavanam, and Emre Ertin. "MrSARP: A Hierarchical Deep Generative Prior for SAR Image Super-resolution". In: *2023 IEEE Radar Conference (RadarConf23)*. 2023, pp. 1–6. DOI: 10.1109/RadarConf2351548.2023.10149659.

[BF08] E. van den Berg and M. P. Friedlander. "Probing the Pareto frontier for basis pursuit solutions". In: *SIAM Journal on Scientific Computing* 31.2 (2008), pp. 890–912. DOI: 10.1137/080714488. URL: http://link.aip.org/link/?SCE/31/890.

[BF19] E. van den Berg and M. P. Friedlander. *SPGL1: A solver for large-scale sparse reconstruction*. https://friedlander.io/spgl1. Dec. 2019.

[BKW+14] Ayush Bhandari, Achuta Kadambi, Refael Whyte, Christopher Barsi, Micha Feigin, Adrian Dorrington, and Ramesh Raskar. "Resolving multipath interference in time-of-flight imaging via modulation frequency diversity and sparse regularization". In: *Optics letters* 39.6 (2014), pp. 1705–1708.

[BT09] Amir Beck and Marc Teboulle. "A Fast Iterative Shrinkage-Thresholding Algorithm for Linear Inverse Problems". In: *SIAM Journal on Imaging Sciences* 2.1 (2009), pp. 183–202. DOI: 10.1137/080716542. eprint: https://doi.org/10.1137/080716542. URL: https://doi.org/10.1137/080716542.

[BT23] Andreas Bathelt and Ruben Thill. "Radar-sensing based on non-contiguous OFDM signals using Compressed Sensing". In: *2023 20th European Radar Conference (EuRAD)*. 2023, pp. 403–406. DOI: 10.23919/EuRAD58043.2023.10289155.

[BZ21] Shengqin Bian and Lixin Zhang. "Overview of Match Pursuit Algorithms and Application Comparison in Image Reconstruction". In: *2021 IEEE Asia-Pacific Conference on Image Processing, Electronics and Computers (IPEC)*. 2021, pp. 216–221. DOI: 10.1109/IPEC51340.2021.9421295.

[CDS01] Scott Shaobing Chen, David L Donoho, and Michael A Saunders. "Atomic decomposition by basis pursuit". In: *SIAM review* 43.1 (2001), pp. 129–159.

[CDS98] Scott Shaobing Chen, David L. Donoho, and Michael A. Saunders. "Atomic Decomposition by Basis Pursuit". In: *SIAM Journal on Scientific Computing* 20.1 (1998), pp. 33–61. DOI: 10.1137/S1064827596304010. eprint: https://doi.org/10.1137/S1064827596304010. URL: https://doi.org/10.1137/S1064827596304010.

[CKL08] Peter G. Casazza, Gitta Kutyniok, and Shidong Li. "Fusion frames and distributed processing". In: *Applied and Computational Harmonic Analysis* 25.1 (2008), pp. 114–132. ISSN: 10635203. DOI: 10.1016/j.acha.2007.10.001.

[CME18] Deborah Cohen, Kumar Vijay Mishra, and Yonina C. Eldar. "Spectrum Sharing Radar: Coexistence via Xampling". In: *IEEE Transactions on Aerospace and Electronic Systems* 54.3 (2018), pp. 1279–1296. DOI: 10.1109/TAES.2017.2780599.

[CT06] Emmanuel J. Candes and Terence Tao. "Near-Optimal Signal Recovery From Random Projections: Universal Encoding Strategies?" In: *IEEE Transactions on Information Theory* 52.12 (2006), pp. 5406–5425. DOI: 10.1109/TIT.2006.885507.

[D06] D.L. Donoho. "Compressed sensing". In: *IEEE Transactions on Information Theory* 52.4 (2006), pp. 1289–1306. DOI: 10.1109/TIT.2006.871582.

[DCW+13] Sintayehu Dehnie, Vasu Chakravarthy, Zhiqiang Wu, Chittabrata Ghosh, and Husheng Li. "Spectrum Coexistence Issues: Challenges and Research Directions". In: *MILCOM 2013 - 2013 IEEE Military Communications Conference*. 2013, pp. 1681–1689. DOI: 10.1109/MILCOM.2013.285.

[DDD04] I. Daubechies, M. Defrise, and C. De Mol. "An iterative thresholding algorithm for linear inverse problems with a sparsity constraint". In: *Communications on Pure and Applied Mathematics* 57.11 (2004), pp. 1413–1457. DOI: https://doi.org/10.1002/cpa.20042. eprint: https://onlinelibrary.wiley.com/doi/pdf/10.1002/cpa.20042. URL: https://onlinelibrary.wiley.com/doi/abs/10.1002/cpa.20042.

[dG12] Yohann de Castro and Fabrice Gamboa. "Exact reconstruction using Beurling minimal extrapolation". In: *Journal of Mathematical Analysis and Applications* 395.1 (2012), pp. 336–354. ISSN: 0022-247X. DOI: https://doi.org/10.1016/j.jmaa.2012.05.011. URL: https://www.sciencedirect.com/science/article/pii/S0022247X12003952.

[DLH+15] Chao Dong, Chen Change Loy, Kaiming He, and Xiaoou Tang. *Image Super-Resolution Using Deep Convolutional Networks*. 2015. arXiv: 1501.00092 [cs.CV].

[DTD+12] David L. Donoho, Yaakov Tsaig, Iddo Drori, and Jean-Luc Starck. "Sparse Solution of Underdetermined Systems of Linear Equations by Stagewise Orthogonal Matching Pursuit". In: *IEEE Transactions on Information Theory* 58.2 (2012), pp. 1094–1121. ISSN: 00189448. DOI: 10.1109/TIT.2011.2173241.

[E10a] Michael Elad. *Sparse and redundant representations: from theory to applications in signal and image processing*. Vol. 2. 1. Springer, 2010.

[E10b] Joachim H.G. Ender. "On compressive sensing applied to radar". In: *Signal Processing* 90.5 (2010). Special Section on Statistical Signal and Array Processing, pp. 1402–1414. ISSN: 0165-1684. DOI: https://doi.org/10.1016/j.sigpro.2009.11.009. URL: https://www.sciencedirect.com/science/article/pii/S0165168409004721.

[E20] Joachim Ender. *Radar - Techniques and Signal Processing*. 2020.

[FFG22] Laura Freijeiro-González, Manuel Febrero-Bande, and Wenceslao González-Manteiga. "A Critical Review of LASSO and Its Derivatives for Variable Selection Under Dependence Among Covariates". In: *International Statistical Review* 90.1 (2022), pp. 118–145. DOI: https://doi.org/10.1111/insr.12469. eprint: https://onlinelibrary.wiley.com/doi/pdf/10.1111/insr.12469. URL: https://onlinelibrary.wiley.com/doi/abs/10.1111/insr.12469.

[FR13] Simon Foucart and Holger Rauhut. *A Mathematical Introduction to Compressive Sensing*. New York, NY: Springer New York, 2013. ISBN: 978-0-8176-4947-0. DOI: 10.1007/978-0-8176-4948-7.

[FXZ+14] Jian Fang, Zongben Xu, Bingchen Zhang, Wen Hong, and Yirong Wu. "Fast Compressed Sensing SAR Imaging Based on Approximated Observation". In: *IEEE Journal of Selected Topics in Applied Earth Observations and Remote Sensing* 7.1 (2014), pp. 352–363. DOI: 10.1109/JSTARS.2013.2263309.

[GAC23] Sanhita Guha, Faisal Ahmed, and Miguel Heredia Conde. "A Novel Approach for Solving MPI for Multi-Target ToF Imaging Using Subdivision-Based Nested Compressed Sensing". In: *2023 31st European Signal Processing Conference (EUSIPCO)*. 2023, pp. 1933–1937. DOI: 10.23919/EUSIPCO58844.2023.10289807.

[GBC+13] H. Griffiths, S. Blunt, L. Cohen, and L. Savy. "Challenge problems in spectrum engineering and waveform diversity". In: *2013 IEEE Radar Conference (RadarCon13)*. 2013, pp. 1–5. DOI: 10.1109/RADAR.2013.6586140.

[GBE22] Sanhita Guha, Andreas Bathelt, and Joachim Ender. "On two approaches to radar band fusion". In: *2021 18th European Radar Conference (EuRAD)*. 2022, pp. 341–344. DOI: 10.23919/EuRAD50154.2022.9784537.

[GBE23] Sanhita Guha, Andreas Bathelt, and Joachim Ender. "A Subdivision-Fusion Algorithm for Radar Range Super-Resolution in Gapped Bands". In: *IGARSS 2023 - 2023 IEEE International Geoscience and Remote Sensing Symposium*. 2023, pp. 6310–6313. DOI: 10.1109/IGARSS52108.2023.10281967.

[GBH+22] Sanhita Guha, Andreas Bathelt, Miguel Heredia Conde, and Joachim Ender. "Radar Band Fusion Using Frame-Based Compressed Sensing". In: *IEEE Journal of Selected Topics in Signal Processing* (2022).

[GCB+18] Elisa Giusti, Davide Cataldo, Alessio Bacci, Sonia Tomei, and Marco Martorella. "ISAR Image Resolution Enhancement: Compressive Sensing Versus State-of-the-Art Super-Resolution Techniques". In: *IEEE Transactions on Aerospace and Electronic Systems* 54.4 (2018), pp. 1983–1997. DOI: 10.1109/TAES.2018.2807283.

[GCW+15] H. Griffiths, L. Cohen, S. Watts, E. Mokole, C. Baker, M. Wicks, and S. Blunt. "Radar Spectrum Engineering and Management: Technical and Regulatory Issues". In: *Proceedings of the IEEE* 103.14 (2015), pp. 85–102. DOI: 10.1109/JPROC.2014.2365517.

[GDE22] Sanhita Guha, Mihai Datcu, and Joachim Ender. "Sar Super-Resolution Using Physics-Aware Adaptive Compressed Sensing". In: *IGARSS 2022 - 2022 IEEE International Geoscience and Remote Sensing Symposium*. 2022, pp. 52–55. DOI: 10.1109/IGARSS46834.2022.9884535.

[GL10] Karol Gregor and Yann LeCun. "Learning Fast Approximations of Sparse Coding". In: *Proceedings of the 27th International Conference on International Conference on Machine Learning*. ICML'10. Haifa, Israel: Omnipress, 2010, pp. 399–406. ISBN: 9781605589077.

[H17] Miguel Heredia Conde. "Compressive sensing for the photonic mixer device". In: *Compressive Sensing for the Photonic Mixer Device: Fundamentals, Methods and Results*. Springer, 2017, pp. 207–352.

[HAJ+15] Muhammad Abdul Hadi, Saleh A. Alshebeili, Khalid Jamil, and Fathi E. Abd El-Samie. "Compressive sensing applied to radar systems: an overview". In: *Signal, Image and Video Processing* 9 (2015), pp. 25–39. URL: https://api.semanticscholar.org/CorpusID:207316507.

[HKB+18] M Heredia Conde, Thomas Kerstein, Bernd Buxbaum, and Otmar Loffeld. "Fast multipath estimation for PMD sensors". In: *5th International Workshop on Compressed Sensing Theory and its Applications to Radar, Sonar, and Remote Sensing (CoSeRa 2018)*. 2018.

[HKK+20] Miguel Heredia Conde, Keiichiro Kagawa, Tomoya Kokado, Shoji Kawahito, and Otmar Loffeld. "Single-Shot Real-Time Multiple-Path Time-of-Flight Depth Imaging for Multi-Aperture and Macro-Pixel Sensors". In: *ICASSP 2020 - 2020 IEEE International Conference on Acoustics, Speech and Signal Processing (ICASSP)*. 2020, pp. 1469–1473. DOI: 10.1109/ICASSP40776.2020.9054565.

[HLX+12] Chu He, Longzhu Liu, Lianyu Xu, Ming Liu, and Mingsheng Liao. "Learning Based Compressed Sensing for SAR Image Super-Resolution". In: *IEEE Journal of Selected Topics in Applied Earth Observations and Remote Sensing* 5.4 (2012), pp. 1272–1281. DOI: 10.1109/JSTARS.2012.2189555.

[HS90] Yingbo Hua and Tapan K Sarkar. "Matrix pencil method for estimating parameters of exponentially damped/undamped sinusoids in noise". In: *IEEE Transactions on Acoustics, Speech, and Signal Processing* 38.5 (1990), pp. 814–824.

[HZ10] Junzhou Huang and Tong Zhang. "The benefit of group sparsity". In: *The Annals of Statistics* 38.4 (2010), pp. 1978–2004. DOI: 10.1214/09-AOS778. URL: https://doi.org/10.1214/09-AOS778.

[HZJ18] Biao Hou, Kang Zhou, and Licheng Jiao. "Adaptive Super-Resolution for Remote Sensing Images Based on Sparse Representation With Global Joint Dictionary Model". In: *IEEE Transactions on Geoscience and Remote Sensing* 56.4 (2018), pp. 2312–2327. DOI: 10.1109/TGRS.2017.2778191.

[IHJ16] Amirul Islam, Mohammad Arif Hossain, and Yeong Min Jang. "Interference mitigation technique for Time-of-Flight (ToF) camera". In: *2016 eighth international conference on ubiquitous and future networks (ICUFN)*. IEEE. 2016, pp. 134–139.

[J] Christian A. Herter Jr. "The Electromagnetic Spectrum: A Critical Natural Resource, 25 Nat. Res. J. 651 (1985)". In: *Natural Resources Journal* (). URL: https://digitalrepository.unm.edu/nrj/vol25/iss3/6.

[KBC13] Ahmed Kirmani, Arrigo Benedetti, and Philip A Chou. "Spumic: Simultaneous phase unwrapping and multipath interference cancellation in time-of-flight cameras using spectral methods". In: *2013 IEEE International Conference on Multimedia and Expo (ICME)*. IEEE. 2013, pp. 1–6.

[KPD+60] J. R. Klauder, A. C. Price, S. Darlington, and W. J. Albersheim. "The Theory and Design of Chirp Radars". In: *Bell System Technical Journal* 39.4 (1960), pp. 745–808. ISSN: 00058580. DOI: 10.1002/j.1538-7305.1960.tb03942.x.

[KRX+14] J. Karlsson, W. Rowe, L. Xu, G. Glentis, and J. Li. "Fast missing-data IAA with application to notched spectrum SAR". In: *IEEE Transactions on Aerospace and Electronic Systems* 50.13 (2014), pp. 959–971. DOI: 10.1109/TAES.2014.120529.

[LJS+13] Simon Lacoste-Julien, Martin Jaggi, Mark Schmidt, and Patrick Pletscher. *Block-Coordinate Frank-Wolfe Optimization for Structural SVMs*. 2013. arXiv: 1207.4747 [cs.LG].

[LLM+19] Suhas Lohit, Dehong Liu, Hassan Mansour, and Petros T. Boufounos. "Unrolled Projected Gradient Descent for Multi-spectral Image Fusion". In: *ICASSP 2019 - 2019 IEEE International Conference on Acoustics, Speech and Signal Processing (ICASSP)*. 2019, pp. 7725–7729. DOI: 10.1109/ICASSP.2019.8683124.

[LM04] Nadav Levanon and Eli Mozeson. *Radar signals*. Hoboken, New Jersey: John Wiley & Sons Inc, 2004. ISBN: 0-471-47378-2. DOI: 10.1002/0471663085. URL: https://onlinelibrary.wiley.com/doi/book/10.1002/0471663085.

[LMP+20] Fan Liu, Christos Masouros, Athina P. Petropulu, Hugh Griffiths, and Lajos Hanzo. "Joint Radar and Communication Design: Applications, State-of-the-Art, and the Road Ahead". In: *IEEE Transactions on Communications* 68.6 (2020), pp. 3834–3862. DOI: 10.1109/TCOMM.2020.2973976.

[LSH23] Alvaro Lopez Paredes, Qiang Song, and Miguel Heredia Conde. "Performance Evaluation of State-of-the-Art High-Resolution Time-of-Flight Cameras". In: *IEEE Sensors Journal* 23.12 (2023), pp. 13711–13727. DOI: 10.1109/JSEN.2023.3273165.

[LZC+23] Fan Liu, Le Zheng, Yuanhao Cui, Christos Masouros, Athina P. Petropulu, Hugh Griffiths, and Yonina C. Eldar. "Seventy Years of Radar and Communications: The road from separation to integration". In: *IEEE Signal Processing Magazine* 40.5 (July 2023), pp. 106–121. ISSN: 1558-0792. DOI: 10.1109/MSP.2023.3272881.

[ME11] Moshe Mishali and Yonina C. Eldar. *Xampling: Compressed Sensing of Analog Signals*. 2011. arXiv: 1103.2960 [cs.IT].

[MGB08] Lukas Meier, Sara van de Geer, and Peter Bühlmann. "The group lasso for logistic regression". In: *Journal of the Royal Statistical Society: Series B (Statistical Methodology)* 70 (2008). URL: https://api.semanticscholar.org/CorpusID:16300010.

[MLE20] Vishal Monga, Yuelong Li, and Yonina C. Eldar. *Algorithm Unrolling: Interpretable, Efficient Deep Learning for Signal and Image Processing*. 2020. arXiv: 1912.10557 [eess.IV].

[MSH+21] Dingyou Ma, Nir Shlezinger, Tianyao Huang, Yariv Shavit, Moshe Namer, Yimin Liu, and Yonina C. Eldar. "Spatial Modulation for Joint Radar-Communications Systems: Design, Analysis, and Hardware Prototype". In: *IEEE Transactions on Vehicular Technology* 70.3 (2021), pp. 2283–2298. DOI: 10.1109/TVT.2021.3056408.

[MY09] Nicolai Meinshausen and Bin Yu. "Lasso-Type Recovery of Sparse Representations for High-Dimensional Data". In: *The Annals of Statistics* 37.1 (2009), pp. 246–270. ISSN: 00905364, 21688966. URL: http://www.jstor.org/stable/25464748 (visited on 05/08/2022).

[NKR+15] Nikhil Naik, Achuta Kadambi, Christoph Rhemann, Shahram Izadi, Ramesh Raskar, and Sing Bing Kang. "A light transport model for mitigating multipath interference in time-of-flight sensors". In: *Proceedings of the IEEE Conference on Computer Vision and Pattern Recognition*. 2015, pp. 73–81.

[NSI+19] Thanh T. Nguyen, Charles Soussen, Jérôome Idier, and El-Hadi Djermoune. "NP-hardness of l0 minimization problems: revision and extension to the non-negative setting". In: *2019 13th International conference on Sampling Theory and Applications (SampTA)*. 2019, pp. 1–4. DOI: 10.1109/SampTA45681.2019.9030937.

[O79] Nobuyuki Otsu. "A Threshold Selection Method from Gray-Level Histograms". In: *IEEE Transactions on Systems, Man, and Cybernetics* 9.1 (1979), pp. 62–66. DOI: 10.1109/TSMC.1979.4310076.

[P23] Reinhard Panhuber. "Fast, Efficient, and Viable Compressed Sensing, Low-Rank, and Robust Principle Component Analysis Algorithms for Radar Signal Processing". In: *Remote Sensing* 15.8 (2023), p. 2216.

[PBI20] Swati S Patil, Pratik M Bhade, and Vandana S Inamdar. "Depth recovery in time of flight range sensors via compressed sensing algorithm". In: *International Journal of Intelligent Robotics and Applications* 4 (2020), pp. 243–251.

[PI21] Swati Suresh Patil and Vandana S Inamdar. "Mitigating Multipath Interference for Time of Flight Range Sensors via Deep Convolutional Networks". In: *2021 7th International Conference on Computer and Communications (ICCC)*. IEEE. 2021, pp. 277–281.

[R14] M. A. Richards. *Fundamentals of radar signal processing*. 2nd ed. McGraw-Hill's AccessEngineering. Chicago, Ill.: McGraw-Hill Education LLC, 2014. ISBN: 9780071798327. URL: https://www.accessengineeringlibrary.com/content/book/9780071798327.

[S49] C.E. Shannon. "Communication in the Presence of Noise". In: *Proceedings of the IRE* 37.1 (1949), pp. 10–21. DOI: 10.1109/JRPROC.1949.232969.

[S99a] M. Soumekh. *Synthetic Aperture Radar Signal Processing with MATLAB Algorithms*. Wiley, 1999. ISBN: 9780471297062. URL: https://books.google.de/books?id=gVWqQgAACAAJ.

[S99b] Mehrdad Soumekh. "Synthetic Aperture Radar Signal Processing with MATLAB Algorithms". In: 1999. URL: https://api.semanticscholar.org/CorpusID:60164406.

[SLB+21] Peyman F. Shahandashti, P. López, V.M. Brea, D. García-Lesta, and Miguel Heredia-Conde. "Proposal of a Single-Shot Multi-Frame Multi-Frequency CMOS ToF Sensor". In: *2021 28th IEEE International Conference on Electronics, Circuits, and Systems (ICECS)*. 2021, pp. 1–4. DOI: 10.1109/ICECS53924.2021.9665528.

[SLL+09] P. Stoica, J. Li, J. Ling, and Y. Cheng. "Missing data recovery via a nonparametric iterative adaptive approach". In: *2009 IEEE International Conference on Acoustics, Speech and Signal Processing*. 12. 2009, pp. 3369–3372. DOI: 10.1109/ICASSP.2009.4960347.

[SLL00] Petre Stoica, Erik G. Larsson, and Jian Li. "Adaptive Filter-bank Approach to Restoration and Spectral Analysis of Gapped Data*". In: *The Astronomical Journal* 120.4 (Oct. 2000), p. 2163. DOI: 10.1086/301572. URL: https://dx.doi.org/10.1086/301572.

[ST23] Josiah W. Smith and Murat Torlak. "Deep Learning-Based Multiband Signal Fusion for 3-D SAR Super-Resolution". In: *IEEE Transactions on Aerospace and Electronic Systems* (2023), pp. 1–17. DOI: 10.1109/TAES.2023.3270111.

[TDJ+21] Reiner Thomä, Thomas Dallmann, Snezhana Jovanoska, Peter Knott, and Anke Schmeink. "Joint Communication and Radar Sensing: An Overview". In: *2021 15th European Conference on Antennas and Propagation (EuCAP)*. 2021, pp. 1–5. DOI: 10.23919/EuCAP51087.2021.9411178.

[TLZ09] Weiming Tian, Haibo Liu, and Tao Zeng. "Frequency and time synchronization error analysis based on generalized signal model for Bistatic SAR". In: *2009 IET International Radar Conference*. 2009, pp. 1–4. DOI: 10.1049/cp.2009.0476.

[VXX+12] Duc Vu, Luzhou Xu, Ming Xue, and Jian Li. "Nonparametric Missing Sample Spectral Analysis and Its Applications to Interrupted SAR". In: *IEEE Journal of Selected Topics in Signal Processing* 6.1 (2012), pp. 1–14. DOI: 10.1109/JSTSP.2011.2168192.

[W14] Andrzej Wolski. *Theory of electromagnetic fields*. 2014. arXiv: 1111.4354 [physics.acc-ph].

[WSL+21] Henk Wymeersch, Deep Shrestha, Carlos Morais de Lima, Vijaya Yajnanarayana, Björn Richerzhagen, Musa Furkan Keskin, Kim Schindhelm, Alejandro Ramirez, Andreas Wolfgang, Mar Francis de Guzman, Katsuyuki Haneda, Tommy Svensson, Robert Baldemair, and Stefan Parkvall. "Integration of Communication and Sensing in 6G: a Joint Industrial and Academic Perspective". In: *2021 IEEE 32nd Annual International Symposium on Personal, Indoor and Mobile Radio Communications (PIMRC)*. 2021, pp. 1–7. DOI: 10.1109/PIMRC50174.2021.9569364.

[WX22] Xiao Wang and Feng Xu. "Tomographic SAR Inversion by Atomic-Norm Minimization—The Gridless Compressive Sensing Approach". In: *IEEE Transactions on Geoscience and Remote Sensing* 60 (2022), pp. 1–13. DOI: 10.1109/TGRS.2022.3223524.

[WZD+18] Longgang Wang, Mana Zheng, Wenbo Du, Menglin Wei, and Lianlin Li. "Super-resolution SAR Image Reconstruction via Generative Adversarial Network". In: *2018 12th International Symposium on Antennas, Propagation and EM Theory (ISAPE)*. 2018, pp. 1–4. DOI: 10.1109/ISAPE.2018.8634345.

[XSE+23] Lei Xie, Shenghui Song, Yonina C. Eldar, and Khaled B. Letaief. "Collaborative Sensing in Perceptive Mobile Networks: Opportunities and Challenges". In: *IEEE Wireless Communications* 30.1 (2023), pp. 16–23. DOI: 10.1109/MWC.005.2200214.

[YBZ20] Weixing Yang, Hui Bi, and Daiyin Zhu. "Improved SAR imaging algorithm with azimuth periodically missing data". In: *IET Radar, Sonar & Navigation* 14.3 (2020), pp. 399–406. DOI: https://doi.org/10.1049/iet-rsn.2019.0320. eprint: https://ietresearch.onlinelibrary.wiley.com/doi/pdf/10.1049/iet-rsn.2019.0320. URL: https://ietresearch.onlinelibrary.wiley.com/doi/abs/10.1049/iet-rsn.2019.0320.

[YHK+19] Rabia Tugce Yazicigil, Tanbir Haque, Peter R. Kinget, and John Wright. "Taking Compressive Sensing to the Hardware Level: Breaking Fundamental Radio-Frequency Hardware Performance Tradeoffs". In: *IEEE Signal Processing Magazine* 36.2 (2019), pp. 81–100. DOI: 10.1109/MSP.2018.2880837.

[YL06] Ming Yuan and Yi Lin. "Model Selection and Estimation in Regression With Grouped Variables". In: *Journal of the Royal Statistical Society Series B* 68 (Feb. 2006), pp. 49–67. DOI: 10.1111/j.1467-9868.2005.00532.x.

[YLP+09] Depeng Yang, Husheng Li, Gregory D. Peterson, and Aly Fathy. "Compressed sensing based UWB receiver: Hardware compressing and FPGA reconstruction". In: *2009 43rd Annual Conference on Information Sciences and Systems*. 2009, pp. 198–201. DOI: 10.1109/CISS.2009.5054716.

[YMS22] Wei Yang, ZiQian Ma, and YingRu Shi. "SAR Image Super-Resolution based on Artificial Intelligence". In: *IGARSS 2022 - 2022 IEEE International Geoscience and Remote Sensing Symposium*. 2022, pp. 4643–4646. DOI: 10.1109/IGARSS46834.2022.9884456.

[ZG18] Jian Zhang and Bernard Ghanem. *ISTA-Net: Interpretable Optimization-Inspired Deep Network for Image Compressive Sensing*. 2018. arXiv: 1706.07929 [cs.CV].

[ZLM+21] J. Andrew Zhang, Fan Liu, Christos Masouros, Robert W. Heath, Zhiyong Feng, Le Zheng, and Athina Petropulu. "An Overview of Signal Processing Techniques for Joint Communication and Radar Sensing". In: *IEEE Journal of Selected Topics in Signal Processing* 15.6 (2021), pp. 1295–1315. DOI: 10.1109/JSTSP.2021.3113120.

[ZLQ19] Wei Zhang, Jiaojie Li, and Xuyi Qiu. "SAR Image Super-Resolution Using Deep Residual SqueezeNet". In: *Proceedings of the International Conference on Artificial Intelligence, Information Processing and Cloud Computing*. AIIPCC '19. Sanya, China: Association for Computing Machinery, 2019. ISBN: 9781450376334. DOI: 10.1145/3371425.3371456. URL: https://doi.org/10.1145/3371425.3371456.

[ZRH+21] Andrew Zhang, Md. Lushanur Rahman, Xiaojing Huang, Yingjie Jay Guo, Shanzhi Chen, and Robert W. Heath. "Perceptive Mobile Networks: Cellular Networks With Radio Vision via Joint Communication and Radar Sensing". In: *IEEE Vehicular Technology Magazine* 16.2 (2021), pp. 20–30. DOI: 10.1109/MVT.2020.3037430.

[ZWZ+22] Yuwei Zhao, Xia Wang, Yixin Zhang, Yujie Fang, and BingHua Su. "Polarization-based approach for multipath interference mitigation in time-of-flight imaging". In: *Appl. Opt.* 61.24 (Aug. 2022), pp. 7206–7217. DOI: 10.1364/AO.461954. URL: https://opg.optica.org/ao/abstract.cfm?URI=ao-61-24-7206.